Title: Novel quantal analysis method reveals conservation of average excitatory synaptic charge across cortical pyramidal neurons of different sizes

Author Names and Affiliations: Martynas Dervinis[1], Guy Major[1]

[1]: Cardiff University, Cardiff, Wales, CF10 3AT, UK

Corresponding author email address: martynas.dervinis@gmail.com

Number of pages: 52

Number of figures: 12

Number of words

Abstract: 217

Body text excluding Materials and Methods: 4193 (946 + 3247)

Conflict of interest statement: The authors declare no competing financial interests.

Acknowledgements: Cardiff University (GM, MD), The Medical Research Council of the UK (MD PhD). Neural activity simulations were performed on the Cardiff School of Biosciences' Biocomputing Hub HPC/Cloud infrastructure.

Abstract

In chemical synapses of the central nervous system (CNS), information is transmitted via the presynaptic release of a vesicle (or 'quantum') of neurotransmitter, which elicits a postsynaptic electrical response with an amplitude termed the 'quantal size'. Measuring amplitudes of miniature postsynaptic currents (mPSCs) or potentials (mPSPs) at the cell soma is generally thought to offer a technically straightforward way to estimate quantal sizes, as each of these miniature responses (minis) is generally thought to be elicited by the spontaneous release of a single neurotransmitter vesicle. However, in large highly-branched neurons, a somatically recorded mini is typically massively attenuated compared with at its input site, and a significant fraction are indistinguishable from (or cancelled out by) background noise fluctuations. Here, using a new software package called 'minis', we describe a novel quantal analysis method that estimates the 'electrical size' of the synapse by comparing events detected in somatic recordings from the same neuron of (a) *real* minis and (b) background noise (minis blocked pharmacologically) with *simulated* minis added by a genetic algorithm. The estimated minis' distributions reveal a striking inverse dependence of mean excitatory mPSP amplitude on total cell capacitance (proportional to cell size, more exactly, extracellular membrane surface area) suggesting that, in rats at least, the average charge injected by excitatory synapses is conserved across neocortical pyramidal neurons of different sizes.

42 # Abbreviations

43 ABF – Axon Binary File

44 aCSF – artificial cerebrospinal fluid

45 AMPA – α-amino-3-hydroxy-5-methyl-4-isoxazolepropionic acid

46 AMPAR – α-amino-3-hydroxy-5-methyl-4-isoxazolepropionic acid receptor

47 ANN – artificial neural network

48 AP – action potential

49 CGP55845A – selective competitive antagonist of $GABA_B$ receptors (thus slow K^+ dependent IPSPs)

50 CPP – (*RS*)-3-(2-carboxypiperazin-4-yl)-propyl-1-phosphonic acid (potent selective competitive
51 glutamate NMDA receptor antagonist, thus depolarization-dependent, slow component of EPSPs)

52 EPSC – excitatory postsynaptic current

53 EPSP – excitatory postsynaptic potential

54 GA – genetic algorithm

55 GABA – gamma-aminobutyric acid (inhibitory neurotransmitter)

56 IC50 – concentration blocking half of the receptors

57 IPSC – inhibitory post-synaptic current

58 IPSP – inhibitory post-synaptic potential

59 MAD – maximum absolute deviation

60 mEPSC– miniature excitatory post-synaptic current

61 mEPSP– miniature excitatory post-synaptic potential

62 mIPSP– miniature inhibitory post-synaptic potential

63 mPSC – miniature post-synaptic current

64 mPSP – miniature post-synaptic potential

65 NBQX – 2,3-dioxo-6-nitro-1,2,3,4-tetrahydrobenzo[*f*]quinoxaline-7-sulfonamide (potent selective
66 competitive antagonist of AMPA (and kainate) glutamate receptors, thus fast component of EPSPs)

67 NMDA – N-methyl-D-aspartate

68 NMDAR - N-methyl-D-aspartate receptor

69 SAD – sum of absolute deviations

70 SD – standard deviation

71 smEPSP – simulated mEPSP

72 SSD – sum of signed deviations

73 SSE – sum of squared errors

74 TTX – tetrodotoxin (potent selective competitive antagonist of Na^+ channels, thus action potentials)

75 V_m – transmembrane potential

76

Introduction

Synaptic transmission in the CNS occurs in 'quanta' (Forti et al., 1997; Hardingham et al., 2010; Isaacson and Walmsley, 1995; Jonas et al., 1993; Kraszewski and Grantyn, 1992; Kullmann and Nicoll, 1992; Kuno, 1964; Larkman et al., 1991; Sahara and Takahashi, 2001; Stern et al., 1992; Wall and Usowicz, 1998), usually thought to each correspond to the release of a single neurotransmitter vesicle (Heuser et al., 1979). The amplitude of the postsynaptic response to a quantum of transmitter, the quantal size, is a key parameter defining the efficacy of synaptic transmission (Katz, 1969; Vere-Jones, 1966) and, therefore, an important determinant of neural computation.

Quantal size measurements in the CNS are difficult due to multi-synaptic contacts (multiple synapses per connection between a particular pair of neurons and multiple release sites/postsynaptic densities/receptor "rafts" for some synapses), limited accessibility, significant quantal variance (both within and between synapses of a given connection), temporal non-stationarity of synaptic properties (e.g. receptor desensitisation or internalisation, and depletion of glutamate from presynaptic vesicles), and low signal-to-noise ratios of somatic electrophysiological recordings of quantal events (Bekkers, 1994; Farsi et al., 2021; Korn and Faber, 1991). For these reasons classical quantal analysis as done at the neuromuscular junction has run into problems in central synapses, where most of the minis do not 'stand out' from the noise. More recent methods such as noise deconvolution, Variance-Mean analysis, and optical quantal analysis have not fared much better (Biró et al., 2005; Clamann et al., 1991; Clements, 2003; Clements and Silver, 2000; Edwards et al., 1976; Enoki et al., 2009; Jack et al., 1981; Liu et al., 2022; Oertner et al., 2002; Peled and Isacoff, 2011; Redman, 1990; Reid and Clements, 1999; Silver, 2003; Yuste et al., 1999), or suffer from potential selection biases (e.g. paired recordings typically require cells close together whose synapses may be a non-representative sub-population, differing from the overall population of synapses).

A complementary method of assessing synaptic function is to measure properties of mPSCs. Miniature PSC amplitude measurements are often taken as quantal size estimates across the population of active synapses onto a neuron, as the mPSC (under voltage clamp) or mPSP (under voltage recording) likely corresponds to the response to a spontaneous release of a single neurotransmitter vesicle (Brown et al., 1979; del Castillo and Katz, 1954; Fatt and Katz, 1952; Isaacson and Walmsley, 1995; Wall and Usowicz, 1998). Measurements of mPSC amplitudes are routine in the literature. However, they are likely overestimates due to small amplitude events being difficult to detect and largely being missed or lost in the noise.

The use of voltage clamp can be a major reason why mPSCs “go missing”. Theoretical studies (Major, 1993a; Rall and Segev, 1985; Spruston et al., 1993) predicted and experimental findings (Williams and Mitchell, 2008) confirmed that somatic voltage clamp fails to space clamp extended dendrites, and to capture all (or even most of) the current flowing in at electrically remote synapses. Amplitude attenuation can also be caused if series resistance is not compensated (Major, 1993a; Williams and Mitchell, 2008). These issues can be somewhat sidestepped by switching to voltage recording, at the cost of (a little) more temporal integration.

However, most mPSCs go undetected because of the electrophysiology of the neuron itself. Distal minis leak charge via the dendritic membrane, but an even more significant amplitude attenuation, 40-fold or more, is inflicted by charging the membrane capacitance of the entire dendritic arbour (Larkum et al., 2009; Major et al., 2013a; Nevian et al., 2007; Stuart and Spruston, 1998; Williams and Mitchell, 2008; Williams and Stuart, 2002). Such amplitudes, at the soma (approximately 80 µV, on average, in layer 5 pyramidal neurons (Nevian et al. 2007), detected via simultaneous dendritic whole-cell recordings) are often indistinguishable from noise fluctuations. Recording from thin dendrites close to synaptic input sites is technically extremely challenging – a tour de force beyond

128 most labs. Therefore, a reliable yet widely accessible quantal analysis method, based on standard
129 somatic whole-cell patch recording, would require taking account of the background noise in
130 addition to measuring putative mPSPs (or mPSCs).
131
132 Here we describe such a method, based on recording excitatory mPSPs (mEPSPs) in the presence of
133 background physiological noise ('noise with minis') then noise alone, from the same cell, after
134 blocking mEPSPs pharmacologically. To detect mEPSP-like events in these recordings, we used a
135 newly developed algorithm called 'minis' which is described in our companion article (Dervinis and
136 Major, 2024). Because of small potentials being 'overshadowed' by larger minis, either by
137 summating with them on rising phases, or having their amplitudes reduced on decaying phases
138 (analysed and discussed in detail in our companion article (Dervinis and Major, 2024)), events
139 detected in the 'noise-alone' recording cannot be used to remove the noise component in the 'noise
140 with minis' recording simply by subtracting their two distributions. Instead, we adopted the
141 approach of using simulated minis, superimposing them on the 'noise-alone' recording and varying
142 their parameters until the amplitude and rise time distributions of events detected in the 'noise with
143 simulated minis' voltage trace closely matches those from the 'noise with real minis' recording, with
144 identical detection parameters. Therefore, we augmented our 'minis' software with a genetic
145 optimisation algorithm (GA) that automatically adjusts amplitudes, rise times and frequencies of
146 simulated minis until a statistically indistinguishable match is achieved. This novel quantal analysis
147 method produced an unbiased 'upper limit' quantal charge estimate for excitatory neocortical
148 synapses in the rat of approximately 31.3 pC, on average, which was conserved across pyramidal
149 neurons of all sizes in cortical layers 2/3 and 5. 'Minis' thus provides an experimentally
150 straightforward quantal analysis method for detecting mPSPs or mPSCs in somatic recordings, and
151 (in aggregate) 'separating' the smaller of these events from comparably-sized background noise
152 fluctuations.
153

Materials and Methods

Animals and electrophysiology

All experimental procedures were carried out in accordance with the UK Animals (Scientific Procedures) Act 1986. The full description is provided in our companion article (Dervinis and Major, 2024). Coronal somatosensory neocortical slices obtained from 19- to 27-day old Wistar rats (RRID:RGD_13508588; n = 11) were used to obtain whole-cell voltage recordings (n = 14) of mEPSPs in the background of physiological (and other) noise ('noise with minis' condition), by superfusing artificial cerebrospinal fluid (aCSF) containing blockers of action potentials (APs) and inhibitory postsynaptic potentials (IPSPs). Excitatory postsynaptic potential (EPSP) blockers were then added ('noise-alone' condition, with all glutamatergic, GABAergic and AP-dependent synaptic potentials blocked, i.e. the vast majority of fast synaptic inputs in the neocortex), and background noise traces were recorded from each cell, while maintaining stability of the whole-cell recording (as judged by numerous criteria, below).

Passive membrane time constant, total membrane capacitance, input resistance, and bridge balance (series resistance compensation) error were estimated by injecting current pulses as described in (Major et al., 1993).

Methodology

The goal of the study was to design an experimentally straightforward quantal analysis method based on standard somatic recordings of minis, as opposed to far more challenging recordings from sub-micron diameter input dendrites closer to (a few of) the synapses. Due to their low signal-to-noise ratio, *simulated* minis were used to infer the signal (mEPSP) component and to eliminate (in aggregate) the noise component in these recordings.

179 The experimental design of this study was similar to the one described in the preceding companion
180 article (Dervinis and Major, 2024). As described in the previous section, whole-cell recordings were
181 obtained where first mEPSPs were recorded in the background of physiological and other noise
182 followed by blocking EPSPs pharmacologically to record 'pure' noise in the absence of minis.
183 Simulated mEPSPs (smEPSPs) were then randomly added to the noise traces (Figure 1) and the
184 'minis' algorithm was applied to this 'noise with simulated minis' voltage trace. The resulting
185 distribution of detected events (in terms of their amplitudes and 10-90% rise times) was compared
186 to the equivalent distribution based on the 'noise with real minis' recording, detected with the same
187 parameters (such as amplitude detection threshold, baseline duration and maximum rise time gap
188 till each peak). The discrepancy between the two distributions was used to inform the GA, which
189 would then adjust the distribution of smEPSPs and generate new 'noise with simulated minis'
190 voltage traces and compare them again to the equivalent distribution detected with the same
191 parameters from the 'noise with real minis' recording. This procedure was repeated multiple times
192 (of the order of tens to hundreds of generations with 260 examples per generation; 10 examples per
193 each parameter optimised by the GA) until the two distributions were closely matched, within the
194 bounds of chance statistical errors (details below). At the end of this process the minis distribution
195 used for simulating the closely matched recording was deemed to be the inference of the true minis
196 distribution underlying the 'noise with real minis' recording (or at least compatible with it).
197
198 **Detection of miniature postsynaptic potentials**
199 Detection of real and simulated mEPSPs was carried out using our 'minis' software. The detailed
200 description of this detection algorithm is provided in the companion article (Dervinis and Major,
201 2024). We used the same detection algorithm parameters as described in that article except for the
202 amplitude range, which was set to 0.02-10 mV.
203
204 **Selection of recordings for fitting distributions of detected real minis-like events**

205 Prior to carrying out any estimation of the distribution of minis, segments of 'noise with real minis'
206 and 'noise-alone' recordings were carefully selected. Segments containing unusual amount of noise
207 or V_m glitches were rejected. Parts of recording showing instability or drift of recording parameters
208 (or excessive movement of the recording pipette relative to the soma) were also rejected, to ensure
209 that only good quality data were used. Data analysis performed at this preprocessing/selection stage
210 were built into our 'minis' software.
211
212 As part of the preprocessing stage, 'minis' produced seven graphs showing the evolution of various
213 recording parameters across the entire duration of a single recording. An example (from the longest
214 recording obtained) is provided in Figure 2, showing these graphs as individual panels. Figure 2A
215 shows the evolution of V_m from the very beginning of the recording obtained in the regular aCSF
216 with APs present (in this case) to the very end of the recording, where APs, mIPSPs and mEPSPs were
217 all blocked for some time ('noise-alone'). The data is shown after removing V_m segments containing
218 responses to regularly injected current pulses and has a total duration of 8520 s. Throughout the
219 entirety of this recording the baseline V_m varied between –70 and –67 mV and, thus remained
220 relatively stable.
221
222 There are three time markers that extend across all figure panels marking the time when the aSCF
223 containing TTX, gabazine, and CGP55845A was infused to block APs and IPSPs (the first marker), the
224 time when APs were observed to cease (the second marker), and the time when the aCSF containing
225 NBQX and CPP was infused to block remaining EPSPs (the third marker). The recording segment
226 between the second and the third markers constituted the 'noise with minis' recording, while the
227 segment following the third marker *after* mEPSPs were eventually blocked constituted the 'noise-
228 alone' recording. The darker yellow shaded regions that also extend across all panels of Figure 2
229 mark files (epochs) that were selected for subsequent minis distribution fitting.
230

231 The remaining panels of Figure 2 were used to guide data selection. The standard deviation (SD) of
232 the V_m (Figure 2B) was useful in determining the transitions between different pharmacological
233 conditions. Stable prolonged decreases in SD reliably indicated when APs or minis were effectively
234 blocked. Sudden brief increases in SD flagged problematic recording segments containing higher
235 levels of noise or V_m glitches. Gradual increases in SD suggested gradual deterioration of recording
236 quality.
237
238 Similar information was also provided by the evolution of the biggest 10% of amplitudes of all
239 detected minis-like events in a single sweep (Figure 2C). Prolonged drop in the amplitudes marked
240 transitions between recording conditions, while sudden jumps were indicative of V_m instabilities.
241 Finally, effective decay time constants of biggest 10% of detected events (Figure 2D) could be used
242 as an indicator for the presence/absence of minis. Blocking minis resulted in time constants
243 becoming large and fluctuating unstably, indicating that only noise fluctuations were being detected
244 that did not possess the typical decay dynamics common to EPSPs.
245
246 Further insights into the recording quality over time were provided by V_m responses to brief current
247 pulses. Passive membrane time constant measurements over time (Figure 2E) were expected to
248 remain stable. Deviations from this could signal a change in passive membrane properties due to
249 degradation in the recording quality. Total membrane capacitance (Figure 2F) was also expected to
250 be stable over time. Change in the capacitance could indicate membrane tearing, patch-resealing or
251 pipette movement or clogging, loss of membrane or part of the cell or some substantial uncontrolled
252 destabilisation of the recording. Finally, change in input resistance (detected from a change in the
253 bridge balance error; Figure 2G) was not permitted to exceed the balance error estimated offline at
254 the beginning of the recorded data by more than two-fold. Violation of this rule of thumb indicated a
255 deterioration in the recording quality potentially resulting from debris accumulating in the recording
256 pipette, movement of the pipette tip or the recorded cell body, partial formation of a membrane

257 ‘tube’ (similar to what would happen in the process of producing an outside-out patch by slowly
258 retracting the pipette), or other reasons.
259
260 We obtained the seven longitudinal recording state/quality indicators described above for all our
261 recordings. Multi-panelled graphs showing these indicators for each individual recording separately
262 are provided in Supplementary Figures 1-13.
263
264 **Simulations**
265 *Simulating distributions of miniature excitatory postsynaptic potentials with a range of amplitudes*
266 *and rise times*
267 All simulations were carried out using our ‘minis’ software, developed in Matlab (Mathworks;
268 RRID:SCR_001622), and performed on the Cardiff School of Biosciences' Biocomputing Hub
269 HPC/Cloud infrastructure. Simulation of minis-like events was based on an analytical solution to the
270 passive cable equation for a transient current (Rall, 1977) using 100 lumped terms with a double
271 exponential synaptic current with τ_1= 0.15-3 ms (optimised in each instance/iteration) and τ_2 = 2 ms
272 (Major et al., 1993). The detailed description of how arbitrary shape PSPs were obtained is provided
273 in our companion article (Dervinis and Major, 2024).
274
275 A pool of simulated events was generated combining four bivariate (two-dimensional: amplitude
276 and 10-90% rise time) normal distributions. Six parameters described each distribution: amplitude
277 mean μ_X and standard deviation σ_X, 10-90% rise time mean μ_Y and standard deviation σ_Y, a
278 correlation (or rotation) factor ρ, and a (relative frequency or number) scale factor n:
279
$$f(x,y) = \frac{n}{2\pi\sigma_X\sigma_Y\sqrt{1-\rho^2}} e^{-\frac{1}{2(1-\rho^2)}\left(\left(\frac{x-\mu_X}{\sigma_X}\right)^2 - 2\rho\left(\frac{x-\mu_X}{\sigma_X}\right)\left(\frac{y-\mu_Y}{\sigma_Y}\right) + \left(\frac{y-\mu_Y}{\sigma_Y}\right)^2\right)}.$$
280 All distribution parameters were controlled by the GA.
281

Fitting distributions of detected real mini-like events

The Matlab ga() function was used to control 24 parameters describing Four (rotated) bivariate normal distributions (6 parameters per distribution). Additional controlled parameters were the synaptic rise time constant τ_1 which ranged between 0.15 and 3 ms and the passive membrane time constant τ_m. The range for the latter constant was taken to be between 0.9 times and 1.1 times the initial estimate based on the averaged waveform of all minis-like events detected in the 'noise with real minis' recording. Thus, there were 26 parameters in total, controlled by the GA.

The GA would start by generating multiple distributions of simulated minis or smEPSPs (i.e. 'individuals'; we used 260 individuals per 'generation' with 10 individuals per parameter optimised by the GA; see a single run structure in Figure3A). Events would be drawn pseudo-randomly from a distribution and then simulated events of the chosen shapes (in terms of amplitude and 10-90% rise time) would be added to the 'noise-alone' recording at times that were also chosen pseudo-randomly (Figure 1). For generating the initial set of individuals ('population'), the GA chose parameters pseudo-randomly within prescribed ranges. For each of the four bivariate normal distributions the parameter ranges were as follows: μ_X (-0.1-1 mV), σ_X (0.01-1 mV), μ_Y (-1-10 ms), σ_Y (0.25-10 ms), ρ (-1 to 1), and n (0-10,000 for the first distribution and –10,000 to 10,000 for the remaining three distributions; negative counts were used for 'sculpting' the base distribution). Any negative count bins within the resulting final distribution were zeroed out. Any events with negative rise times or amplitudes below the simulation threshold (varying non-negative value) were excluded.

Next, the GA assessed the 'fitness' of each individual in the generation by using the cost function (explained in the next subsection). The top 5% of the most fit individuals survived to the next generation without change, while individual 'crossover' ('recombination'), genetic migration, and other GA parameters were set to default values of the Matlab ga() function. A new evolved generation of individuals was then created, which then served as the basis for yet another

308 generation and so on. This process (a single run in Figure 3A) was repeated until an 'individual' was
309 created with the lowest cost (highest fitness value) possible, or there was no improvement in the
310 fitness for 100 consecutive generations, or the number of generations reached 1000 (Figure 3A).
311
312 In cases where the GA terminated without converging on the highest fitness value, the distribution
313 fitting procedure was reinitiated using the most fit individual as a seed (Runs 2 and 3 in Figure 3B).
314 The population genetic diversity was reset by setting the GA-controlled parameter ranges to ±25% of
315 the original ranges relative to the seed parameter values, to explore the space around the current
316 best seed values. The re-running of distribution fitting was repeated until the GA converged to an
317 'apparently fittest possible individual' (or the 'best fit possible/achievable'; defined in the next
318 subsection), or otherwise an 'acceptable' level of fitness was reached (also defined in the next
319 subsection), or there was no improvement in fitness compared to the previous run for two
320 consecutive runs while an 'acceptable' fit was not yet attained (Figures 3B and C). In the latter case,
321 the entire distribution fitting procedure was reinitiated starting with a high simulated amplitude
322 lower limit (e.g., 200 μV), with the limit being gradually lowered until the 'best possible' or
323 'acceptable' fit was attained (Figure 3D). This 'backwards' ('downwards') fitting procedure was
324 required for several recordings having a large mean amplitude which, when we started with a low
325 simulated amplitude lower limit, failed to converge to an acceptable fit.
326
327 If the most fit individual was within acceptable levels of fitness values, the lower threshold on
328 smEPSP amplitude was increased by 10 μV (Figures 3B and C) (or lowered during the 'backwards' i.e.
329 'downwards' fitting procedure if no 'acceptable' fit was obtained; Figure 3D) and the entire fitting
330 step was re-run. This was repeated until the GA stopped converging (or started converging during
331 the 'backwards'/'downwards' fitting procedure) on a solution with acceptable fitness values.
332

333 The reason for attempting to push up the lower limit of the amplitudes of the smEPSPs is that it
334 became obvious that GA-generated solutions were not unique. Given an acceptable fit, matching the
335 histograms of events detected from the 'noise with real minis' recording can generally be achieved
336 by using distributions with a larger number of smaller amplitude smEPSPs, which get 'lost' in the
337 noise or summate with other smEPSPs, although the distribution of bigger smEPSPs is more tightly
338 constrained. (Indeed, one can also often (but not always) achieve acceptable fits with *fewer* small
339 amplitude smEPSPs (Supplementary Figure 14)). There is large number of such distributions with
340 ever-decreasing amplitudes of smEPSPs (in theory, all the way down to events resulting from brief
341 single AMPAR or NMDAR channel sub-conductance state openings, injecting undetectably small
342 amounts of charge). Therefore, the GA with the thresholding procedure described above has no
343 guaranteed way of arriving at the true distribution of minis, only at a distribution giving an
344 approximate *upper bound* on the *mean* (or median) mini amplitude – unless further biological
345 constraints are imposed.
346
347 *Cost function*
348 The goal of the minis distribution fitting procedure was to match 'noise with simulated minis' and
349 'noise with real minis' recordings as closely as possible, in terms of the distribution of amplitudes
350 and 10-90% rise times of detected mini-like events in the two types of V_m recording traces
351 ('simulated' vs. 'real' distributions), in the process 'cancelling out' any systematic errors in
352 amplitudes or shapes introduced by the detection algorithm or the summation or superposition of
353 events. This was achieved by minimising the cost function using the GA. The cost function was
354 composed of four types of components: *shape constraints* on the *simulated* minis distribution, *sums*
355 of *absolute* deviations (SADs) between 'simulated' and 'real' distributions, *sums* of *signed* deviations
356 (SSDs) between 'simulated' and 'real' distributions, and *maximal absolute* deviations (MADs)
357 between 'simulated' and 'real' distributions (Figures 4A and B). We avoided using the sum of
358 squared errors (SSE) because it is sensitive to outliers (giving them undue weight).

We calculated the typical ranges of SADs and MADs for each of the 14 recordings by taking the individual 'noise with real minis' recording and dividing it into smaller files (range was 15-606 files), each the duration of a single recording sweep (20 s, typically). Each file in this set was subjected to the minis detection procedure resulting in a set of 'real' (detected mini-like events) distributions. These were then subtracted from each other, in all pairwise combinations, and the corresponding SAD (sum of absolute deviations) and MAD (maximum absolute deviation) scores were calculated for each of the possible n*(n-1)/2 file pairings (range 105 to 183315, corresponding to 15 to 606 available files, respectively). Six SAD- and six MAD-based scores were calculated based on: distributions of amplitudes of (1) *all* detected events, (2) the largest 50%, (3) the largest 10% and (4) the largest 2% of detected events, (5) distribution of all 10-90% rise times, and (6) a joint amplitude and 10-90% rise time distribution. Three different SSD (sum of signed deviations)-based scores were calculated based on the amplitudes of (1) the largest 50%, (2) the largest 10%, and (3) the largest 2% of detected events. These latter scores constrained high-amplitude (but low count) tails of 'simulated' distributions to have sufficient counts to avoid negative distribution deviations ('simulated' – 'real').

To ensure good fits to *all* portions of the histograms, and to prevent 'dilution' or 'swamping' effects on the high amplitude (but low event frequency) tail by the low amplitude, high frequency 'hump', the smallest 'global' percentile (same for every measure) was estimated, that guaranteed to include *half* of all single-sweep file pairings (real vs. real data) with *all* their 15 respective SAD, MAD, and SSD score values falling below this percentile threshold *simultaneously* ('15-score combined 50th centile'; Tables 1 and 2). This centile estimate was used to determine cut-off values for all these 15 different scores, to construct the optimisation cost function. The 'global' centile value from single sweep file comparisons was then used with SAD and MAD scores from longer files during the GA-controlled

384 fitting procedure (typically 5 recording sweep-long files to match the size of the 'noise-alone'
385 recording files, 100 s typically).
386
387 The cost function was constructed of 6 types of SAD scores and 6 types of MAD scores estimated
388 using the '15-score combined 50th centile' procedure and 3 types of SSD scores. These 15 scores
389 were used to evaluate how close the 'simulated' distribution was to the single selected 'real'
390 distribution that was deemed to be of the best quality by a human observer (Figures 4A and B).
391 Typically, it was a file close to the *end* of the 'noise with minis' recording epoch, therefore, being the
392 most similar file, in terms of recording quality parameters, to the 'noise-alone' recording epoch
393 (which was generally the *first* good-quality epoch safely *after* pharmacological blockade of
394 neurotransmission was deemed complete). An additional corresponding 15 'envelope deviation'
395 scores (same as SADs, MADs, and SSDs but comparing to the envelope or lower and upper range
396 limits of superimposed all available data distributions within that pharmacological epoch) were
397 calculated assessing how much each 'real' or 'simulated' distribution deviated from the full set
398 consisting of all the remaining 'real' distributions and the single 'simulated' distribution (Figures 4C
399 and D). The 'simulated' distribution was expected to have lower deviation scores than the worst
400 performing (most discrepant from the others) 'real' distribution (so the simulated distribution would
401 not be picked as the 'worst outlier' by a double-blind observer).
402
403 'Simulated' distributions were further penalised if their underlying source 'simulated minis'
404 distribution was non-unimodal, had a 10-90% rise time mean larger than 5 ms, or it violated a 10-
405 90% rise time skewness constraint that the mean 10-90% rise time of simulated minis should exceed
406 the median at least by a quarter of the standard deviation, as seen for the real minis (with noise)
407 distributions (range of 0.25 to 0.39 standard deviations). Finally, 'simulated' distributions were also
408 penalised if their underlying 'simulated minis' amplitude distribution had a sharp cliff at its lower

end. Hence, together with the four shape constraints there were 34 fitness components in total (15 + 15 + 4 = 34).

If all SAD, MAD, SSD, deviation scores, and shape constraints for comparing the 'simulated' distribution to the 'real' distributions were satisfied (≤ 15-score 50th centile SAD and MAD cutoff values and ≥0 SSD values) at the end of the fitting procedure, the fit was deemed to be the 'best possible' (a 'very good match', by all criteria). Alternatively, the fit could also be deemed 'acceptable' if all amplitude SAD, MAD, and SSD scores, as well as the distribution unimodality constraint were satisfied (excluding 10-90% rise time scores, all 'envelope deviation' scores, and the distribution skewness and 'cliff' constraints). The 'best' and 'acceptable' fits comprised the set of 'good enough' fits in terms of their GA-optimised 'fitness' which, however, did not guarantee a statistically acceptable fitness.

Final test for distribution acceptance or rejection

The notion of a 'good enough' fit is somewhat arbitrary, so far. Once the fitting procedure was completed, we set out to check whether the final fit was objectively acceptable using statistical tests. We divided the full available length of the 'noise with real minis' recording condition (epoch) into smaller files of the same length as the selected 'noise-alone' recording file and constructed a *set* of (independent) 'real' ('noise with real minis') distributions (histograms) by running the 'minis' detection algorithm on all these files (which we term the 'real distribution set'). We then compared these individual 'real' distributions to each other, pairwise, by subtracting their marginal ('1-D') amplitude and 10-90% rise time distributions from each other, taking the absolute value of the differences, and summing over all bins (bin sizes of 10 µV and 0.5 ms; bin counts were normalised by the average bin count over all 'real' distributions to increase the weight of distribution tails). So we ended up with amplitude (Figure 6A) and 10-90% rise time (Figure 6B) sets of SAD scores for each distribution (individual file) within the 'distribution set' (the 'real-real SAD score sets'; there is an

amplitude and a rise time ‘real-real SAD score set’ for each distribution within the ‘distribution set’ corresponding to individual lines in Figures 6A and B). The number of SAD scores in each ‘real-real SAD score set’ corresponded to the number of possible comparisons between the distribution (file) of interest and the rest of the distributions (files) = n - 1 (given n different files). Finally, we selected the ‘worst’ (‘most discrepant’) and the ‘best’ (‘least discrepant’ compared to the others) ‘real’ reference distributions (files; the top and the bottom rows of SAD score matrices in Figures 6A and B, respectively), in terms of their median SAD scores (median over all SADs in the ‘real-real SAD score set’ for that distribution). Therefore, we were left with only two sets: The ‘worst real-real SAD set’ and ‘the best real-real SAD set’.

We also compared the ‘good enough so far’ (‘work-in-progress’) ‘noise with simulated minis’ distribution to all the non-reference ‘real’ (‘noise with *real* minis’) distributions. The comparison yielded another set of SAD scores: the ‘simulated-real SAD score set’ (Figures 6C and D). The median of this was then compared to the medians of the ‘worst real-real SAD score set’ and the ‘best real-real SAD score set’ using the non-parametric Wilcoxon signed-rank paired samples test. If the median score of the ‘simulated-real SAD score set’ was significantly larger than the median score of the ‘*worst* real-real SAD score set’, (i.e. if the distributions actually were identical, that discrepancy or more would only have occurred purely by chance less than 5% of the time; Bonferroni-corrected for a requirement to simultaneously satisfy both amplitude and 10-90% rise time tests), the ‘simulated’ distribution was deemed to be an inadequate fit and, was therefore rejected and the fitting procedure continued. (By contrast, if the median score of the ‘simulated-real SAD score set’ was significantly *smaller* than the median score of the ‘*best* real-real SAD score set’, the ‘simulated’ distribution was deemed likely to be an “excellent” fit; however, ‘passing’ this test was not strictly required and was used only for guidance). The ‘work-in-progress’ ‘good enough’ fit was ultimately accepted if the median of the ‘simulated-real SAD score set’ was *not* significantly larger than the median of the ‘worst (most discrepant) real-real SAD score set’. Intuitively, this corresponds

(roughly) to a double-blind observer not being able to pick out that (simulated minis with real noise) distribution (histogram) from the (real minis with real noise) data distributions (histograms): it was not (obviously) the 'most discrepant' histogram.

Statistical analyses

Parametric inferential statistics tests were used for incidence rates of minis (frequencies minis/s), mean amplitudes, and total cell membrane capacitances, as quantile-quantile ('Q-Q') plots indicated that these measures were normally distributed. Sums of absolute distribution bin deviations (SADs) were often not normally distributed as assessed by Q-Q plots, and therefore were tested using the corresponding non-parametric paired samples Wilcoxon signed-rank test.

Data accessibility

All data analysed in this study are publicly available (Dervinis, 2024a, 2024b). The available data include 'noise with minis' and 'noise-alone' whole-cell patch membrane potential recordings that were used in computer simulations and minis' distribution fitting, as well as GA distribution fitting results. All electrophysiological recordings were stored in Axon Binary File (ABF) format.

Code accessibility

All analyses were carried out in Matlab and the analysis code is publicly available on GitHub (Dervinis, 2024c). The code is complete with instructions on how to reproduce figures reported in this study.

Software accessibility

The present study reported the use of a novel quantal analysis method that is part of 'minis' software available on GitHub (Dervinis, 2024d).

Results

Estimating quantal size by direct subtraction of noise component

We have analysed 'noise with minis' recordings and 'noise-alone' recordings with the 'minis' detection algorithm. Detected mEPSP-like events had an amplitude and 10-90% rise time distributions that resembled log-normal or gamma distributions (Figure 7), left skewed with a long tail on the right. In the amplitude domain, the lower end of the distribution contains a mixture of real minis and noise fluctuations that were misidentified as real events (but also missing small minis cancelled out by noise, summating with larger minis, or failing to be detected due to being on a decay phase of a big preceding mini – the 'overshadowing' effect).

We initially tested whether the noise component (in 'noise with minis' recordings) could be reliably estimated based on the corresponding 'noise-alone' recording (where synaptic activity has been pharmacologically blocked), simply by directly subtracting the detected 'noise-alone' events distribution from the 'noise with minis' distribution, to yield an estimate of the pure minis' component. Figure 7A shows both 'noise with minis' and 'noise-alone' detected event amplitude distributions superimposed. After subtracting the 'noise-alone' distribution from the 'noise with minis' distribution there appear negative low amplitude bins in the resulting distribution (indicated by an arrowhead in Figure 7A). These missing low amplitude events are caused by a greater number of small false positive mini-like detections in the noise-alone traces, and larger minis overshadowing smaller minis and small amplitude noise fluctuations in the 'noise with minis' recording (we have discussed this phenomenon in more detail in our companion article (Dervinis and Major, 2024)). Therefore, the direct subtraction approach can only provide a relatively crude 'first order', high-end upper limit on the mean of the mini amplitude distribution. Nevertheless, this over-estimate is more reliable than a highly subjective approach of simply estimating the mean amplitude based on events detected using a high amplitude threshold, or worse still, detected manually, by what could, perhaps

uncharitably, be termed a “beauty contest” method (rather arduous, slow, subjective, and prone to human error/bias).

Estimating quantal size by simulating excitatory postsynaptic potential source distributions

An alternative and more reliable way of estimating the quantal size in our recordings is to estimate the minis component directly using simulations. This relies on the ‘minis’ optimisation algorithm (GA) being able to closely match a ‘noise with simulated minis’ voltage trace (Figure 3) with the ‘noise with real minis’ recordings in terms of amplitude and 10-90% rise time distributions of minis-like events detected within these traces. We were able to successfully do that for all our recordings (see Figure 8 and Supplementary Figures 15-27). In the example shown in Figure 8, the overall amplitude SAD of the ‘simulated’ distribution was not significantly larger than the worst-performing ‘real’ distribution (unidirectional ‘underfit’ test: Is ‘simulated’ median SAD significantly > worst-performing ‘real’ median SAD? Wilcoxon signed-rank paired samples test statistic $W (n = 16) = 105$, $p = 0.058$ (Bonferroni-corrected due to comparing once on amplitudes and once on rise times); a high W statistic indicates a high absolute distance between the two medians, irrespective of its sign/direction, while $p < 0.025$ would indicate fit rejection, due to a fit SAD score being larger than the worst SAD score than would be expected by chance alone, at that significance level; downward arrow indicates ‘simulated’ median SAD < ‘real’ median SAD relationship in Figure 8) and was not outperforming the best ‘real’ distribution (‘simulated’ median SAD < best-performing ‘real’ median SAD Wilcoxon signed-rank paired samples unidirectional ‘overfit’ test $W(16) = 135$, $p = 1$; upward arrow indicates ‘simulated’ median SAD > ‘real’ median SAD relationship in Figure 8). Similarly, the ‘simulated’ 10-90% rise time distribution was also neither an underfit (‘simulated’ median SAD > worst-performing ‘real’ median SAD unidirectional ‘underfit’ test $W(16) = 0$, $p = 1$) nor an overfit (‘simulated’ median SAD < best-performing ‘real’ median SAD unidirectional ‘overfit’ test $W(16) = 117$, $p = 1$).

538 All simulations produced ‘good enough’ matches showing amplitude and 10-90% rise time
539 distributions of detected minis-like events being within the range of (and thus indistinguishable
540 from) amplitude and 10-90% rise time count values measured in sets of ‘real event’ distributions
541 (Supplementary Figures 15-27). None of the fits performed significantly worse than the worst-
542 performing ‘real’ distribution, qualifying them as ‘good enough’ (accepted) fits. All resulting minis
543 source distributions are displayed in Figure 9 and Supplementary Figures 28-40. An example in
544 Figure 9 shows that the ‘real minis’ source distribution likely has a log-normal or gamma-like shape
545 in both amplitude and rise time domains.
546
547 Incidence rates (frequencies of minis per second) estimated based on simulated minis source
548 distributions ranged roughly between 10 and 100 minis/s (a mean of 27.3 ± 2.4 minis/s and a range
549 of 6.8 to 58.1 minis/s; Figure 10). This estimate is an order of magnitude higher than the one based
550 on the literature (3.6 minis/s; (Dervinis and Major, 2024)) and significantly higher than the one based
551 on the direct subtraction method (15.9 ± 0.9 minis/s; $t(13) = 3.51$, $p = 0.004$) and also higher than
552 the estimate based on amplitudes higher than a (deliberately chosen) unrealistically high detection
553 threshold of 0.8 mV (14.3 ± 0.9 minis/s; $t(13) = 3.69$, $p = 0.003$). It is precisely within the range
554 predicted in our companion article (Dervinis and Major, 2024). However, this range is possibly still
555 somewhat of an underestimate, as mini source distributions were often generated using a lower
556 limit on simulated amplitudes to constrain the distribution non-uniqueness, as discussed in the
557 Methods subsection on the distribution fitting (also see Supplementary Figure 14).
558
559 Mean amplitudes of minis derived using simulations ranged between 53 and 182.9 μV (overall mean
560 of 114.1 ± 5.5 μV, layer 2/3 mean of 133.1 ± 9.9 μV, and layer 5 mean of 95.1 ± 11.2 μV; Figure 11A).
561 When compared to capacitance estimates (or 1/capacitance), there was a strong (very tight)
562 correlation between each cell’s mean mEPSP amplitude and the inverse of its capacitance (which is
563 proportional to cell size, assuming capacitance per unit area is more or less a biological constant for

564 each cell class/type of membrane/density of channels with charged gates moving within the
565 membrane (Gentet et al., 2000); $r = 0.96$, $p = 7.1 \times 10^{-8}$, $R^2 = 0.92$). That is, the larger the cell, the
566 smaller the amplitude of its somatically detected minis and vice-versa. This relationship is predicted
567 by the theory of capacitors ($C = Q/V$, where C stands for capacitance, Q stands for charge, and V
568 stands for voltage across the cell's membrane), and it is a direct demonstration of an attenuating
569 effect of cell's capacitance on the amplitude of somatically detected minis. If a direct line was drawn
570 through the data and the origin of the axes in Figure 11A, the slope of this line would provide a
571 quantal size estimate for excitatory synapses in the CNS in terms of 'injected' charge ($Q = \Delta V/$
572 $\Delta(1/C)$) which is approximately equal to 31.3 fC, for these data. The fact that the least square fitted
573 line to the data ($y = 30.6x + 2.76$), with a negligibly small intercept term (2.76), roughly coincided
574 with the line through the origin fitted to the data ($y = 31.3x$) indicated that no obvious 'proactive'
575 mechanism *varying with cell size* was in place to compensate for the attenuation of the average
576 minis' amplitude due to the size of the cell.
577
578 Another notable observation was that the mean amplitude estimates derived either by noise
579 subtraction or by minis source distribution simulation were highly correlated ($r = 0.84$, $p = 1.49 \times 10^{-4}$,
580 $R^2 = 0.71$ Figure 11B). The equation of the line ($y = 1.37x – 65.9$) fitted to this data provides a
581 possible "shortcut" method to approximate the mean amplitude of fitted minis' source distribution
582 by inserting the mean estimated using 'naïve' noise subtraction directly into this equation.
583
584 *Generic miniature excitatory postsynaptic potential distribution in neocortex*
585 To construct a generic mEPSP distribution, we normalised amplitudes of simulated minis' source
586 distributions shown in Figure 9 and Supplementary Figures 28-40 by dividing them by their
587 respective means, taking the total average, and then scaling the amplitudes to the overall mean
588 (114.1 ± 5.5 μV). The resulting combined (amplitude and 10-90% rise time) distribution is shown in
589 Figures 12A and B. The corresponding marginal amplitude and 10-90% rise time distributions are

590 shown in Figures 12C and D, respectively. Both marginal distributions have left-skewed log-normal-
591 like or gamma-like distributions. This may be useful in neural network simulations, or to potentially
592 speed up (and constrain) fitting of simulated minis on noise to real minis with noise, using the GA
593 (e.g., limit the source distribution to one 2-D 'rotated' log-normal or gamma distribution).
594

595 # Discussion

596 We report two major scientific advances. First, a novel quantal analysis method based on sequential
597 somatic recording, from a given neuron, of a) mEPSPs (after blockade of action potential-mediated
598 neurotransmission, and all inhibitory neurotransmission, including mIPSPs) on a background of other
599 physiological noise, and b) subsequent recordings from the same cell of noise alone, after additional
600 pharmacological blockade of mEPSPs (all glutamatergic ionotropic excitatory neurotransmission).
601 The latter type of recording provides a means to estimate the properties of the noise component
602 which can then be used to take into account noise fluctuations in the combined minis and noise
603 recording. However, this was done not by a direct subtraction of the histogram of amplitudes
604 (and/or rise times) detected from the noise-alone recordings, but rather by the simulation of the
605 underlying minis component and repeatedly superimposing (at random) the waveforms of simulated
606 minis onto the noise trace, varying source distribution parameters until the histograms detected
607 from the 'noise with simulated minis' voltage trace closely matched those detected from the 'noise
608 with real minis' recording. The key tool for achieving this match was a genetic algorithm that
609 optimised the parameters of the 2-dimensional simulated minis distribution in terms of amplitudes
610 and 10-90% rise times (and rate, i.e. minis per second), simultaneously, to best fit the experimental
611 data distributions.
612

613 The second major advance was the application of our novel quantal analysis method, that
614 successfully measured the mean 'electric charge injected' size of excitatory synapses of cortical

615 pyramidal cells, which was shown to be approximately 31.3 fC, across the entire sample of
616 neocortical pyramidal neurons recorded. This number was inferred from the slope of the line which
617 tightly fitted mean mini amplitude vs. 1/total cell capacitance, in accordance with the theory of
618 capacitors. The fact that this line had an intercept at the origin of the axes indicated that there was
619 no biological compensation (other than *number* of synapses) for the amplitude attenuation of minis
620 due to cell size (i.e., total capacitance). Indeed, cell capacitance played a major role affecting the
621 *voltage* amplitude of mEPSPs, resulting in a large proportion of mEPSPs being otherwise
622 indistinguishable from noise (as independently found in numerous other studies, e.g. (Major et al.,
623 2013b; Nevian et al., 2007), summarised in (Major et al., 2013b)). The number of these 'missed'
624 minis was so high that the estimated minis' incidence rate (frequency) was in the order of 10-100
625 minis/s: an order of magnitude higher than typically reported in the synaptic physiology literature
626 (with the notable exception of (Nevian et al., 2007), which predicted this result, by simultaneous
627 dual somatic and basal dendritic whole-cell patch recordings of mEPSPs, with dendritic detection,
628 and simultaneous somatic measurement). Finally, both the amplitude and 10-90% rise time
629 distributions of minis had a left-skewed log-normal- or gamma-like shape.
630
631 These findings have some major implications. First, the method, as used for estimating the mEPSP
632 distributions in cortical layers 2/3 and 5 of cells of various size, and then using these distributions to
633 arrive at the electrical size of excitatory synapses, serves as a proof of principle that it can be
634 successfully used to estimate PSP distributions of various types in the CNS. The next logical step of
635 this method is to extend its application to the estimation of amplitude and rise time distributions of
636 mIPSPs generated by different types of inhibitory synapses and, as a result, their 'electrical sizes'.
637 Moreover, the ability to obtain relatively accurate 'quantal' size estimates unobscured by
638 physiological noise is important for constraining synaptic parameters in physiologically realistic
639 simulations of neural activity. For example, now we should be able to better estimate how many
640 active synapses are needed to generate an NMDA spike within a single dendritic segment (Major et

641 al., 2013b). The importance of these number estimates is not restricted to the domain of
642 physiologically realistic simulations but also extends to more abstract computations that use NMDA
643 spike-like mechanisms as coincidence detectors in the latest cortically inspired/constrained models
644 of artificial intelligence (Hawkins et al., 2019). Accurate estimates of synaptic transmission
645 parameters thus have very wide-reaching ramifications.
646
647 These findings also draw attention to some possible methodological issues in the field of synaptic
648 physiology. As discussed in our companion article (Dervinis and Major, 2024), the reported incidence
649 rates ('frequencies') for mEPSCs are generally well below 10 minis/s. Even if one doubts the
650 incidence rates we arrived with simulations, in the range of 10-100 minis/s, the rates given by 'naïve'
651 direct subtraction of the distribution of events detected in the 'noise-alone' recording from the
652 distribution based on the 'noise with minis' recording is still within 5.9 to 26.7 minis/s, which we
653 know to be an underestimate. Therefore, reported mini incidence rates below 10 minis/s are almost
654 certainly underestimates. This may have multiple causes, including lower slice temperatures in the
655 majority of studies (we used physiological, ca. 37 °C), and a significant temperature dependence of
656 synaptic release, as well as differences in slice health and slicing angle (which can affect branch and
657 local circuit 'amputations'). Another big cause could be the use of voltage clamp, especially if the
658 series resistance is not compensated fully, as this low-pass filters traces and obscures smaller minis.
659 As discussed earlier, these estimates could be improved by switching to voltage recording instead of
660 using voltage clamp (Major, 1993a; Rall and Segev, 1985; Spruston et al., 1993; Williams and
661 Mitchell, 2008) but at the price of somewhat slower decay times of minis (Major 1993), thus more
662 temporal overlap/integration and consequent difficulties detecting peaks. But more importantly, a
663 strong association between cell capacitance (i.e. surface area) and the extent to which somatically
664 recorded minis' amplitudes are attenuated, indicates that special care must be taken to account for
665 the effect of background noise fluctuations on the amplitude measurements - as we have done here.
666 This association is yet more evidence supporting experimental observations of massive mini

667 amplitude attenuation as the PSP spreads from its dendritic source location to the soma (Larkum et
668 al., 2009; Major et al., 2013a; Nevian et al., 2007; Stuart and Spruston, 1998; Williams and Mitchell,
669 2008; Williams and Stuart, 2002), especially in cells with large dendritic arbours, hence large surface
670 areas and overall membrane capacitance. Dendritic spines and post-synaptic densities (the
671 specialised regions opposite release sites, containing high densities of synaptic receptors, with a
672 substantial fraction tethered to the cytoskeleton) are not grossly different in size between different
673 classes of pyramidal neurons in the neocortex, although differences exist between cortical layers,
674 cortical areas, and, particularly, species (Yuste, 2010).
675
676 It is also worth noting that understanding the link between cell capacitance and somatically
677 recorded average mini amplitudes, as well as knowing actual shapes of mini distributions in terms of
678 their amplitudes and rise times, allows us to generate artificial data where the 'ground truth' is
679 known. Such labelled data could perhaps be used to train artificial neural networks (ANNs) which
680 could then be used to develop 'next generation' quantal analysis methods allowing detection of
681 minis directly in mixed 'noise with minis' recordings. We are not the first to suggest the application
682 of ANNs to this issue (see (Pircher et al., 2022) and (Wang et al., 2024)). However, we are not aware
683 of attempts to use realistic mini distributions for this purpose.
684
685 Even though the novel quantal analysis method we present here is an important advance, it
686 nevertheless has limitations. One of them is the need for (relatively) long duration recordings using
687 different pharmacological agents at various stages. However, the somatic recording set up is not as
688 complicated and high-skill as an alternative multisite 2-photon targeted dendritic recording set up
689 would be (Nevian et al., 2007), a heroic technique which has not to our knowledge been reproduced
690 in another lab. Experiments themselves could be further streamlined, as we did in some cases, by
691 pre-blocking action potentials before obtaining the whole-cell recordings, and using high solution
692 perfusion rates. This is particularly useful for smaller cells which are more prone to osmotic

overloading or shrinkage and resulting recording instability after a few tens of minutes (the pipette solution cannot exactly reproduce the cytoplasm, as it contains no proteins or other macromolecules, and is missing many common metabolites). Moreover, the distribution fitting procedure involving the GA can be lengthy and computationally intensive. However, the 'minis' software is parallelised at the PSP detection level, as well as at the GA optimisation level, making it particularly suitable to be executed on multi-core computing clusters. Although our 'minis' software combined with two-stage recordings offers unprecedented control for the background physiological noise, provided recording stability is very good throughout, we understand that many researchers may not be persuaded to adopt it themselves. The possibility of misleading fits if the recording noise became substantially worse between 'noise with minis' and 'noise-alone' recording phases needs to be vigilantly excluded. Nevertheless, our 'minis' software should still be useful for detecting mini-like events without recording independent noise, or fitting simulated to real distributions, if there is some other credible cut-off or separation method that can be used to distinguish between small or partially cancelled minis and mini-like noise. We anticipate, indeed, that, realistically, this scenario is likely to be its most popular use.

Some researchers may be critical of a method that does not rely on a direct measurement of minis but rather on an approximation via indirect means, using simulations. This is a valid criticism that could (perhaps) be addressed in the future by using a method of repeatedly subjecting a voltage recording to the minis detection procedure with an increasingly lower threshold while subtracting detected events from the voltage recording, or perhaps compensating for the 'exponential-like' decay phases of recent, temporally integrated, detected mini-like events. Some combination of these approaches could potentially recover most of the smaller minis that are 'overshadowed' by the larger ones (the so called 'negative bins' problem illustrated in Figure 7A), providing the waveforms were reasonably stereotyped in shape (not the case under voltage clamp, in neurons with large or extended or highly-branched dendritic arbours, (Major, 1993b)). Furthermore, other

719 researchers may question the ability to pharmacologically isolate the background physiological
720 noise. Our 'noise with minis' recordings may contain random openings of individual AMPA receptor
721 (AMPAR) or NMDA receptor (NMDAR) channels (possibly extra-synaptic) and our 'noise-alone'
722 recordings may fail to fully eliminate all channel openings in the presence of quantal release of
723 neurotransmitter (although we used high doses, well above IC50s' (Lehmann et al., 1987; Randle et
724 al., 1992) and rapid slice perfusion, to achieve quick wash-in times).
725 Background/physiological/electrical noise itself may also be drifting between two such (hypothetical)
726 conditions, with the presence or absence of mEPSP pharmacological blockers. Occasionally, we
727 rejected recordings (or epochs) with suspicious or obvious instabilities. These factors are unlikely to
728 have affected the results significantly, due to the small amplitudes of any remaining membrane
729 potential variations in the fitted cells. Two largely independent analyses of the same data by the two
730 authors separately yielded similar results and conclusions (albeit with somewhat different data
731 selection, sweep lengths, and tests of goodness of fits: the 'first pass', not presented here, relied
732 more on 'double-blind' visual inspection of multiple real minis with noise data distributions from the
733 same cell superimposed on the simulated minis with noise fit distribution: if the latter stood out
734 obviously from the crowd, it was rejected).
735
736 Despite some of the limitations discussed above, the method and its application to neocortical
737 excitatory connections presented in this article provide a useful advance in the field of synaptic
738 physiology. Logical next steps could include the application of this novel quantal analysis method to
739 establish the properties of other types of excitatory synapse, and various types of inhibitory synapse,
740 in both neocortex and hippocampus, and in other species, and to investigate whether average
741 synaptic 'size' (injected charge) is more widely conserved within different cell classes.

References

Bekkers JM. 1994. Quantal analysis of synaptic transmission in the central nervous system. *Curr Opin Neurobiol* **4**:360–365. doi:https://doi.org/10.1016/0959-4388(94)90097-3

Biró ÁA, Holderith NB, Nusser Z. 2005. Quantal Size Is Independent of the Release Probability at Hippocampal Excitatory Synapses. *The Journal of Neuroscience* **25**:223–232. doi:10.1523/JNEUROSCI.3688-04.2005

Brown TH, Wong RKS, Prince DA. 1979. Spontaneous miniature synaptic potentials in hippocampal neurons. *Brain Res* **177**:194–199. doi:https://doi.org/10.1016/0006-8993(79)90931-4

Clamann HP, Rioult-Pedotti MS, Luscher HR. 1991. The influence of noise on quantal EPSP size obtained by deconvolution in spinal motoneurons in the cat. *J Neurophysiol* **65**:67–75. doi:10.1152/jn.1991.65.1.67

Clements JD. 2003. Variance–mean analysis: a simple and reliable approach for investigating synaptic transmission and modulation. *J Neurosci Methods* **130**:115–125. doi:https://doi.org/10.1016/j.jneumeth.2003.09.019

Clements JD, Silver RA. 2000. Unveiling synaptic plasticity: a new graphical and analytical approach. *Trends Neurosci* **23**:105–113. doi:10.1016/S0166-2236(99)01520-9

del Castillo J, Katz B. 1954. Quantal components of the end-plate potential. *J Physiol* **124**:560–573. doi:https://doi.org/10.1113/jphysiol.1954.sp005129

Dervinis M. 2024a. https://gin.g-node.org/dervinism/minis-benchmarking-data2. *GIN*. doi:10.12751/g-node.mvsy4j

Dervinis M. 2024b. https://gin.g-node.org/dervinism/minis-quantal-analysis-data. *GIN*. doi:10.12751/g-node.32m2ge

Dervinis M. 2024c. https://github.com/dervinism/minis-quantal-analysis. *GitHub*. doi:10.5281/zenodo.14288653

Dervinis M. 2024d. https://github.com/dervinism/minis. doi:10.5281/zenodo.14573132

Dervinis M, Major G. 2024. A novel method for reliably measuring miniature and spontaneous postsynaptic potentials/currents in whole-cell patch clamp recordings in the central nervous system. *bioRxiv*. doi:10.1101/2022.03.20.485046

Edwards FR, Redman SJ, Walmsley B. 1976. Statistical fluctuations in charge transfer at Ia synapses on spinal motoneurones. *J Physiol* **259**:665–688. doi:https://doi.org/10.1113/jphysiol.1976.sp011488

Enoki R, Hu Y, Hamilton D, Fine A. 2009. Expression of Long-Term Plasticity at Individual Synapses in Hippocampus Is Graded, Bidirectional, and Mainly Presynaptic: Optical Quantal Analysis. *Neuron* **62**:242–253. doi:10.1016/j.neuron.2009.02.026

Farsi Z, Walde M, Klementowicz AE, Paraskevopoulou F, Woehler A. 2021. Single synapse glutamate imaging reveals multiple levels of release mode regulation in mammalian synapses. *iScience* **24**. doi:10.1016/j.isci.2020.101909

Fatt P, Katz B. 1952. Spontaneous subthreshold activity at motor nerve endings. *J Physiol* **117**:109–128.

Forti L, Bossi M, Bergamaschi A, Villa A, Malgaroli A. 1997. Loose-patch recordings of single quanta at individual hippocampal synapses. *Nature* **388**:874–878. doi:10.1038/42251

Gentet LJ, Stuart GJ, Clements JD. 2000. Direct Measurement of Specific Membrane Capacitance in Neurons. *Biophys J* **79**:314–320. doi:https://doi.org/10.1016/S0006-3495(00)76293-X

Hardingham NR, Read JCA, Trevelyan AJ, Nelson JC, Jack JJB, Bannister NJ. 2010. Quantal Analysis Reveals a Functional Correlation between Presynaptic and Postsynaptic Efficacy in Excitatory Connections from Rat Neocortex. *The Journal of Neuroscience* **30**:1441–1451. doi:10.1523/JNEUROSCI.3244-09.2010

Hawkins J, Lewis M, Klukas M, Purdy S, Ahmad S. 2019. A Framework for Intelligence and Cortical Function Based on Grid Cells in the Neocortex. *Front Neural Circuits* **12**. doi:10.3389/fncir.2018.00121

Heuser JE, Reese TS, Dennis MJ, Jan Y, Jan L, Evans L. 1979. Synaptic vesicle exocytosis captured by quick freezing and correlated with quantal transmitter release. *Journal of Cell Biology* **81**:275–300. doi:10.1083/jcb.81.2.275

Isaacson JS, Walmsley B. 1995. Counting quanta: Direct measurements of transmitter release at a central synapse. *Neuron* **15**:875–884. doi:10.1016/0896-6273(95)90178-7

Jack JJ, Redman SJ, Wong K. 1981. The components of synaptic potentials evoked in cat spinal motoneurones by impulses in single group Ia afferents. *J Physiol* **321**:65–96. doi:https://doi.org/10.1113/jphysiol.1981.sp013972

Jonas P, Major G, Sakmann B. 1993. Quantal components of unitary EPSCs at the mossy fibre synapse on CA3 pyramidal cells of rat hippocampus. *J Physiol* **472**:615–663. doi:https://doi.org/10.1113/jphysiol.1993.sp019965

Katz B. 1969. The Release of Neural Transmitter Substances. Liverpool: Liverpool Univ. Press.

Korn H, Faber DS. 1991. Quantal analysis and synaptic efficacy in the CNS. *Trends Neurosci* **14**:439–445. doi:https://doi.org/10.1016/0166-2236(91)90042-S

Kraszewski K, Grantyn R. 1992. Unitary, quantal and miniature gaba-activated synaptic chloride currents in cultured neurons from the rat superior colliculus. *Neuroscience* **47**:555–570. doi:https://doi.org/10.1016/0306-4522(92)90165-X

Kullmann DM, Nicoll RA. 1992. Long-term potentiation is associated with increases in quantal content and quantal amplitude. *Nature* **357**:240–244. doi:10.1038/357240a0

Kuno M. 1964. Quantal components of excitatory synaptic potentials in spinal motoneurones. *J Physiol* **175**:81–99. doi:https://doi.org/10.1113/jphysiol.1964.sp007504

Larkman A, Stratford K, Jack J. 1991. Quantal analysis of excitatory synaptic action and depression in hippocampal slices. *Nature* **350**:344–347. doi:10.1038/350344a0

Larkum ME, Nevian T, Sandler M, Polsky A, Schiller J. 2009. Synaptic Integration in Tuft Dendrites of Layer 5 Pyramidal Neurons: A New Unifying Principle. *Science (1979)* **325**:756–760. doi:10.1126/science.1171958

Lehmann J, Schneider J, McPherson S, Murphy DE, Bernard P, Tsai C, Bennett DA, Pastor G, Steel DJ, Boehm C. 1987. CPP, a selective N-methyl-D-aspartate (NMDA)-type receptor antagonist: characterization in vitro and in vivo. *Journal of Pharmacology and Experimental Therapeutics* **240**:737–746.

Liu Z, Lu X, Villette V, Gou Y, Colbert KL, Lai S, Guan S, Land MA, Lee J, Assefa T, Zollinger DR, Korympidou MM, Vlasits AL, Pang MM, Su S, Cai C, Froudarakis E, Zhou N, Patel SS, Smith CL, Ayon A, Bizouard P, Bradley J, Franke K, Clandinin TR, Giovannucci A, Tolias AS, Reimer J, Dieudonné S, St-Pierre F. 2022. Sustained deep-tissue voltage recording using a fast indicator evolved for two-photon microscopy. *Cell* **185**:3408-3425.e29. doi:10.1016/J.CELL.2022.07.013

Major G. 1993a. Solutions for transients in arbitrarily branching cables: III. Voltage clamp problems. *Biophys J* **65**:469–491. doi:10.1016/S0006-3495(93)81039-7

Major G. 1993b. Solutions for transients in arbitrarily branching cables: III. Voltage clamp problems. *Biophys J* **65**:469–491. doi:10.1016/S0006-3495(93)81039-7

Major G, Evans JD, Jack JJ. 1993. Solutions for transients in arbitrarily branching cables: I. Voltage recording with a somatic shunt. *Biophys J* **65**:423–449. doi:10.1016/S0006-3495(93)81037-3

Major G, Larkum ME, Schiller J. 2013a. Active Properties of Neocortical Pyramidal Neuron Dendrites. *Annu Rev Neurosci* **36**:1–24. doi:10.1146/annurev-neuro-062111-150343

Major G, Larkum ME, Schiller J. 2013b. Active Properties of Neocortical Pyramidal Neuron Dendrites. *Annu Rev Neurosci* **36**:1–24. doi:10.1146/annurev-neuro-062111-150343

Nevian T, Larkum ME, Polsky A, Schiller J. 2007. Properties of basal dendrites of layer 5 pyramidal neurons: a direct patch-clamp recording study. *Nat Neurosci* **10**:206–214. doi:10.1038/nn1826

Oertner TG, Sabatini BL, Nimchinsky EA, Svoboda K. 2002. Facilitation at single synapses probed with optical quantal analysis. *Nat Neurosci* **5**:657–664. doi:10.1038/nn867

Peled ES, Isacoff EY. 2011. Optical quantal analysis of synaptic transmission in wild-type and rab3-mutant Drosophila motor axons. *Nat Neurosci* **14**:519–526. doi:10.1038/nn.2767

Pircher T, Pircher B, Feigenspan A. 2022. A novel machine learning-based approach for the detection and analysis of spontaneous synaptic currents. *PLoS One* **17**:1–16. doi:10.1371/journal.pone.0273501

Rall W. 1977. Core Conductor Theory and Cable Properties of Neurons In: Kandel ER, Brookhardt JM, Mountcastle VM, editors. Handbook of Physiology, Cellular Biology of Neurons. Bethesda, MD: American Physiological Society. pp. 39–97.

Rall W, Segev I. 1985. Space-clamp problems when voltage clamping branched neurons with intracellular microelectrodes In: T. G. Smith Jr, Lecar H, Redman SJ, Gage P, editors. Voltage and Patch Clamping with Microelectrodes. Bethesda, MD: American Physiological Society. pp. 191–215.

Randle JCR, Guet T, Cordi A, Lepagnol JM. 1992. Competitive inhibition by NBQX of kainate/AMPA receptor currents and excitatory synaptic potentials: importance of 6-nitro substitution. *Eur J Pharmacol* **215**:237–244. doi:https://doi.org/10.1016/0014-2999(92)90033-Z

Redman S. 1990. Quantal analysis of synaptic potentials in neurons of the central nervous system. *Physiol Rev* **70**:165–198. doi:10.1152/physrev.1990.70.1.165

858 Reid CA, Clements JD. 1999. Postsynaptic expression of long-term potentiation in the rat dentate
859 gyrus demonstrated by variance-mean analysis. *J Physiol* **518**:121–130.
860 doi:https://doi.org/10.1111/j.1469-7793.1999.0121r.x

861 Sahara Y, Takahashi T. 2001. Quantal components of the excitatory postsynaptic currents at a rat
862 central auditory synapse. *J Physiol* **536**:189–197. doi:https://doi.org/10.1111/j.1469-
863 7793.2001.00189.x

864 Silver RA. 2003. Estimation of nonuniform quantal parameters with multiple-probability fluctuation
865 analysis: theory, application and limitations. *J Neurosci Methods* **130**:127–141.
866 doi:https://doi.org/10.1016/j.jneumeth.2003.09.030

867 Spruston N, Jaffe DB, Williams SH, Johnston D. 1993. Voltage- and space-clamp errors associated
868 with the measurement of electrotonically remote synaptic events. *J Neurophysiol* **70**:781–802.
869 doi:10.1152/jn.1993.70.2.781

870 Stern P, Edwards FA, Sakmann B. 1992. Fast and slow components of unitary EPSCs on stellate cells
871 elicited by focal stimulation in slices of rat visual cortex. *J Physiol* **449**:247–278.
872 doi:https://doi.org/10.1113/jphysiol.1992.sp019085

873 Stuart G, Spruston N. 1998. Determinants of Voltage Attenuation in Neocortical Pyramidal Neuron
874 Dendrites. *The Journal of Neuroscience* **18**:3501–3510. doi:10.1523/JNEUROSCI.18-10-
875 03501.1998

876 Vere-Jones D. 1966. SIMPLE STOCHASTIC MODELS FOR THE RELEASE OF QUANTA OF TRANSMITTER
877 FROM A NERVE TERMINAL. *Australian Journal of Statistics* **8**:53–63.
878 doi:https://doi.org/10.1111/j.1467-842X.1966.tb00164.x

879 Wall MJ, Usowicz MM. 1998. Development of the quantal properties of evoked and spontaneous
880 synaptic currents at a brain synapse. *Nat Neurosci* **1**:675–682. doi:10.1038/3677

881 Wang N-S, Marino M, Malinow R. 2024. Detecting unitary synaptic events with machine learning.
882 *Proceedings of the National Academy of Sciences* **121**:e2315804121.
883 doi:10.1073/pnas.2315804121

884 Williams SR, Mitchell SJ. 2008. Direct measurement of somatic voltage clamp errors in central
885 neurons. *Nat Neurosci* **11**:790–798. doi:10.1038/nn.2137

886 Williams SR, Stuart GJ. 2002. Dependence of EPSP Efficacy on Synapse Location in Neocortical
887 Pyramidal Neurons. *Science (1979)* **295**:1907–1910. doi:10.1126/science.1067903

888 Yuste R. 2010. Dendritic Spines. The MIT Press. doi:10.7551/mitpress/9780262013505.001.0001

889 Yuste R, Majewska A, Cash SS, Denk W. 1999. Mechanisms of Calcium Influx into Hippocampal
890 Spines: Heterogeneity among Spines, Coincidence Detection by NMDA Receptors, and Optical
891 Quantal Analysis. *The Journal of Neuroscience* **19**:1976–1987. doi:10.1523/JNEUROSCI.19-06-
892 01976.1999

893

894

Figures

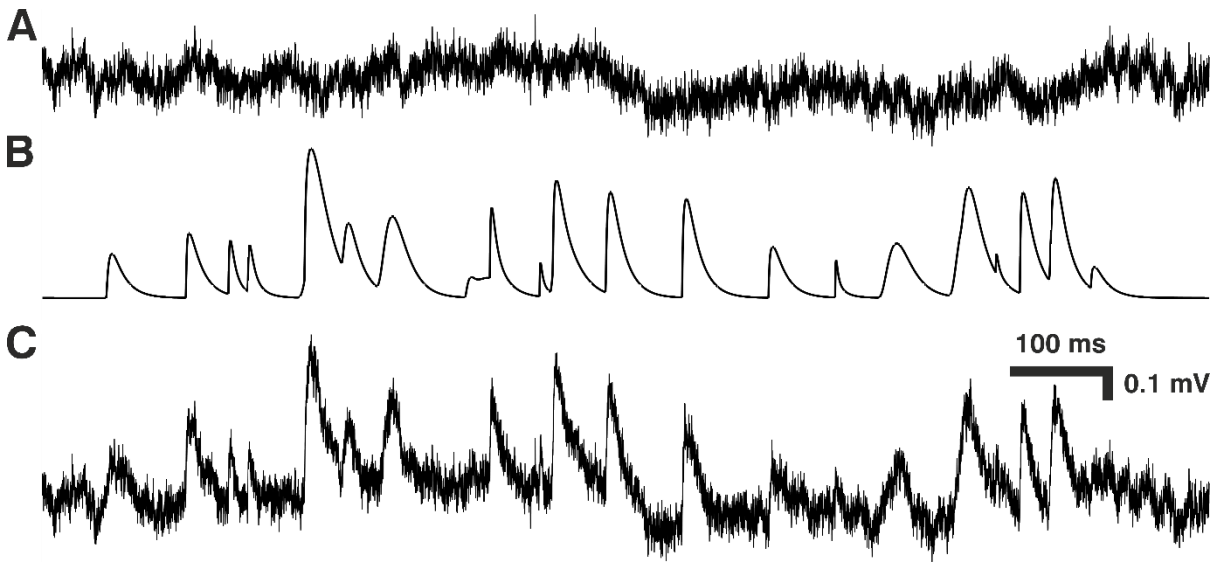

Figure 1: Constructing 'noise with simulated minis' voltage trace.

(A) Segment of 'noise-alone' voltage recording (from cortical layer 2/3 pyramidal neuron p131a).

(B) Simulated mEPSPs that were randomly added to the noise-alone trace in (A) to produce the 'real noise with simulated mEPSPs' voltage trace in (C).

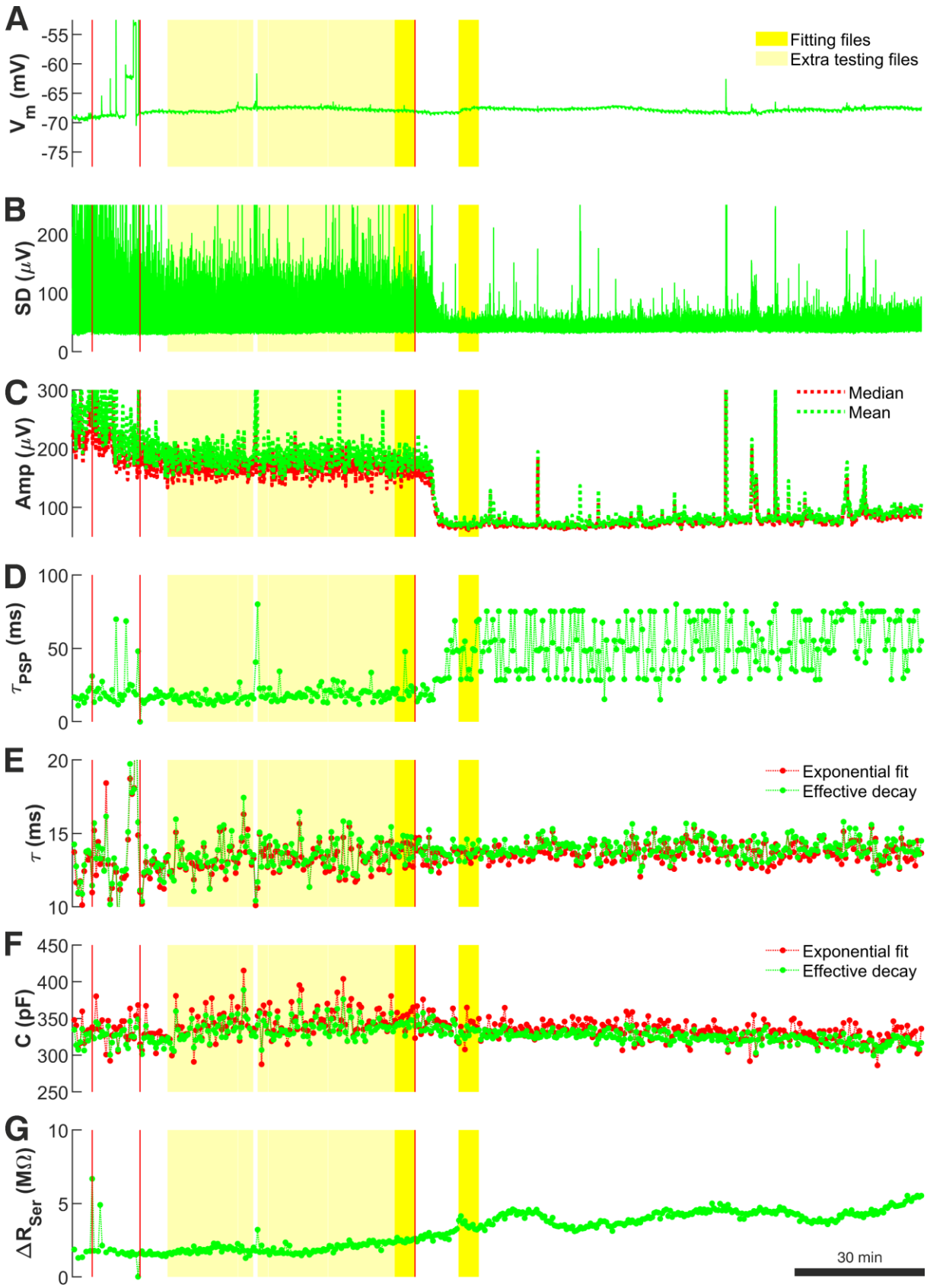

Figure 2: Recording quality measures used during the data preprocessing stage to select 'noise with

904 minis' and 'noise-alone' recording sweeps for further data analysis for recording p103a (layer 5
905 'burster' with tuft and thick trunk).
906 (A) Baseline V_m across the entire recording session. Stimulation pulses were excluded from the
907 display. The total recording duration (excluding pulse periods) was 8520 s. The first red vertical line
908 marks the time when pharmacological blockade of APs was initiated. The second red vertical line
909 marks the time when no more APs were observed in the recording. The third red vertical line marks
910 the time when pharmacological blockade of mEPSPs was initiated. Bright yellow periods mark 'noise
911 with minis' and 'noise-alone' recording segments selected as the main comparison files for the
912 distribution fitting. Light yellow marks all the remaining good quality 'noise with minis' recording
913 sweeps that were also included in the distribution fitting procedure for estimating target SAD, MAD,
914 and 'deviation' scores, as well as statistical evaluation of fits (see Methods).
915 (B) V_m standard deviation measured over consecutive 15 ms windows over the same recording
916 session.
917 (C) Evolution of mean and median amplitudes of the biggest top 10% of detected events (including
918 minis and noise events), averaged over single sweeps (duration of each was 4 s).
919 (D) Effective decay time constants (time to drop to 1/e of starting value 'safely' (8 ms) after the peak
920 and upwardly convex part) of the same biggest 10% of detected events as in panel (C) averaged over
921 consecutive 20-second-long (5-sweep-long) segments across the same session. Once minis were
922 blocked pharmacologically, effective time constant of detected events, (now pure noise) increased,
923 and its scatter, so this is another useful indication of when the block is complete.
924 (E) Evolution of passive membrane time constant over the entire recording session. Measurements
925 were averaged over consecutive 20-second-long (5-sweep-long) segments. Measurements based on
926 exponential decay curve fit and on 'effective time constant' (time for V_m to drop to 1/e of a value
927 just after change in current (after pipette capacitance artefact and fast charge redistribution
928 components: starting at 4 ms after the end of the pulse).

929 (F) Evolution of total cell membrane capacitance across the recording session. Measurements were
930 averaged over consecutive 20-second-long (5-sweep-long) segments. Measurements based on
931 exponential decay curve fit and on effective time constant (time taken for V_m drop to 1/e of an initial
932 value of the slowest impulse response component).
933 (G) Evolution of whole-cell pipette series resistance change (bridge balance error) across the
934 recording session, calculated from any jumps at starts or ends of charging curves. Measurements
935 were averaged over consecutive 4-second-long (5-sweep-long) segments.
936

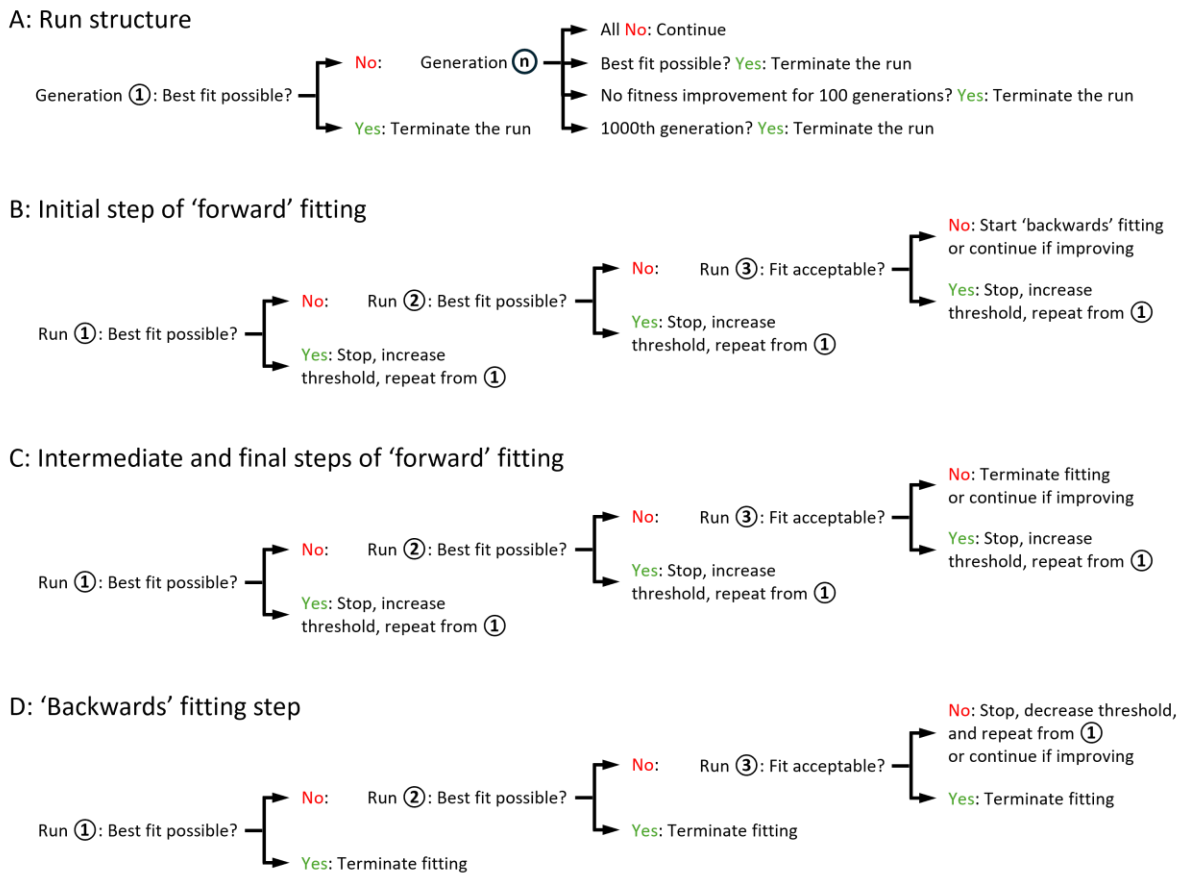

Figure 3: Schematic illustration of 'minis' genetic algorithm execution steps leading to the discovery of a minis source distribution underlying a distribution of minis-like events detected in a 'noise with minis' recording.

(A) The structure of a single GA run.

(B) The structure of the initial step of the 'forward' ('upward') fitting procedure where the lower threshold of the simulated minis amplitude is gradually raised.

(C) The structure of intermediate and final steps of the 'forward' ('upward') fitting procedure.

(D) The structure of the 'backwards' ('downwards') fitting procedure where the lower threshold of the simulated minis amplitude is gradually lowered.

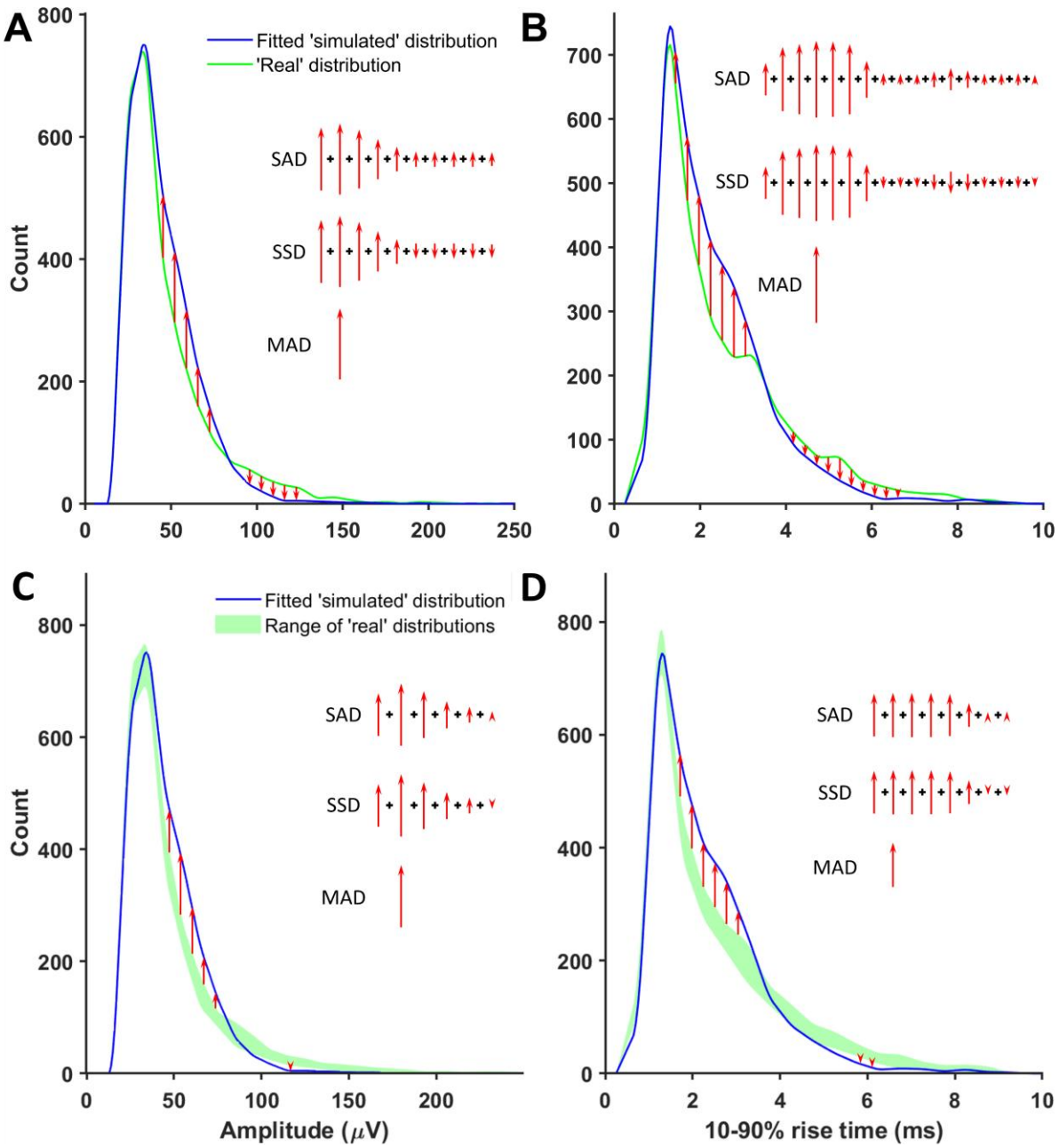

Figure 5: Non-shape components of the genetic algorithm's cost function.

(A) A schematic illustration of how amplitude SADs, MADs, and SSDs were calculated. Red arrows mark detected minis-like event count discrepancies between 'simulated' and 'real' 'noise with minis' distribution bins.

(B) A schematic illustration of how 10-90% rise time SADs, MADs, and SSDs were calculated.

(C) A schematic illustration of how amplitude 'envelope deviation' scores corresponding to SADs, MADs, and SSDs were calculated. Red arrows mark detected minis-like event count discrepancies

956 between the ‘noise with simulated minis’ distribution and the envelope of all superimposed ‘noise

957 with real minis’ distribution bins.

958 (D) A schematic illustration of how 10-90% rise time ‘envelope deviation’ scores corresponding to

959 SADs, MADs, and SSDs were calculated.

960

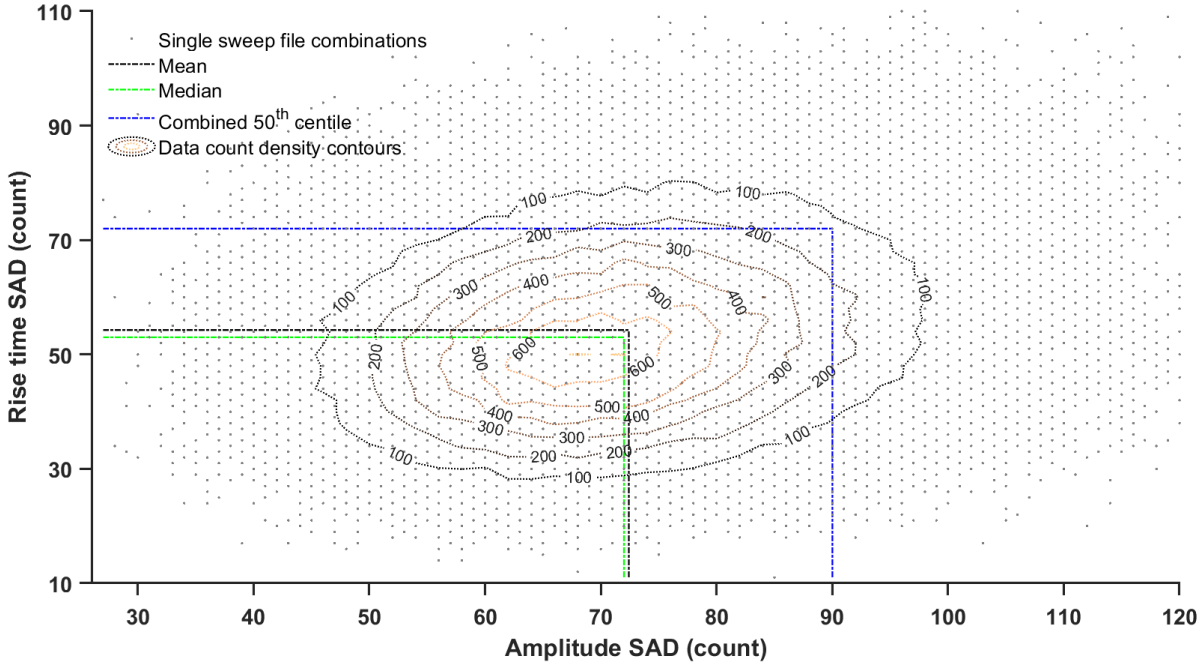

Figure 5: Amplitude and rise time scattergram (density plot) of sum of absolute deviation (SAD) scores between histograms from all possible pairs of 'noise with minis' single sweep files (4 s) from a layer 5 pyramidal neuron (p103a).

The line marking 'combined 50th centile' cutoff is based on 15 different SAD, SSD, and MAD scores as explained in Tables 1 and 2 (it extends to the remaining 13 dimensions not shown here). '15-score combined 50th centile' sets a lower (more exacting) threshold for accepting ('steering') distribution fits than the mean or the median would. This is justified because distribution fits need to satisfy all 15 SAD, SSD, and MAD scores *simultaneously* (e.g. to ensure that one of the tails of the distribution is not badly fit, as well as the remaining parts of the distribution).

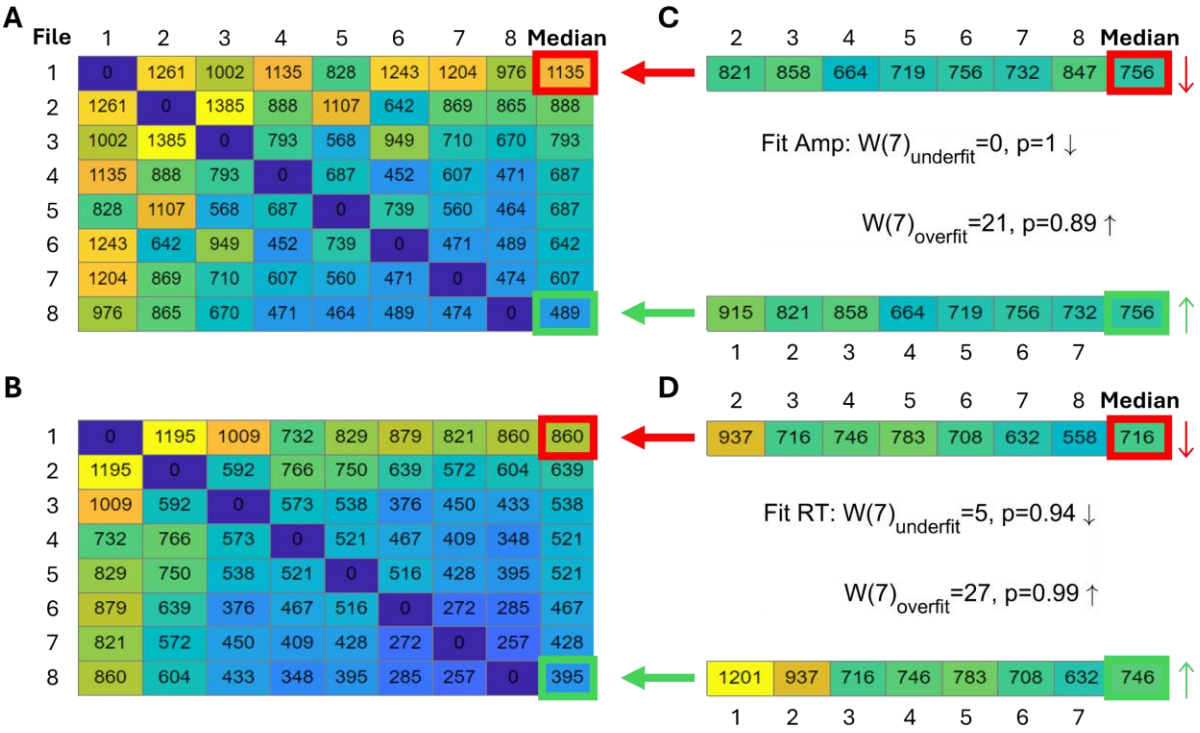

Figure 6: A schematic illustration of simulated minis distribution acceptance tests.

(A) A matrix showing amplitude SADs for all 'noise with real minis' recording file comparisons. The last matrix column shows the median SAD score for all comparisons in individual matrix rows. The matrix cell with thick red borders indicates the 'worst'-performing distribution, while the cell with thick green borders indicates the 'best'-performing distribution.

(B) A matrix showing 10-90% rise time SADs for all 'noise with real minis' recording file comparisons.

(C) Two sets of SADs for comparisons of the 'noise with simulated minis' amplitude distribution and all non-reference 'noise with real minis' amplitude distributions. The top vector contains comparisons with the same 'real' distributions/files as the top matrix row in (A) as indicated by the thick red arrow (the reference 'worst' distribution was excluded from the comparison). The thin red arrow points in the downward direction consistent with the 'simulated' median (right) being lower than the 'real' 'worst'-performing distribution's median (left). The bottom vector contains comparisons with the same 'real' distributions/files as the bottom matrix row in (A) as indicated by the thick green arrow (the reference 'best' distribution was excluded from the comparison). The thin green arrow points in the upward direction consistent with the 'simulated' median (right) being

988 higher than the ‘real’ ‘best’-performing distribution’s median (left). Results of the amplitude
989 acceptance Wilcoxon signed-rank paired samples test for the simulated minis distribution are shown
990 in the middle between the two SAD vectors. The top line tests whether the median of the SAD vector
991 top set in (C) is larger than the median in the red-bordered cell of the matrix in (A) ($W_{underfit}$; the
992 number of files/distributions minus the reference distribution is indicated within brackets). The
993 downward arrow indicates that the median of the SAD vector in (C) is smaller than the red-bordered
994 median in (A). The bottom line tests whether the median of the SAD vector bottom set is smaller
995 than the median in the green-bordered cell of the matrix in (A) ($W_{overfit}$). The upward arrow indicates
996 that the median of the SAD vector in (C) is larger than the green-bordered median in (A).
997 (D) A set of SADs and acceptance tests as in (C) but for the 10-90% rise time distribution of simulated
998 minis.
999

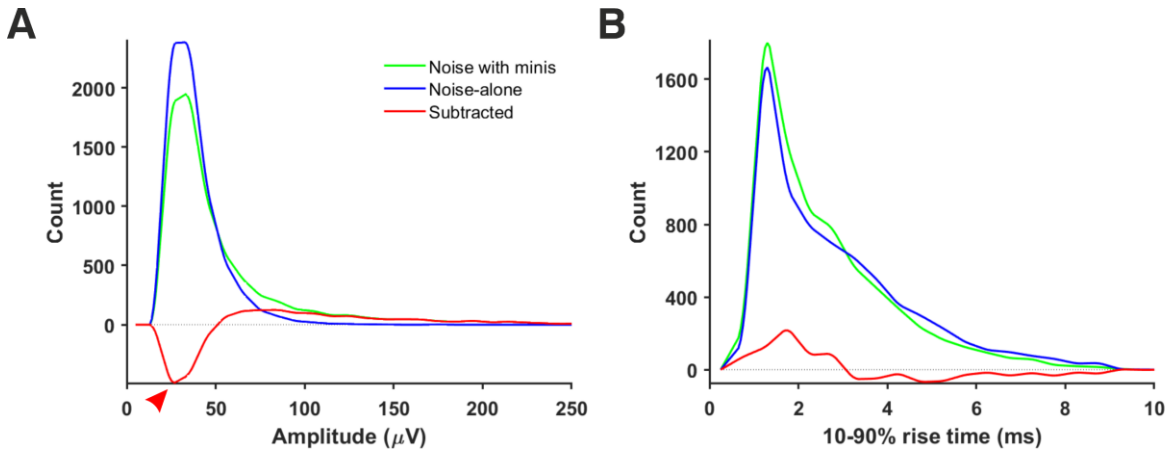

Figure 7: Amplitude and rise time distributions of detected mini-like events in 'noise with minis' and 'noise-alone' recordings.

(A) Amplitude distributions in a "thick" tufted neocortical layer 5 pyramidal neuron (p108b). Red arrowhead indicates negative bins after subtracting 'noise-alone' distribution from 'noise with minis' distribution.

(B) 10-90% rise time distributions from the same neuron.

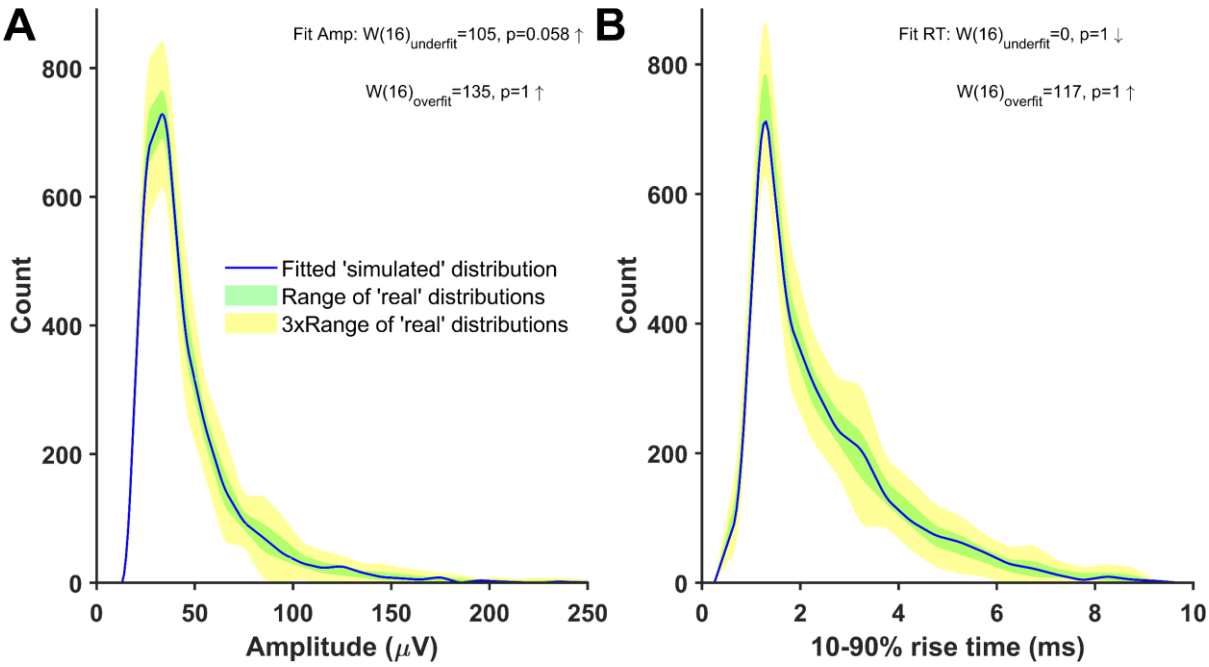

Figure 8: Distributions of mini-like events detected in a 'noise with simulated minis' voltage trace reasonably closely matching 'noise with real minis' recordings from the same cell, p106b (neocortical layer 5).

Parameters of simulated minis were controlled by the Genetic Algorithm. Up arrows indicate 'simulated' SAD > 'real' SAD; down arrows 'simulated' SAD < 'real'. The underfit test involves a comparison with the 'worst-performing' 'real' SAD (most discrepant from the others), whereas the overfit ('excellent fit') test involves a comparison with the 'best-performing' 'real' SAD (least discrepant from the others). With the underfit test (top), a fit SAD worse (bigger) than the 'real' SAD (up arrow), and $p < 0.05$ would mean the fit is rejected (not the case here: both amplitude and rise time fits (A and B) were accepted). (See Methods and Figure 6 for more details).

(A) Amplitude and (B) 10-90% rise time distributions (blue) of mini-like events detected in a 'noise with simulated minis' voltage trace, compared with 'envelopes' or bands (shaded) of all available 'real' data distributions from the neuron (taking the most extreme low and high values at each point across all the available data files recorded with both APs and IPSPs blocked).

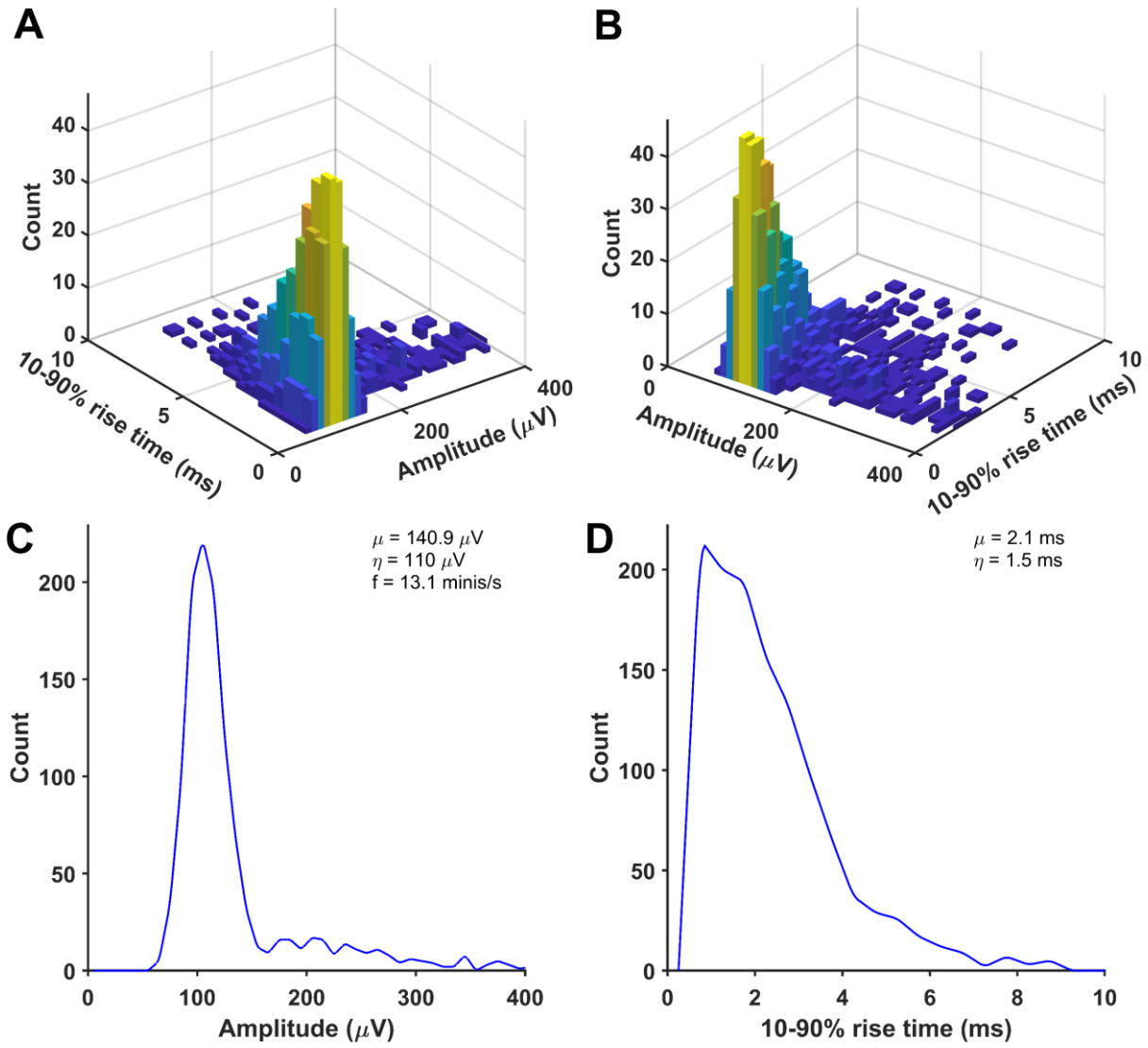

Figure 9: An example of a simulated minis distribution that was used to produce a close match between the distributions of detected mini-like events in a 'noise with simulated minis' voltage trace (with a 60 µV lower limit on simulated amplitudes) and a 'noise with real minis' recording, for a neocortical layer 2/3 cell (p131c).

(A) and (B) Joint amplitude and 10-90% rise time distribution of simulated minis, viewed from different angles.

(C) and (D) Corresponding 'marginal' (one-dimensional) amplitude and 10-90% rise time distributions, projected onto the axis indicated.

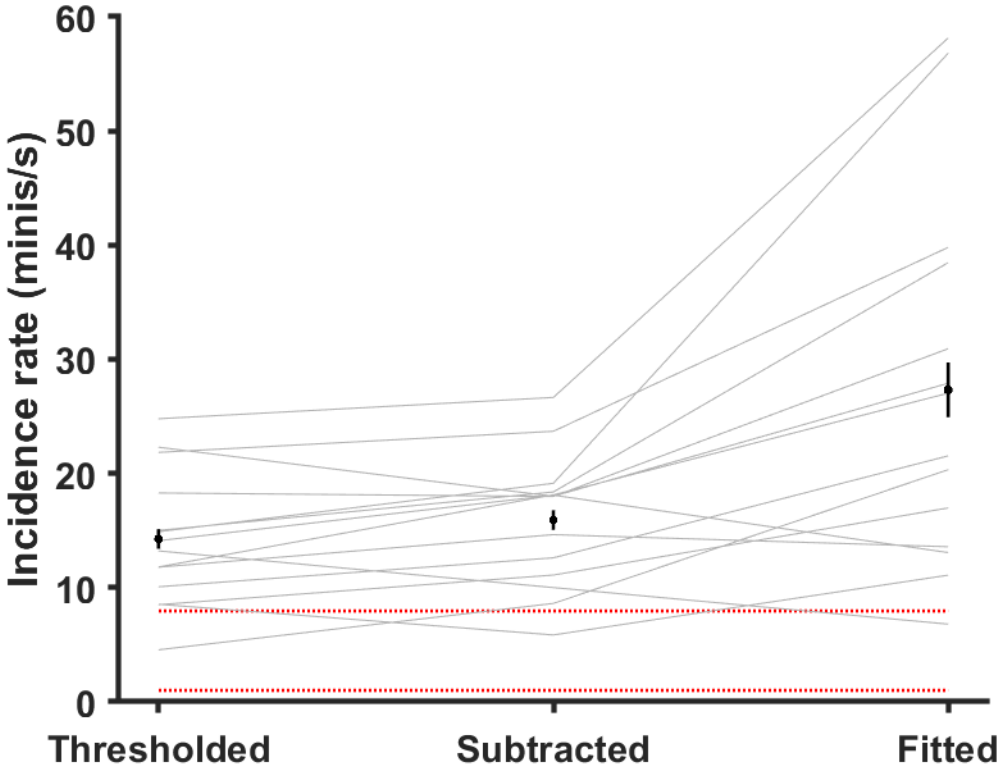

1033

1034 **Figure 10:** Estimated mEPSP incidence rates ('frequencies') using various methods (grey lines are

1035 individual cells).

1036 'Thresholded' method: an 'unreasonably high' 80 µV detection threshold was applied to all 14 'noise

1037 with real minis' recordings so only larger events were included.

1038 'Subtracted' method: the distribution of mini-like events in the 'noise-alone' recording was

1039 subtracted from the distribution of mini-like events in the 'noise with real minis' recording and the

1040 incidence rate estimate was based on the positive bins of the resulting distribution.

1041 'Fitted' method: the simulated minis distribution was used to estimate a lower bound on the mEPSP

1042 incidence rate (*lowest* acceptable rate statistically consistent with the real experimental data).

1043 Black markers and black vertical lines correspond to means and 95% confidence intervals. Red

1044 dotted lines mark the range of incidence rates typically reported in the literature; discussed in the

1045 companion article (Dervinis and Major, 2024).

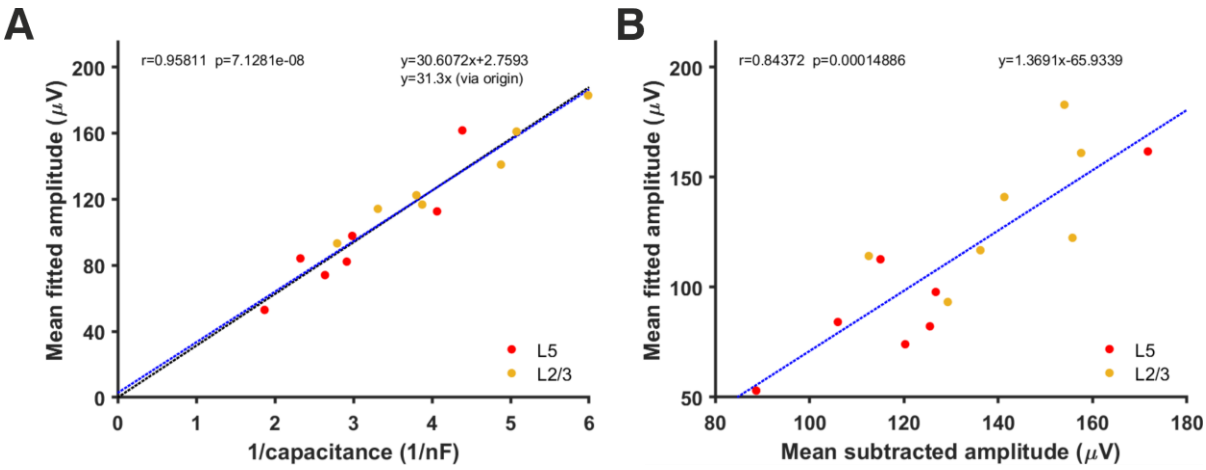

Figure 11: Relationship between each cell's inverse total membrane capacitance and its estimated mean mEPSP amplitude using simulations and fitting of minis distributions.

(A) Correlation between mean mini amplitudes from different neurons, as derived using the simulated minis distribution fitting method and the inverse of each cell's total capacitance. The blue line is the least square fit to the data while the (nearly indistinguishable) black line is the fit to the data that passes through the origin.

(B) Correlation between the mean mEPSP amplitude of each neuron estimated from 'fitting' versus 'subtracting' (the corresponding noise histogram, as in Figure 7).

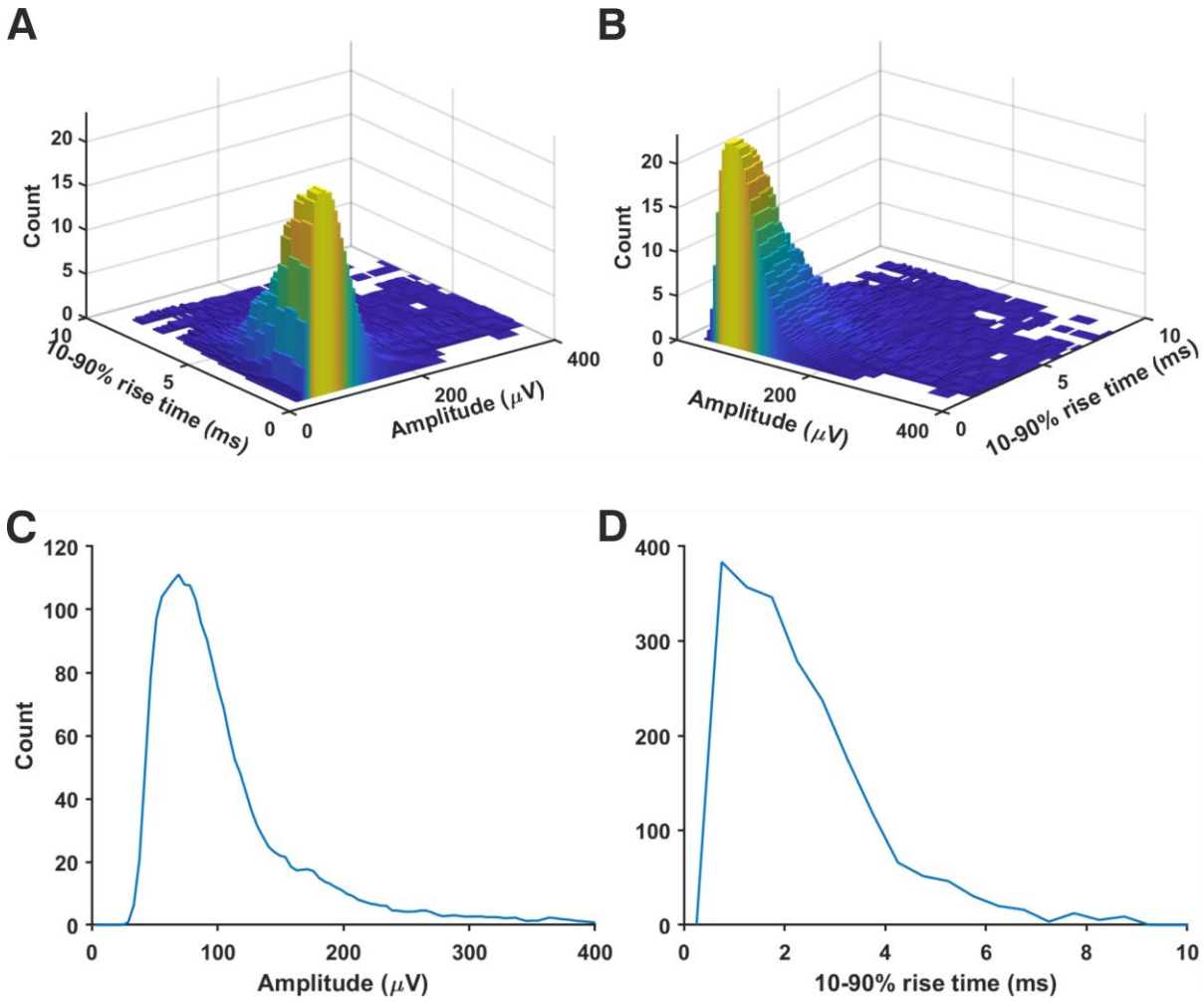

Figure 12: Generic 'averaged' mEPSP distribution from rat (somatosensory) neocortical pyramidal neurons.

Distributions resulting from all 14 recordings were averaged. All mini amplitudes were first normalised by the means of their respective source distributions, then multiplied by the average of the average amplitudes (114.1 ± 5.5 μV) across all the neurons analysed.

(A) A joint amplitude and 10-90% rise time distribution of simulated minis.

(B) The same distribution but viewed from a different angle.

(C) 'Marginal' (1-dimensional) amplitude distribution projected from the above distribution onto the amplitude axis.

(D) 'Marginal' 10-90% rise time distribution.

Tables

Amp SAD ≤56th centile?	Top 50% amp SAD ≤56th centile?	Top 10% amp SAD ≤56th centile?	Top 2% amp SAD ≤56th centile?	Top 50% amp SSD ≤0?	Top 10% amp SSD ≤0?	Top 2% amp SSD ≤0?	RT SAD ≤56th centile?	Joint SAD ≤56th centile?	Amp MAD ≤56th centile?	Top 50% amp MAD ≤56th centile?	Top 10% amp MAD ≤56th centile?	Top 2% amp MAD ≤56th centile?	RT MAD ≤56th centile?	Joint MAD ≤56th centile?
…	…	…	…	…	…	…	…	…	…	…	…	…	…	…
Yes	Yes	Yes	Yes	No	No	No	Yes	Yes	Yes	Yes	Yes	Yes	Yes	Yes
Yes	Yes	Yes	Yes	Yes	Yes	Yes	Yes	Yes	Yes	Yes	Yes	Yes	Yes	Yes
Yes	Yes	Yes	Yes	No	No	No	Yes	Yes	Yes	Yes	Yes	Yes	Yes	Yes
No	No	No	No	Yes	No	No	Yes	Yes	Yes	No	No	No	Yes	Yes
No	Yes	No	No	No	Yes	Yes	Yes	Yes	Yes	Yes	No	No	Yes	No
Yes	Yes	Yes	Yes	No	No	No	No	Yes	Yes	Yes	Yes	Yes	No	Yes
…	…	…	…	…	…	…	…	…	…	…	…	…	…	…

Table 1: Failed hypothetical attempt to use 56th centile as a basis for the combined '15-score 50th centile'.

The table shows a representative portion of a much bigger table illustrating a hypothetical scenario where the 15 SAD, SSD, and MAD scores are arranged in columns and rows corresponding to different two-file comparisons (many other comparisons are above and below those portrayed for the sake of the argument). SAD, SSD, and MAD scores are calculated by subtracting one file distribution from another (see the text for a detailed explanation). In this example, only *one* file comparison pair (green; 1/6 = 16.7%; row shaded in grey) satisfies the condition of having *all* its actual between-file SAD, SSD, and MAD values equal or below their respective 56th centile (across all comparison pairs - a unique value applying all the way down each column) – i.e. *simultaneously* in *all* columns. Therefore, the 56th percentile of each SAD, SSD, and MAD score would be too small to serve as the basis for the composite, joint or combined '15-score 50th centile': we need *half* the rows to be green, i.e. to pass the test.

Amp SAD ≤90th centile?	Top 50% amp SAD ≤90th centile?	Top 10% amp SAD ≤90th centile?	Top 2% amp SAD ≤90th centile?	Top 50% amp SSD ≤0?	Top 10% amp SSD ≤0?	Top 2% amp SSD ≤0?	RT SAD ≤90th centile?	Joint SAD ≤90th centile?	Amp MAD ≤90th centile?	Top 50% amp MAD ≤90th centile?	Top 10% amp MAD ≤90th centile?	Top 2% amp MAD ≤90th centile?	RT MAD ≤90th centile?	Joint MAD ≤90th centile?
…	…	…	…	…	…	…	…	…	…	…	…	…	…	…
Yes	Yes	Yes	Yes	Yes	Yes	Yes	Yes	Yes	Yes	Yes	No	No	No	Yes
Yes	Yes	Yes	Yes	Yes	Yes	Yes	Yes	Yes	Yes	Yes	Yes	Yes	Yes	Yes
Yes	Yes	Yes	Yes	Yes	Yes	Yes	Yes	Yes	Yes	Yes	Yes	Yes	Yes	Yes
Yes	Yes	Yes	Yes	Yes	Yes	Yes	Yes	Yes	Yes	Yes	Yes	Yes	Yes	No
Yes	Yes	Yes	Yes	Yes	Yes	Yes	Yes	Yes	Yes	Yes	Yes	Yes	No	No
Yes	Yes	Yes	Yes	Yes	Yes	Yes	Yes	Yes	Yes	Yes	Yes	Yes	Yes	Yes
…	…	…	…	…	…	…	…	…	…	…	…	…	…	…

Table 2: Using 90th SAD centile as a basis for the combined '15-score 50th centile'.

The table shows another example where the 15 SAD, SSD, and MAD scores are arranged in columns and rows correspond to different two-file comparisons. SAD, SSD, and MAD scores are calculated by subtracting one file distribution from another (see the text for a detailed explanation). Now *three* of the six file pairings (*half* of them: green; rows shaded in grey) satisfy the condition of having *all* their between-file SAD, SSD, and MAD scores equal or below their respective 90th centiles (across all comparison pairs - a unique number applying all the way down each column). Therefore, the 90th percentile works as the basis for the combined '15-score 50th centile'. Higher than 90 leads to more than half and lower than 90 leads to fewer than half of possible file pairs 'passing' all 15 tests simultaneously.

1085 **Supplementary Figures**

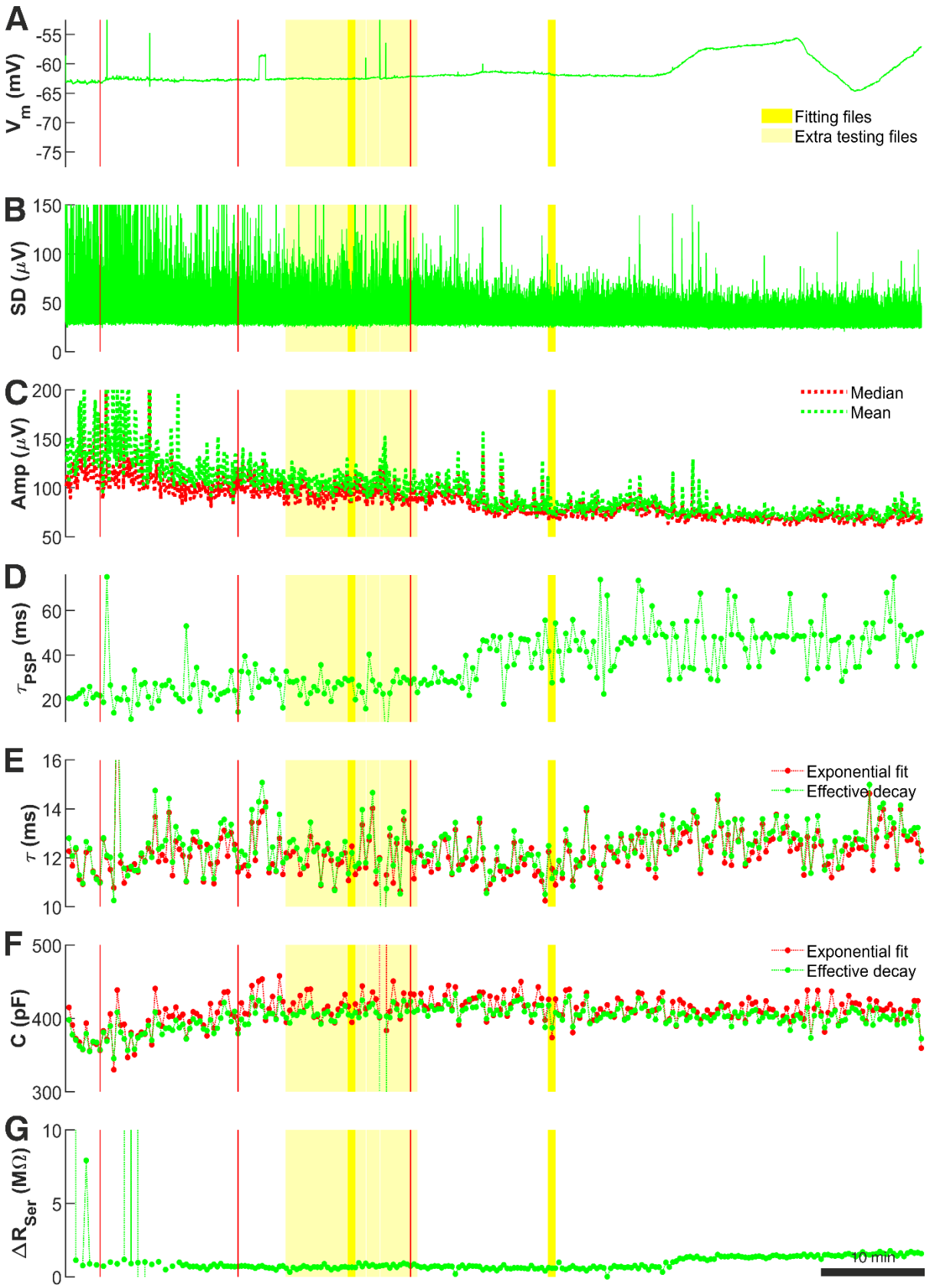

Supplementary Figure 1: Cell p106b (layer 5). Recording quality measures used to select 'noise with minis' and 'noise-alone' sweeps.

1089 (A) Baseline V_m across entire recording (excluding stimulation pulse periods); duration 4960 s. Red

1090 lines and shaded yellow regions and Panels B-G as for Figure 2.

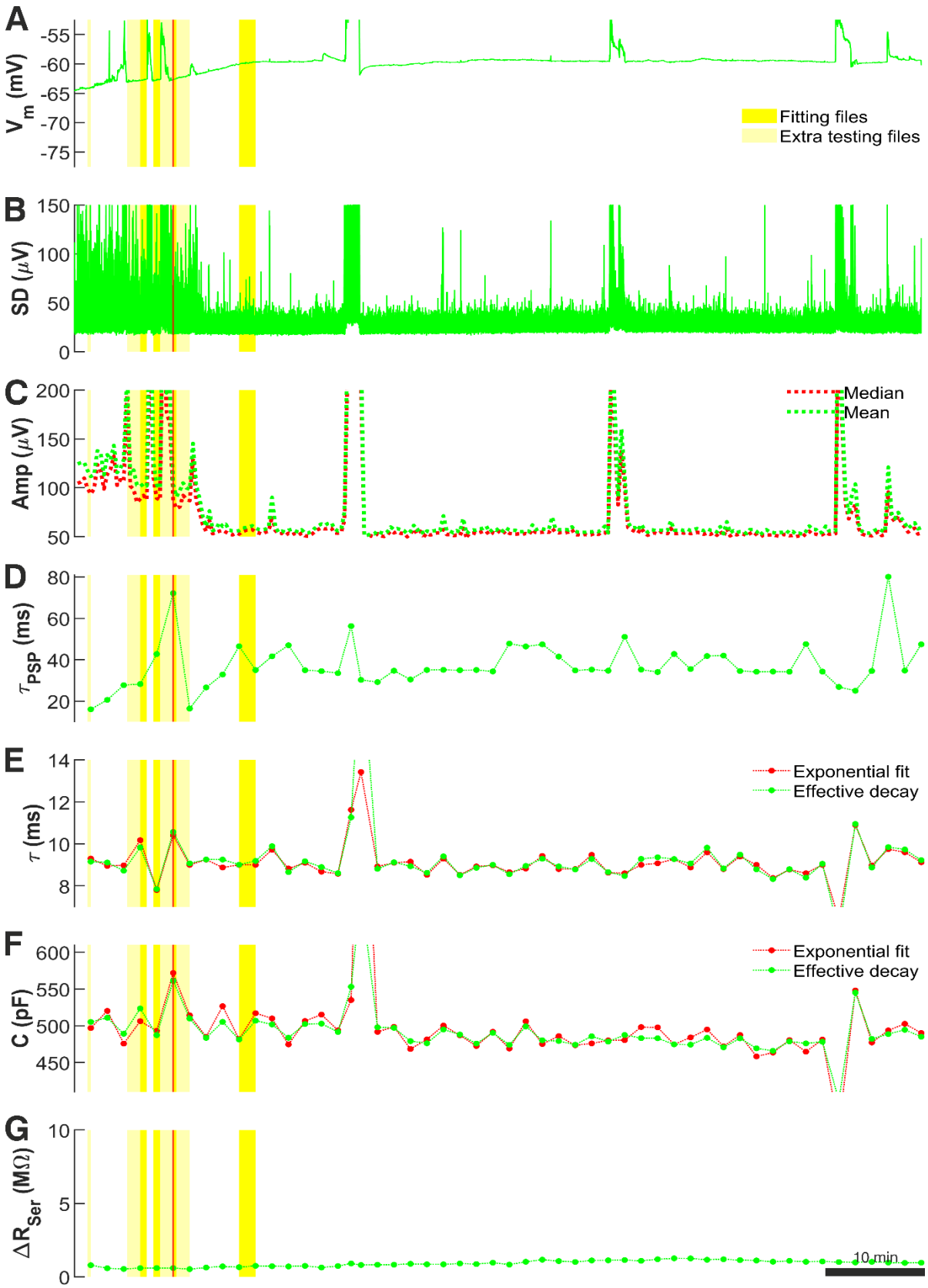

Supplementary Figure 2: Cell p108a (layer 5). Recording quality measures used to select 'noise with minis' and 'noise-alone' sweeps.

1094 Panels A-G as for Figure 1 except for data being averaged over 100-second-long windows (5
1095 recording sweeps of 20 s each) in panels D-G. The figure shows only part of the recording following
1096 the blockade of APs with only a single red vertical time marker visible indicating the time when
1097 pharmacological EPSP blockers were infused. The total duration of the recording shown in the figure
1098 was 5140 s. Some episodes with transient recording instabilities (noise glitches) were removed from
1099 the 'noise with minis' epoch (white gaps).
1100

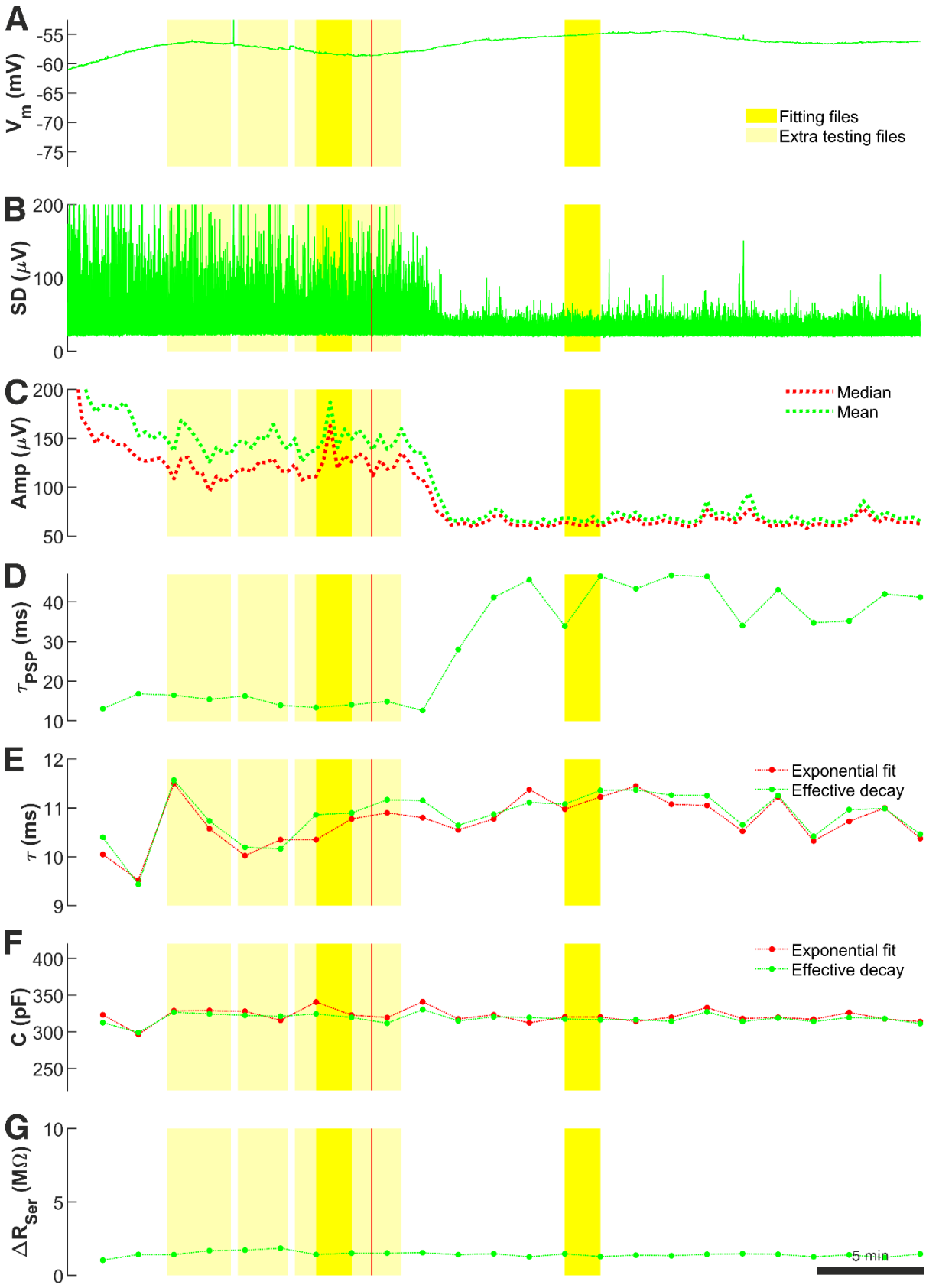

Supplementary Figure 3: Cell p108b (layer 5). Recording quality measures used to select 'noise with minis' and 'noise-alone' sweeps.

1104 Panels A-G as for Figure 2 and Supplementary Figure 2. Data were averaged over 100-second-long

1105 windows (5 recording sweeps of 20 s each) in panels D-G; duration 2400 s.

1106

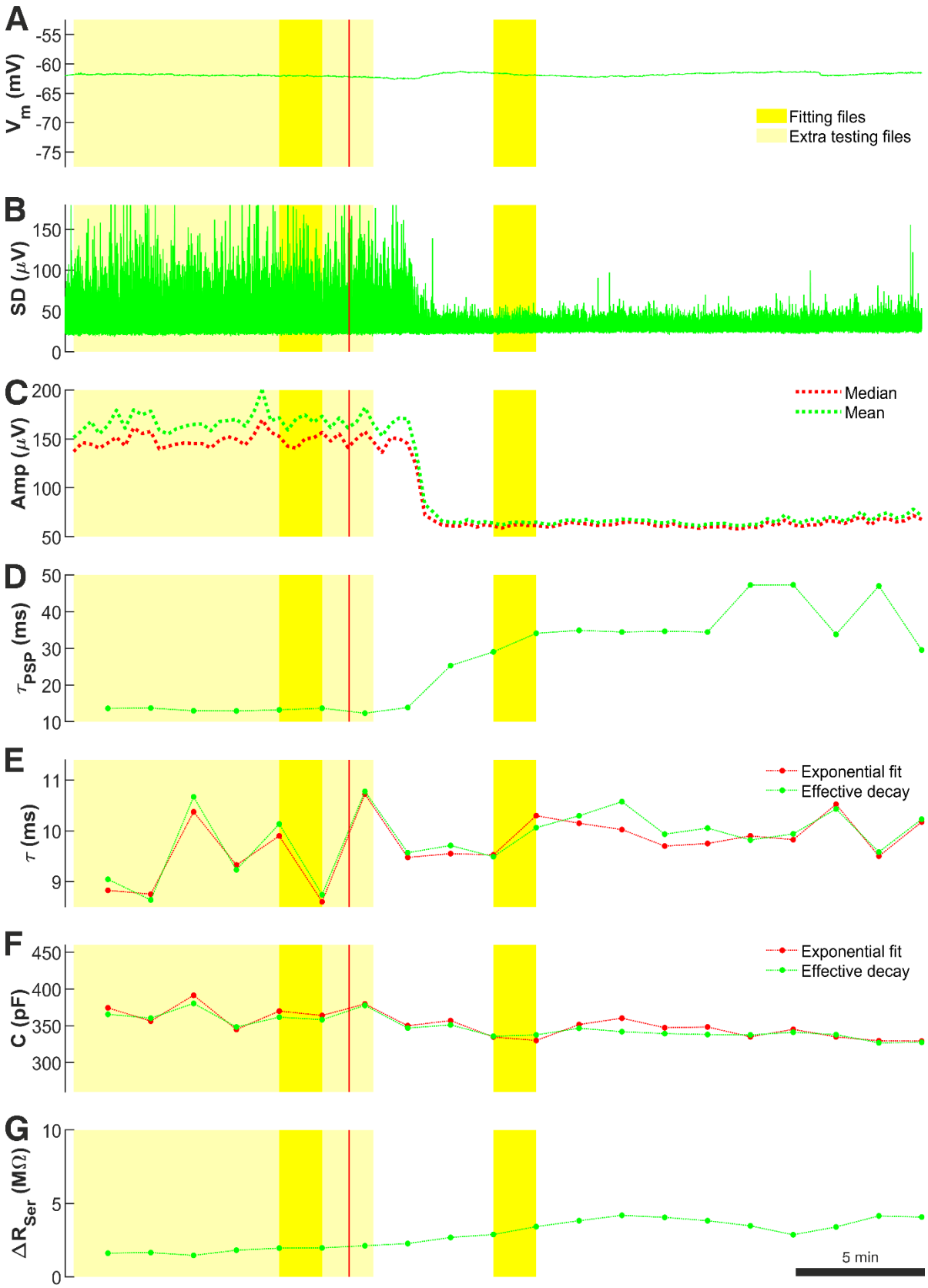

Supplementary Figure 4: Cell p108c (layer 5). Recording quality measures used to select 'noise with minis' and 'noise-alone' sweeps.

1110 Panels A-G as for Figure 2 and Supplementary Figure 2. Data were averaged over 100-second-long

1111 windows (5 recording sweeps of 20 s each) in panels D-G; duration 2000 s.

1112

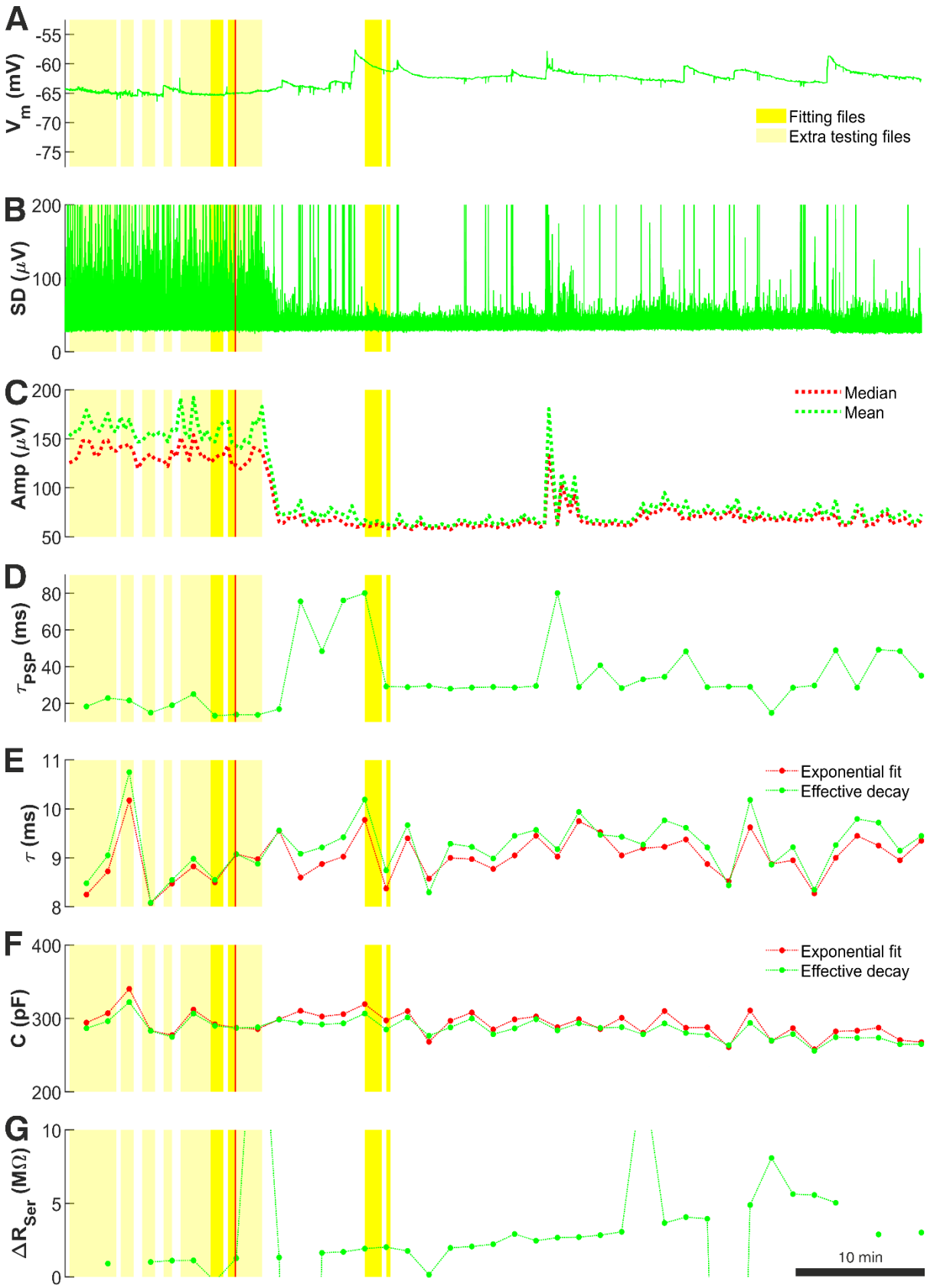

Supplementary Figure 5: Cell p120b (layer 2/3). Recording quality measures used to select 'noise with minis' and 'noise-alone' sweeps.

Panels A-G as for Figure 2 and Supplementary Figure 2. Data were averaged over 100-second-long windows (5 recording sweeps of 20 s each) in panels D-G; duration 4000 s. Some transient ‘glitchy’ extra noisy periods (due to transient recording instability) were manually excluded from the ‘noise with minis’ and ‘noise-alone’ epochs (white gaps).

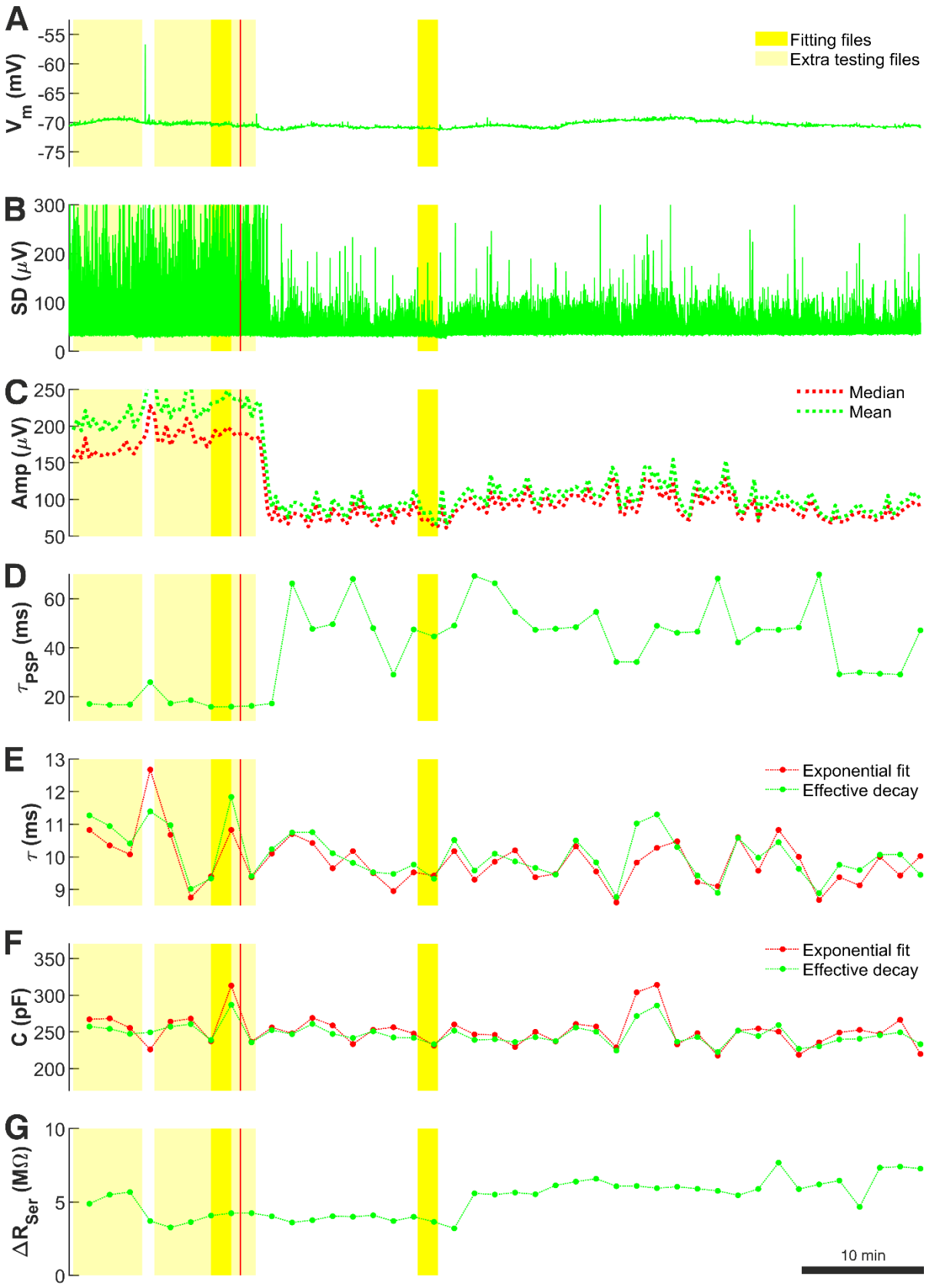

Supplementary Figure 6: Cell p122a (layer 2/3). Recording quality measures used to select 'noise with minis' and 'noise-alone' sweeps.

1124 Panels A-G as for Figure 2 and Supplementary Figure 2. Data were averaged over 100-second-long

1125 windows (5 recording sweeps of 20 s each) in panels D-G; duration 4200 s.

1126

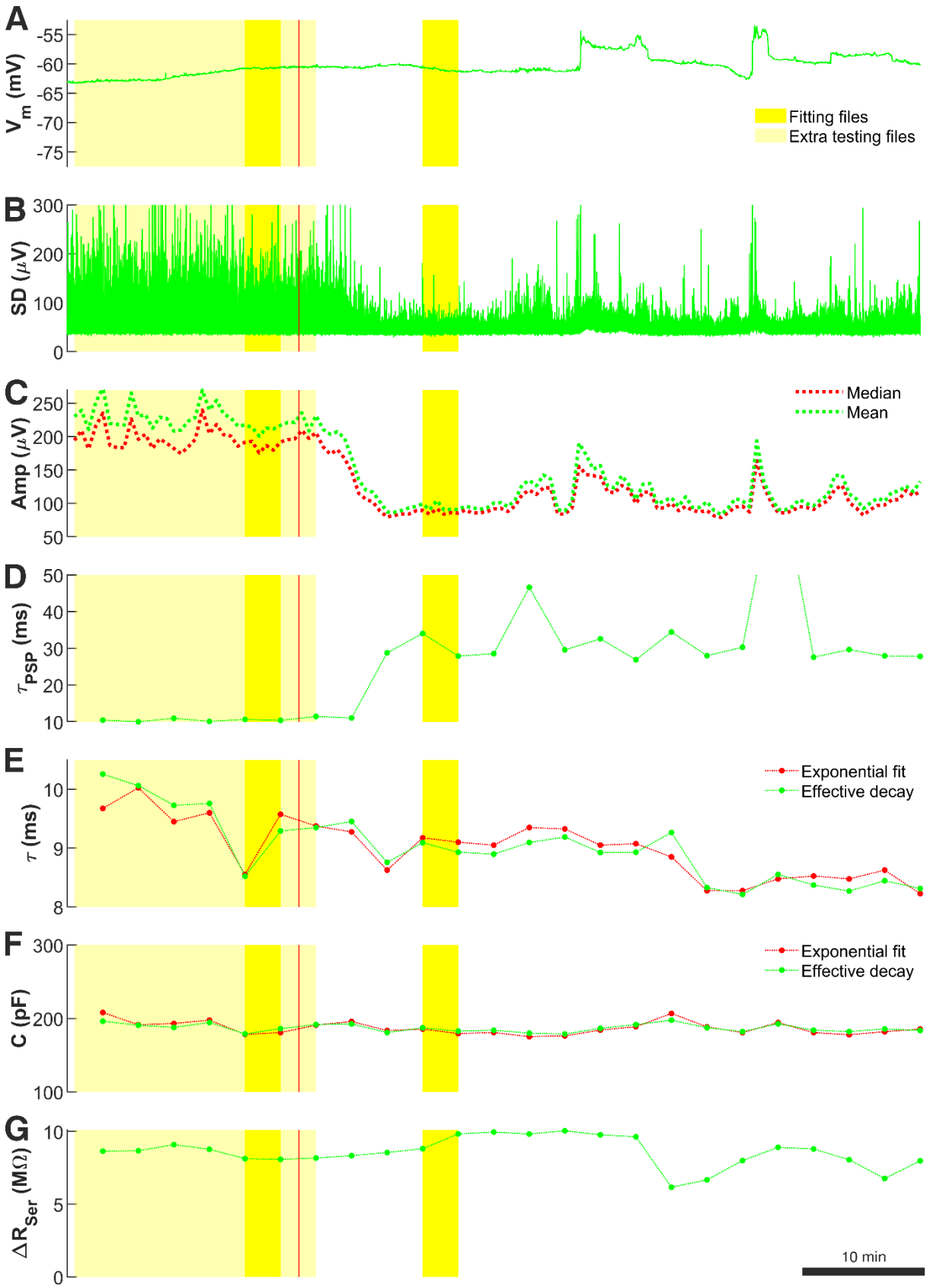

Supplementary Figure 7: Cell p124b (layer 5). Recording quality measures used to select 'noise with minis' and 'noise-alone' sweeps.

1130 Panels A-G as for Figure 2 and Supplementary Figure 2. Data were averaged over 100-second-long

1131 windows (5 recording sweeps of 20 s each) in panels D-G; duration 2400 s.

1132

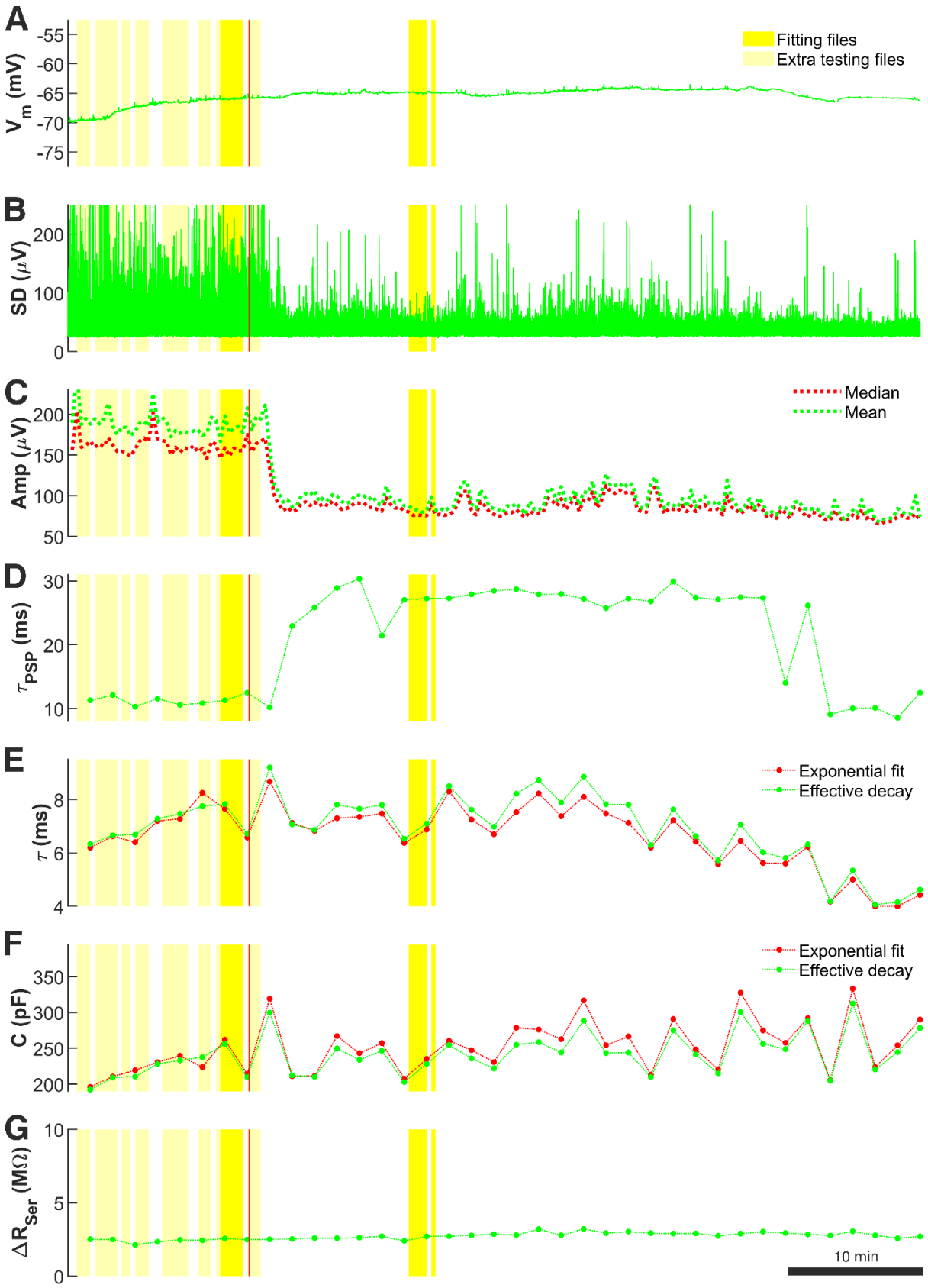

Supplementary Figure 8: Cell p125a (layer 2/3). Recording quality measures used to select 'noise with minis' and 'noise-alone' sweeps.

1136 Panels A-G as for Figure 2 and Supplementary Figure 2. Data were averaged over 100-second-long

1137 windows (5 recording sweeps of 20 s each) in panels D-G; duration 3800 s. Some transiently extra

1138 noisy data due to temporary recording instability were excluded from the ‘noise-alone’ epoch.

1139

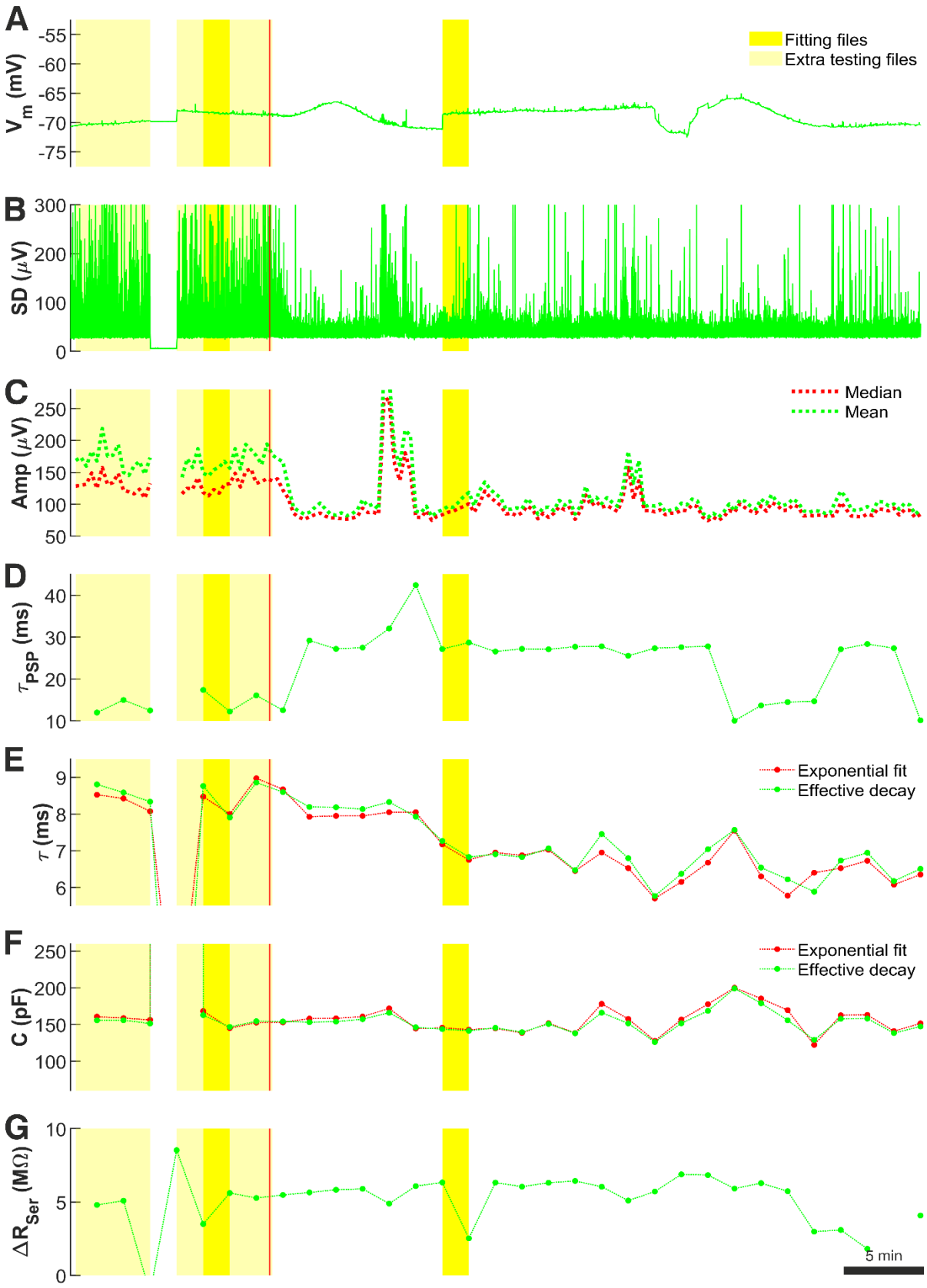

Supplementary Figure 9: Cell p127c (layer 2/3). Recording quality measures used to select 'noise with minis' and 'noise-alone' sweeps.

1143 Panels A-G as for Figure 2 and Supplementary Figure 2. Data were averaged over 100-second-long

1144 windows (5 recording sweeps of 20 s each) in panels D-G; duration 3200 s.

1145

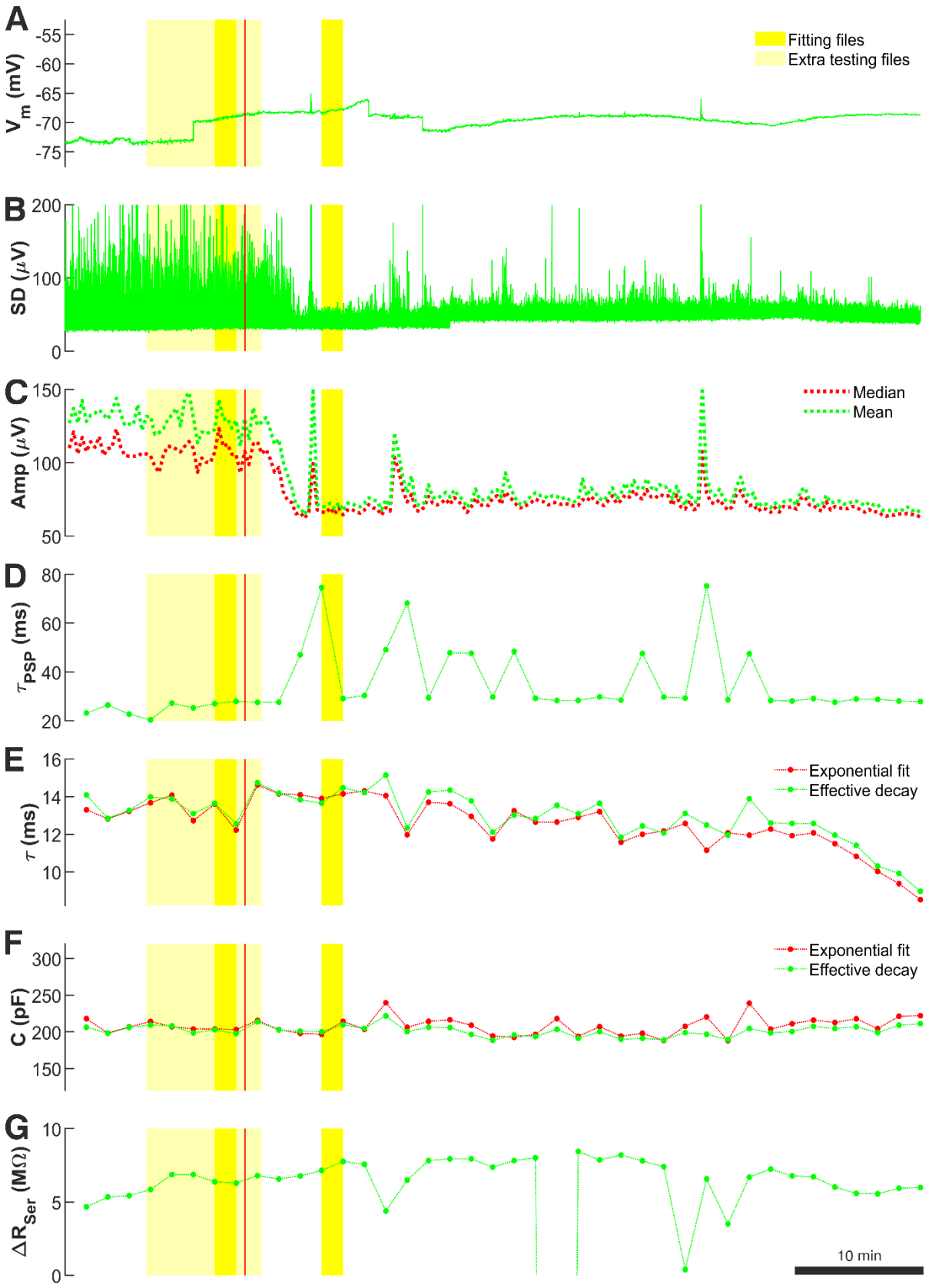

Supplementary Figure 11: Cell p129a (layer 5). Recording quality measures used to select 'noise with minis' and 'noise-alone' sweeps.

1149 Panels A-G as for Figure 2 and Supplementary Figure 2. Data were averaged over 100-second-long

1150 windows (5 recording sweeps of 20 s each) in panels D-G; duration 4000 s.

1151

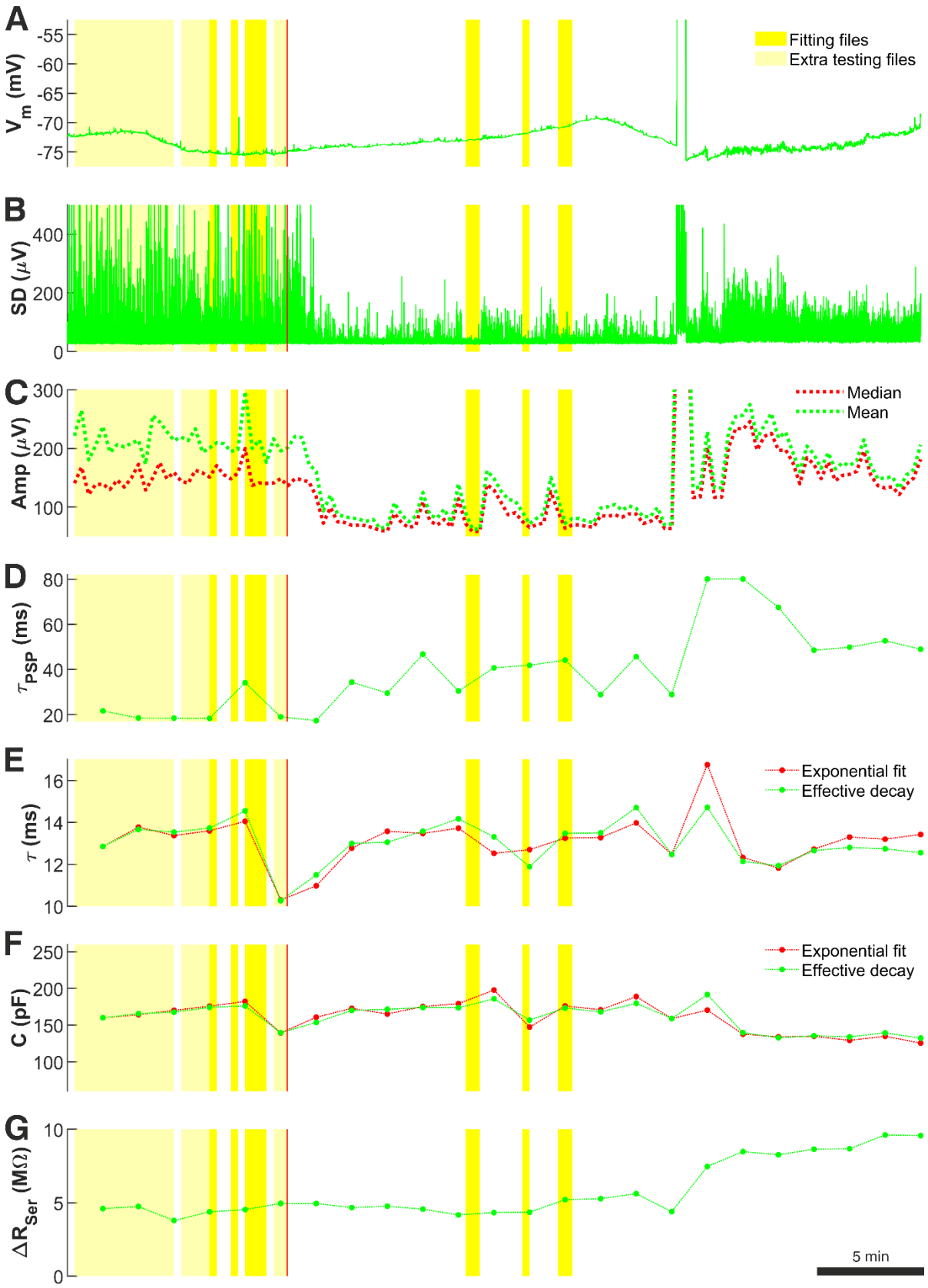

Supplementary Figure 12: Cell p131a (layer 2/3). Recording quality measures used to select 'noise with minis' and 'noise-alone' sweeps.

1155 Panels A-G as for Figure 2 and Supplementary Figure 2. Data were averaged over 100-second-long

1156 windows (5 recording sweeps of 20 s each) in panels D-G; duration 2400 s. Fit epoch is fragmented

1157 due to noisy segments, with transient recording instability, being excluded.

1158

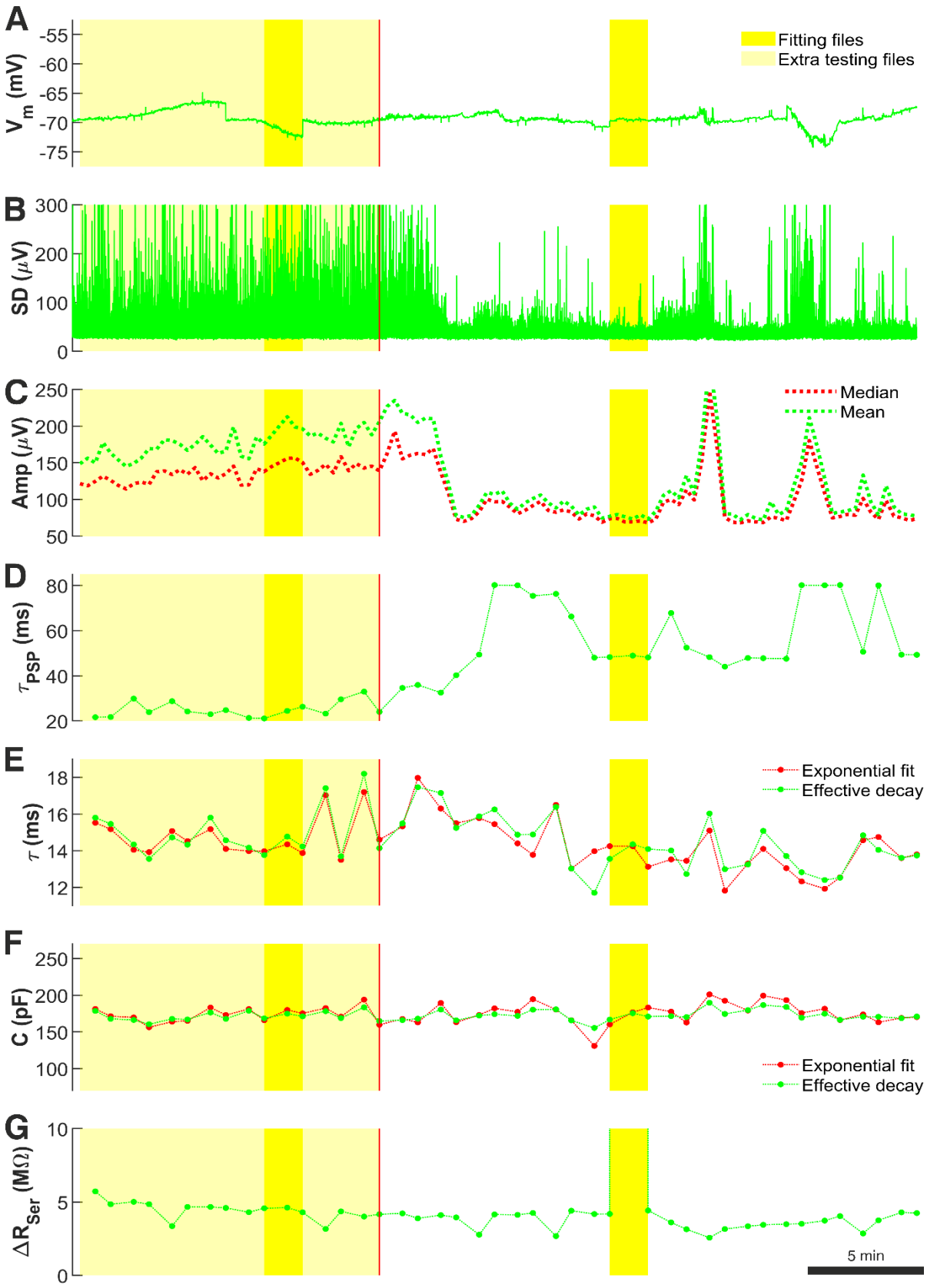

Supplementary Figure 13: Cell p131c (layer 2/3). Recording quality measures used to select 'noise with minis' and 'noise-alone' sweeps.

1162 Panels A-G as for Figure 2 and Supplementary Figure 2. Data were averaged over 100-second-long

1163 windows (5 recording sweeps of 20 s each) in panels D-G; duration 2200 s.

1164

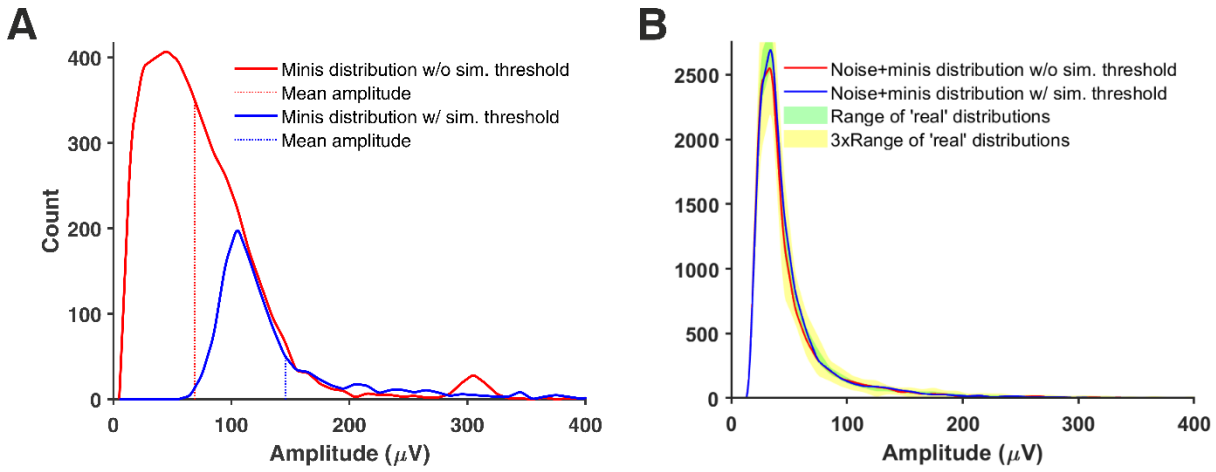

Supplementary figure 14: Non-uniqueness of simulated minis distributions.

(A) Two amplitude distributions of simulated minis events generated by the GA using a lower limit on simulated amplitudes of 10 µV (red histogram; termed as without simulation threshold) or 60 µV simulation threshold (blue histogram).

(B) Distributions of mini-like events detected in a ’noise with simulated minis’ voltage traces corresponding to the two minis source distributions in (A). Event histograms are shown superimposed on the full range of ‘real’ (‘noise with real minis’) distributions. The two distributions clearly fall within the range of ‘real’ distributions albeit being generated by two very different source distributions. Recordings obtained from cell p131c (layer 2/3).

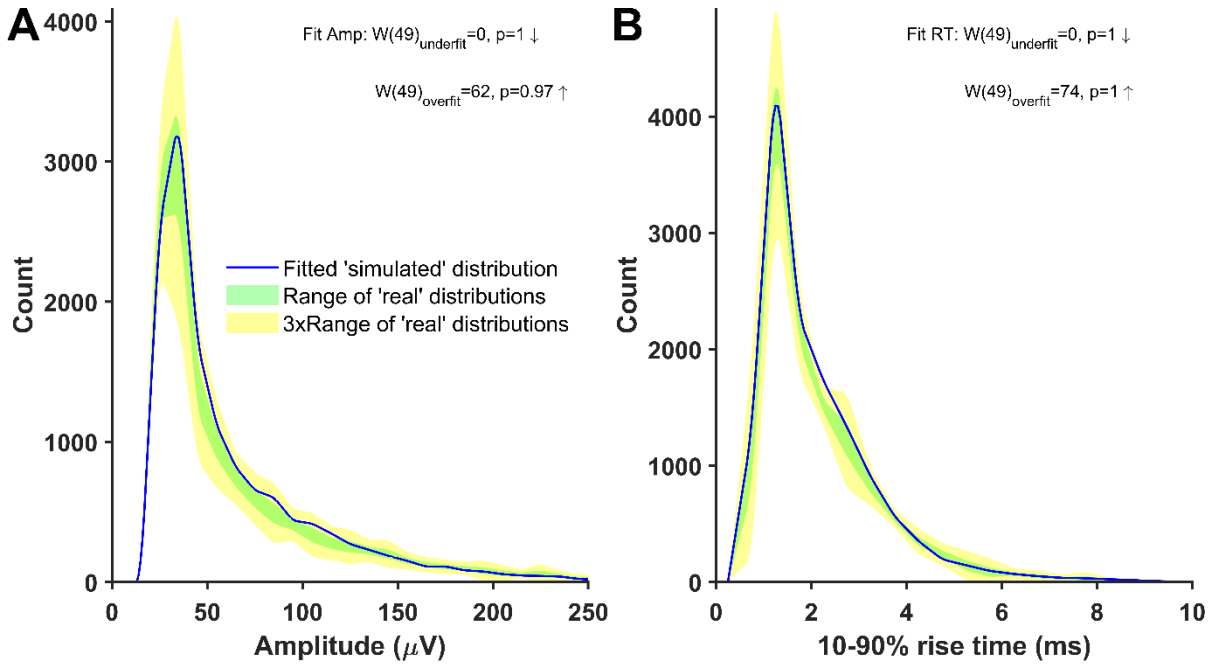

Supplementary figure 15: Distributions of mini-like events detected in a ’noise with simulated minis’ voltage trace that closely matched ‘noise with real minis‘ recordings and passed statistical good fit tests, i.e. did not ‘fail’ the poor fit (underfit) unidirectional tests (it could not be ‘picked out’ either objectively or ‘double-blind’ from the ‘noise with real minis’ distributions found with the same detection parameters).

Parameters of simulated minis were controlled by the GA; ’noise-alone’ recording obtained from cell p103a (layer 5). Downward arrows indicate ‘simulated’ SAD < ‘real’ SAD. Upward arrows indicate ‘simulated’ SAD > ‘real’ SAD. The ‘underfit’ (poor fit) unidirectional test (top) involves a comparison with the ‘worst-performing’ (highest between-file) ‘real’ SAD file (most discrepant from the others; the null hypothesis is ‘simulated’ SAD does not exceed ‘real’ SAD). The ‘overfit’ unidirectional test (bottom) involves a comparison with the ‘best-performing’ (lowest between-file) ‘real’ SAD (least discrepant from the others; the null hypothesis is ‘simulated’ SAD is not smaller than ‘real’ SAD), but ‘failure’ of this test ($p < 0.05$ Bonferroni-corrected, difference not by chance) does not indicate a fit rejection.

(A) Amplitude and (B) 10-90% rise time distributions of mini-like events detected in a ’noise with simulated minis’ voltage trace (blue curve).

1193

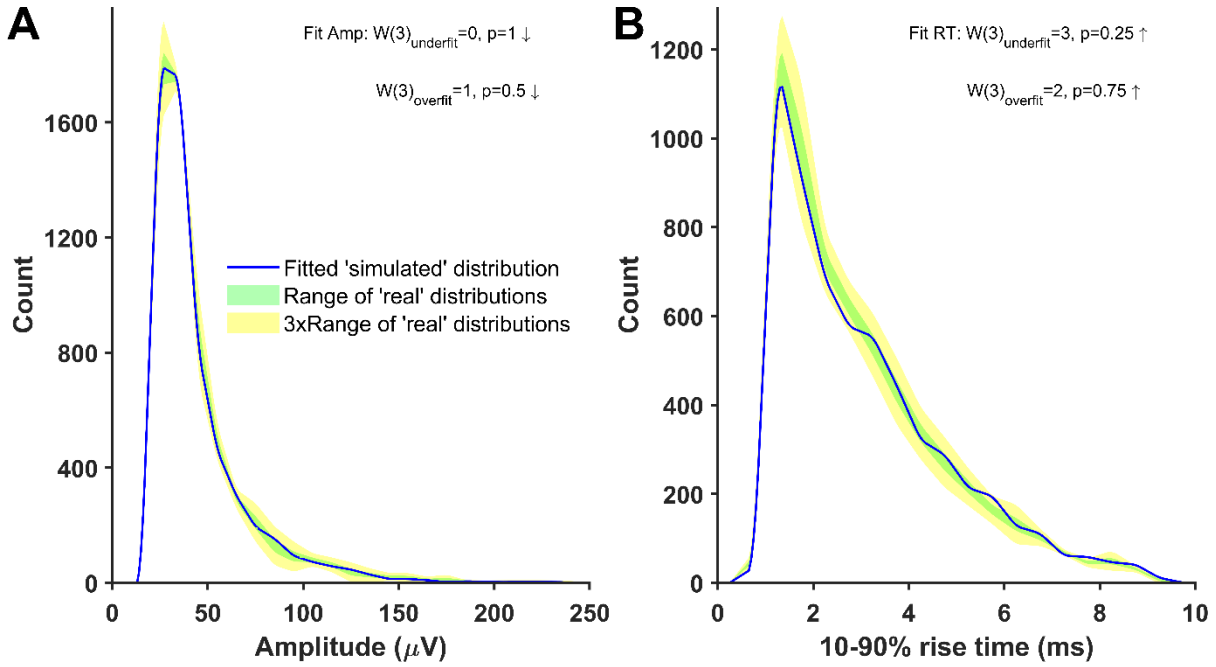

1194

1195 **Supplementary Figure 16:** Cell p108a (layer 5), distributions of mini-like events detected in a ’noise

1196 with simulated minis’ voltage trace that closely matched ‘noise with real minis‘ recordings.

1197 Parameters of simulated minis controlled by GA. Down arrow: ‘simulated’ SAD < ‘real’ SAD (up:

1198 ‘simulated’ > ‘real’; Suppl. Fig. 15).

1199

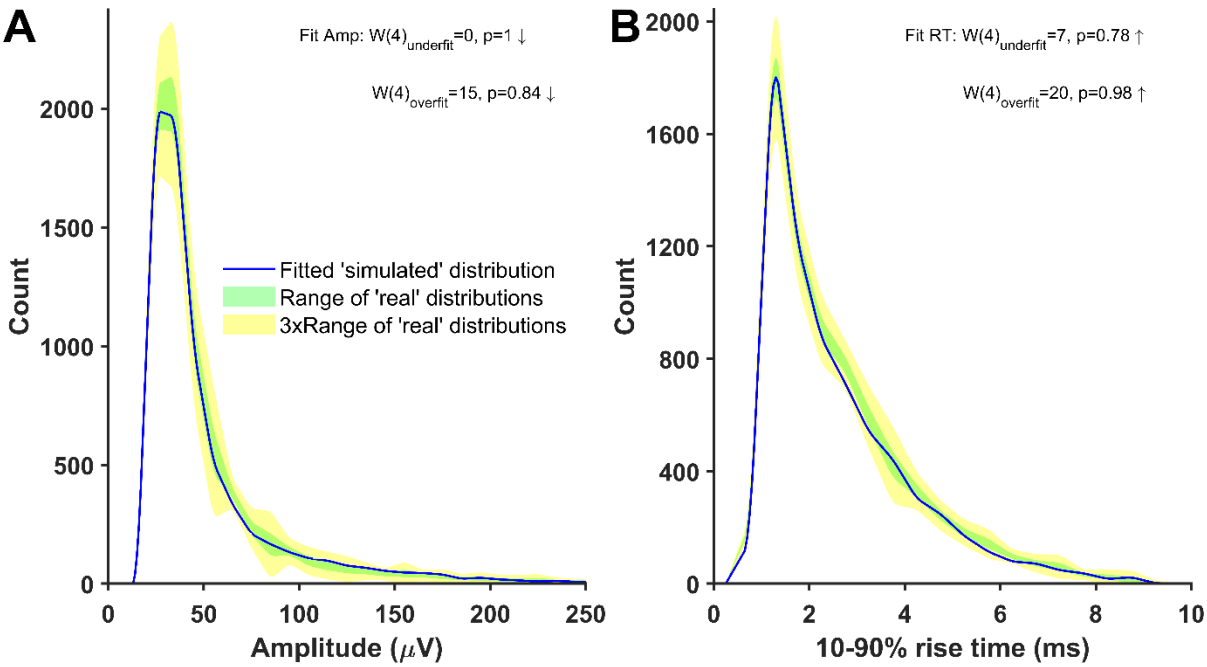

Supplementary Figure 17: Cell p108b (layer 5), distributions of mini-like events detected in a 'noise with simulated minis' voltage trace that closely matched 'noise with real minis' recordings. Parameters of simulated minis controlled by GA. Down arrow: 'simulated' SAD < 'real' SAD (up: 'simulated' > 'real'; Suppl. Fig. 15).

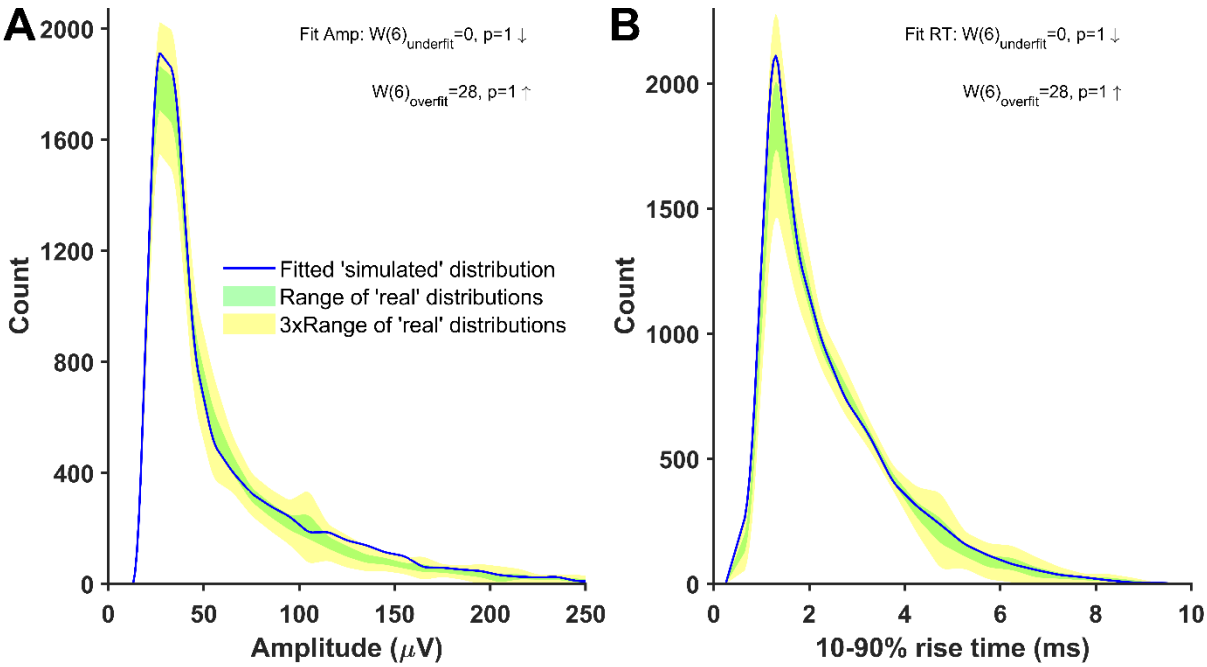

Supplementary Figure 18: Cell p108c (layer 5), distributions of mini-like events detected in a 'noise with simulated minis' voltage trace that closely matched 'noise with real minis' recordings. Parameters of simulated minis controlled by GA. Down arrow: 'simulated' SAD < 'real' SAD (up: 'simulated' > 'real'; Suppl. Fig. 15).

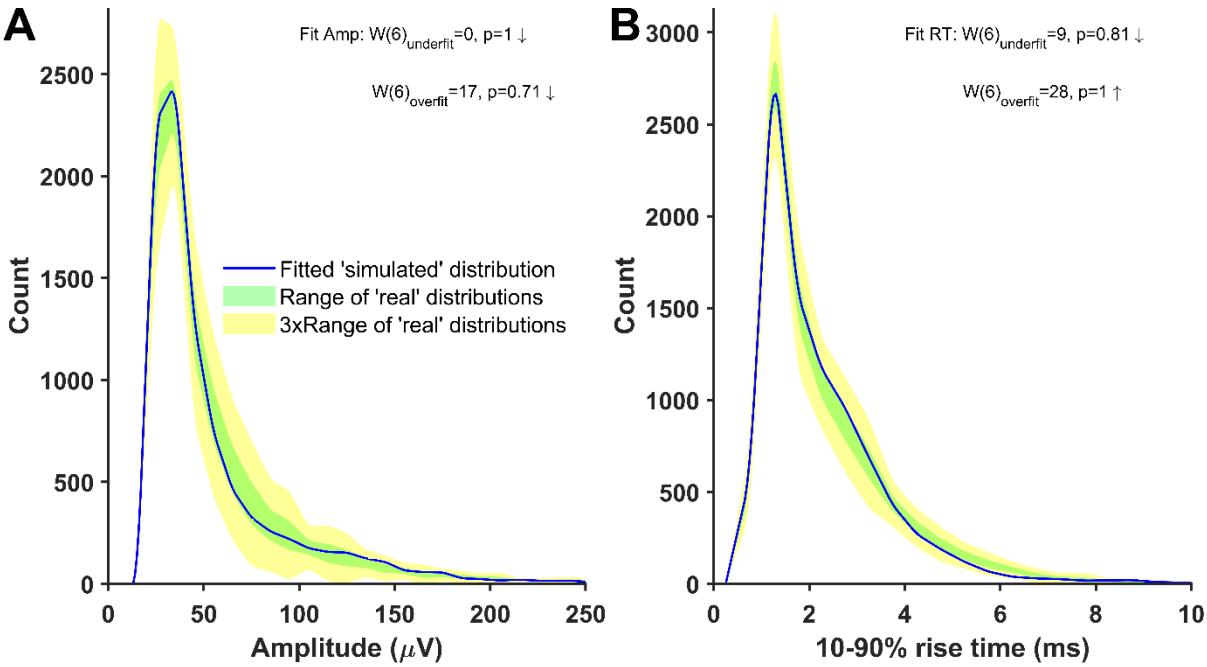

Supplementary Figure 19: Cell p120b (layer 2/3), distributions of mini-like events detected in a 'noise with simulated minis' voltage trace that closely matched 'noise with real minis' recordings. Parameters of simulated minis controlled by GA. Down arrow: 'simulated' SAD < 'real' SAD (up: 'simulated' > 'real'; Suppl. Fig. 15).

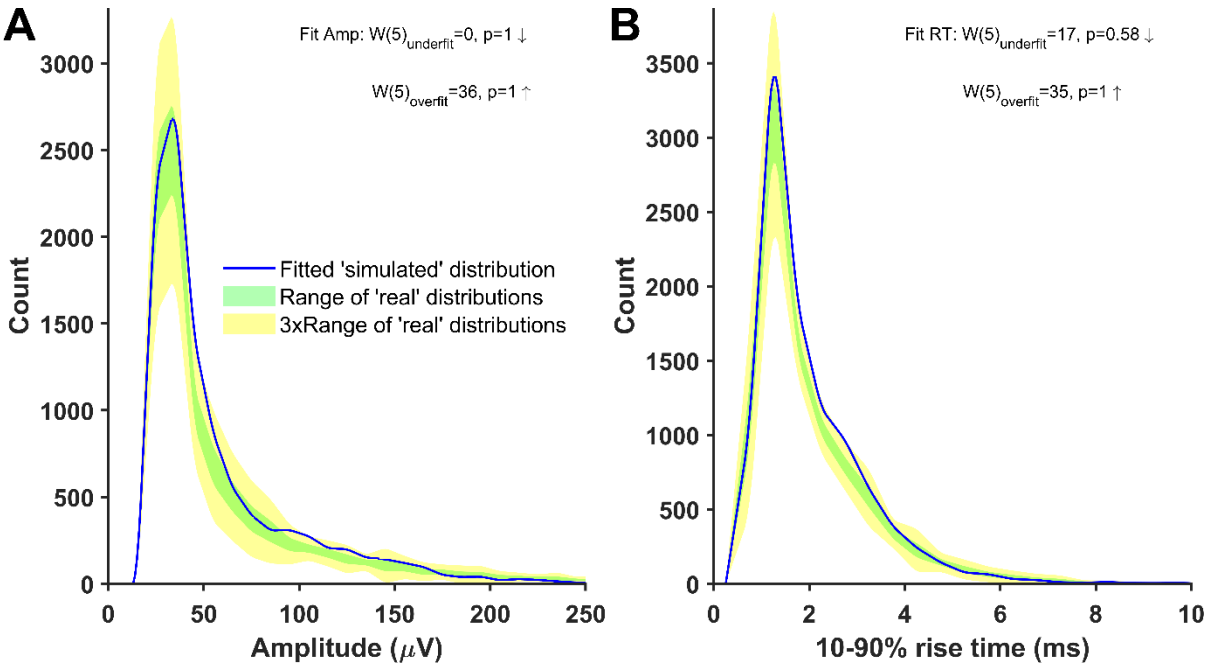

Supplementary Figure 20: Cell p122a (layer 2/3), distributions of mini-like events detected in a 'noise with simulated minis' voltage trace that closely matched 'noise with real minis' recordings. Parameters of simulated minis controlled by GA. Down arrow: 'simulated' SAD < 'real' SAD (up: 'simulated' > 'real'; Suppl. Fig. 15).

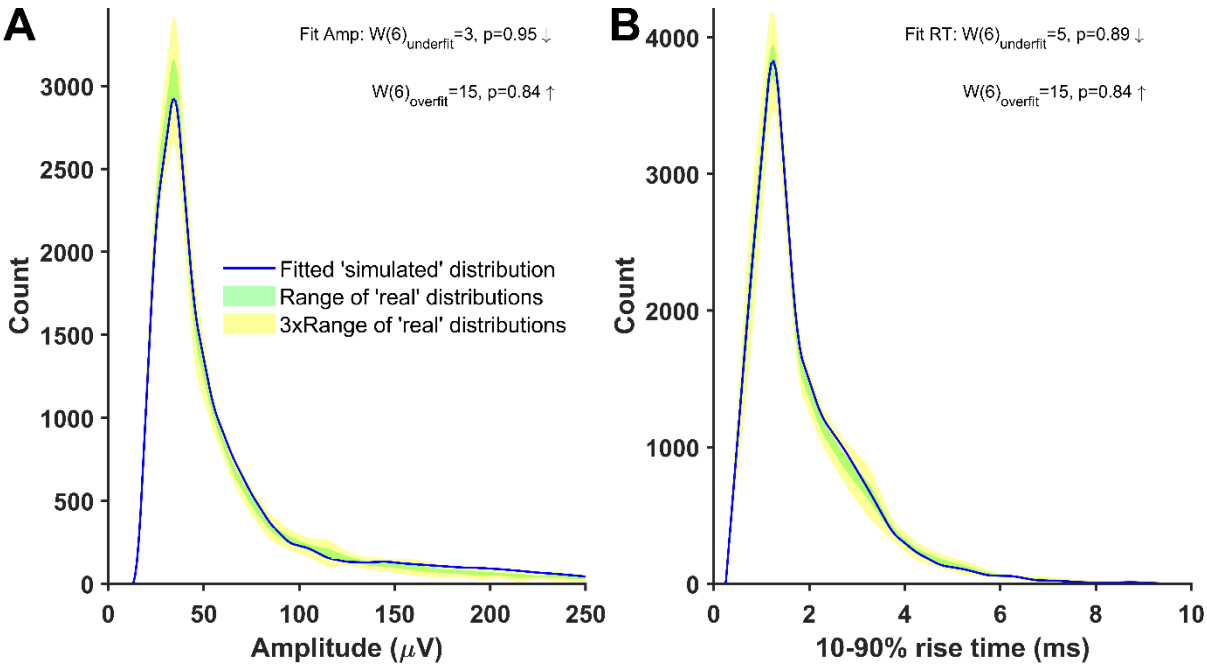

Supplementary Figure 21: Cell p124b (layer 5), distributions of mini-like events detected in a ’noise with simulated minis’ voltage trace that closely matched ‘noise with real minis‘ recordings. Parameters of simulated minis controlled by GA. Down arrow: ‘simulated’ SAD < ‘real’ SAD (up: ‘simulated’ > ‘real’; Suppl. Fig. 15).

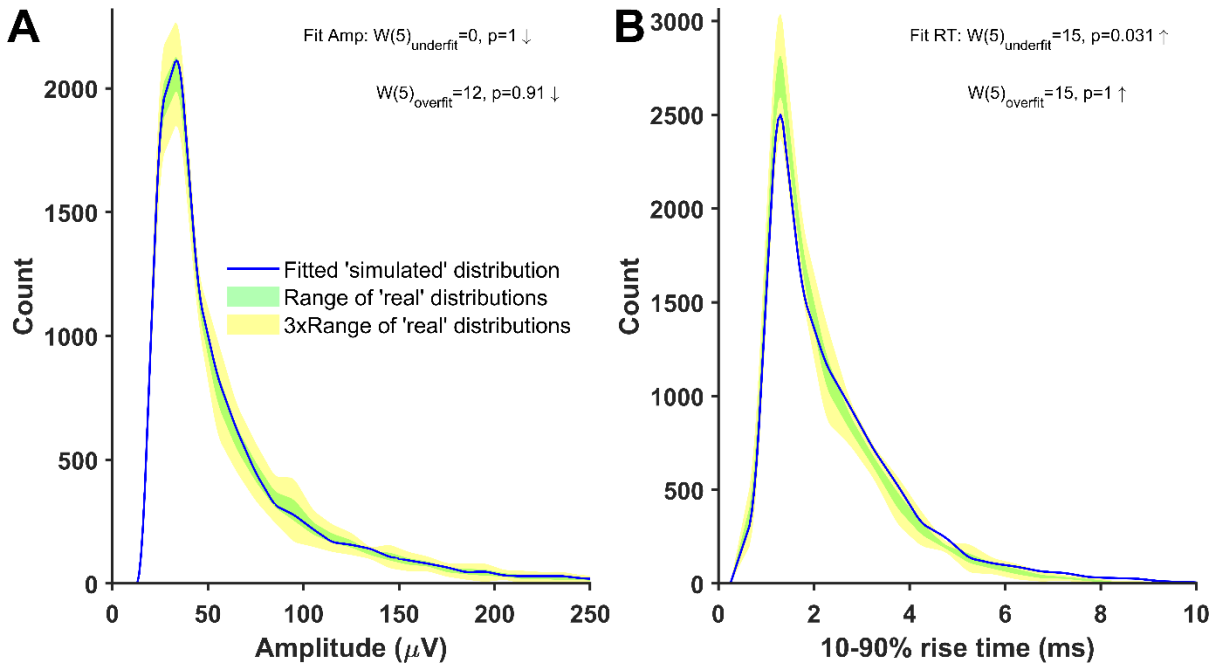

Supplementary Figure 22: Cell p125a (layer 2/3), distributions of mini-like events detected in a 'noise with simulated minis' voltage trace that closely matched 'noise with real minis' recordings. Parameters of simulated minis controlled by GA. Down arrow: 'simulated' SAD < 'real' SAD (up: 'simulated' > 'real'; Suppl. Fig. 15).

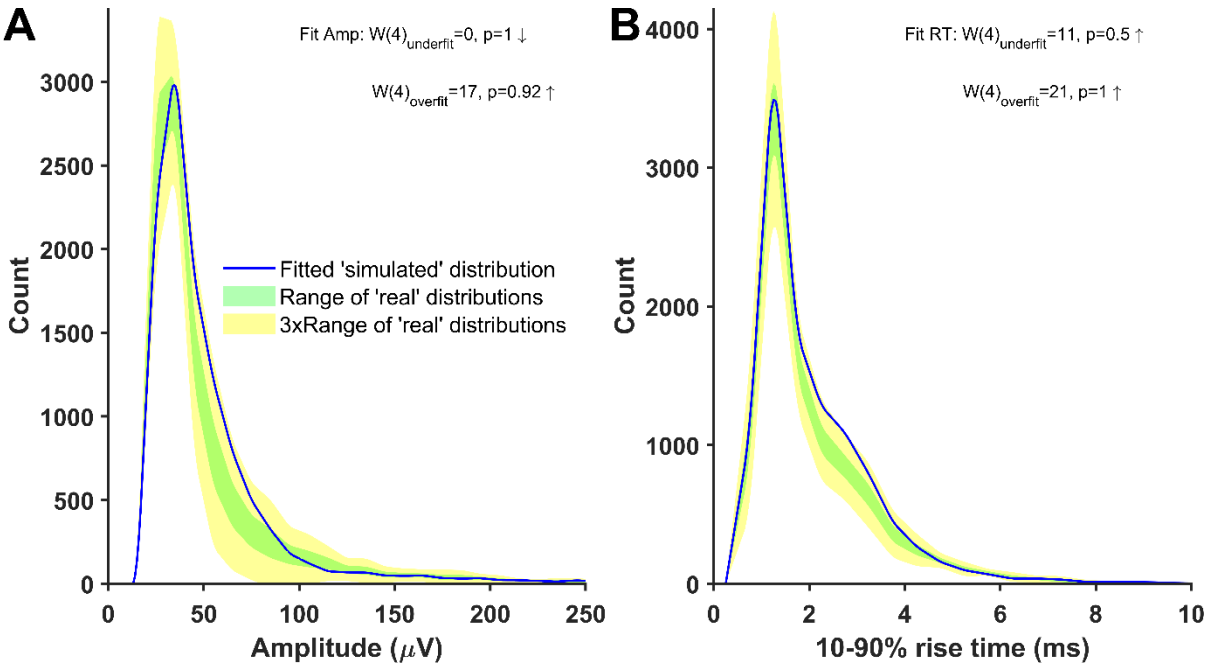

Supplementary Figure 23: Cell p127c (layer 2/3), distributions of mini-like events detected in a 'noise with simulated minis' voltage trace that closely matched 'noise with real minis' recordings. Parameters of simulated minis controlled by GA. Down arrow: 'simulated' SAD < 'real' SAD (up: 'simulated' > 'real'; Suppl. Fig. 15).

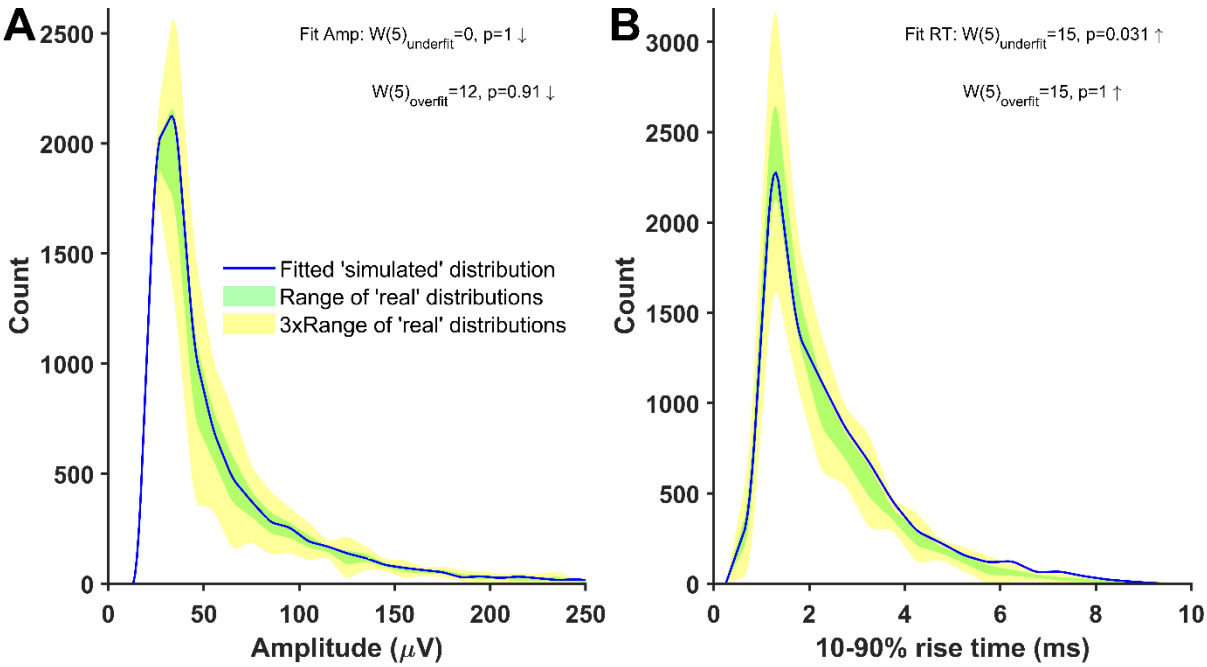

Supplementary Figure 24: Cell p128c (layer 2/3), distributions of mini-like events detected in a 'noise with simulated minis' voltage trace that closely matched 'noise with real minis' recordings. Parameters of simulated minis controlled by GA. Down arrow: 'simulated' SAD < 'real' SAD (up: 'simulated' > 'real'; Suppl. Fig. 15).

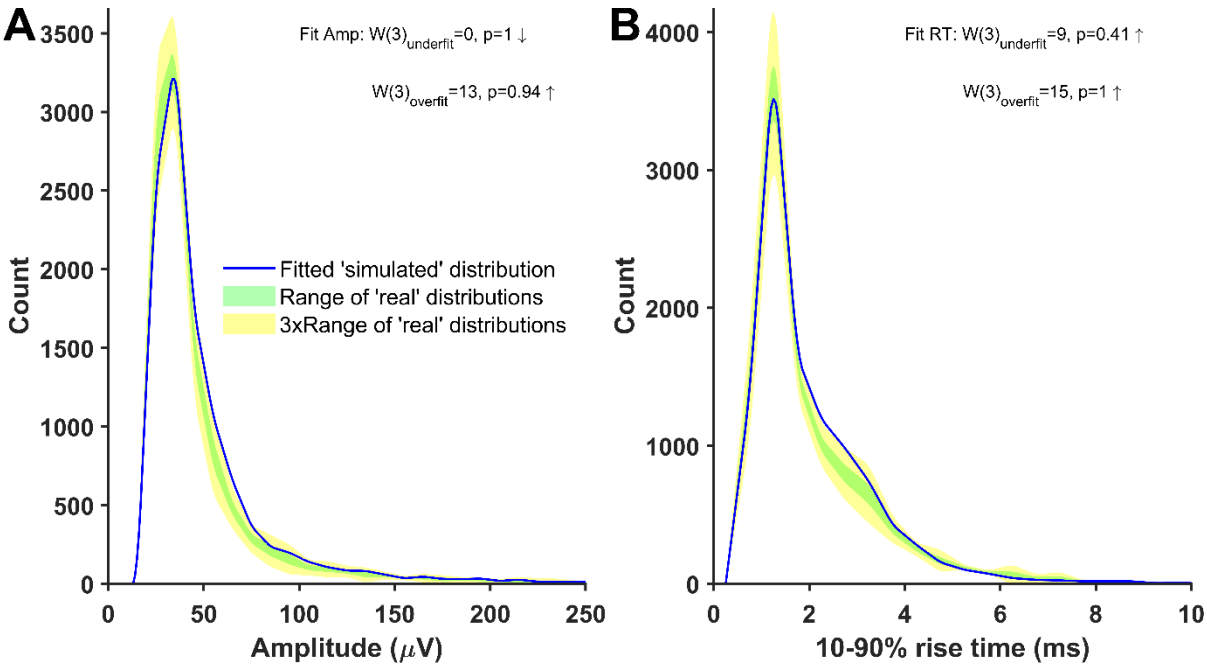

Supplementary Figure 25: Cell p129a (layer 5), distributions of mini-like events detected in a 'noise with simulated minis' voltage trace that closely matched 'noise with real minis' recordings. Parameters of simulated minis controlled by GA. Down arrow: 'simulated' SAD < 'real' SAD (up: 'simulated' > 'real'; Suppl. Fig. 15).

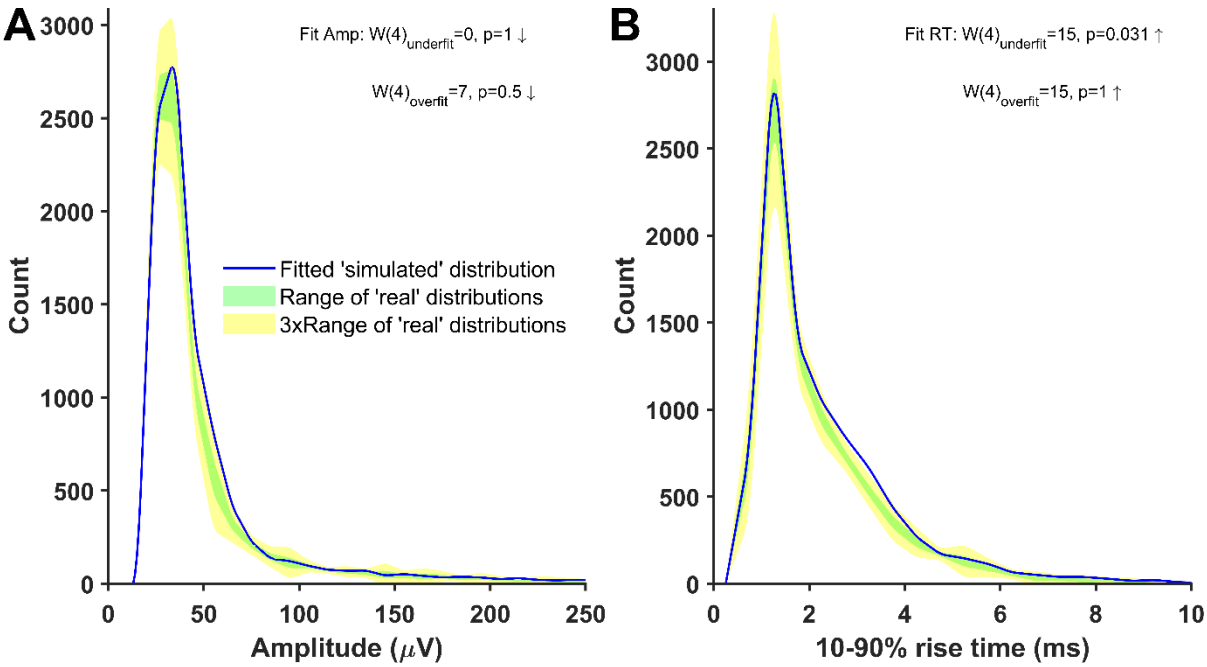

Supplementary Figure 26: Cell p131a (layer 2/3), distributions of mini-like events detected in a 'noise with simulated minis' voltage trace that closely matched 'noise with real minis' recordings. Parameters of simulated minis controlled by GA. Down arrow: 'simulated' SAD < 'real' SAD (up: 'simulated' > 'real'; Suppl. Fig. 15).

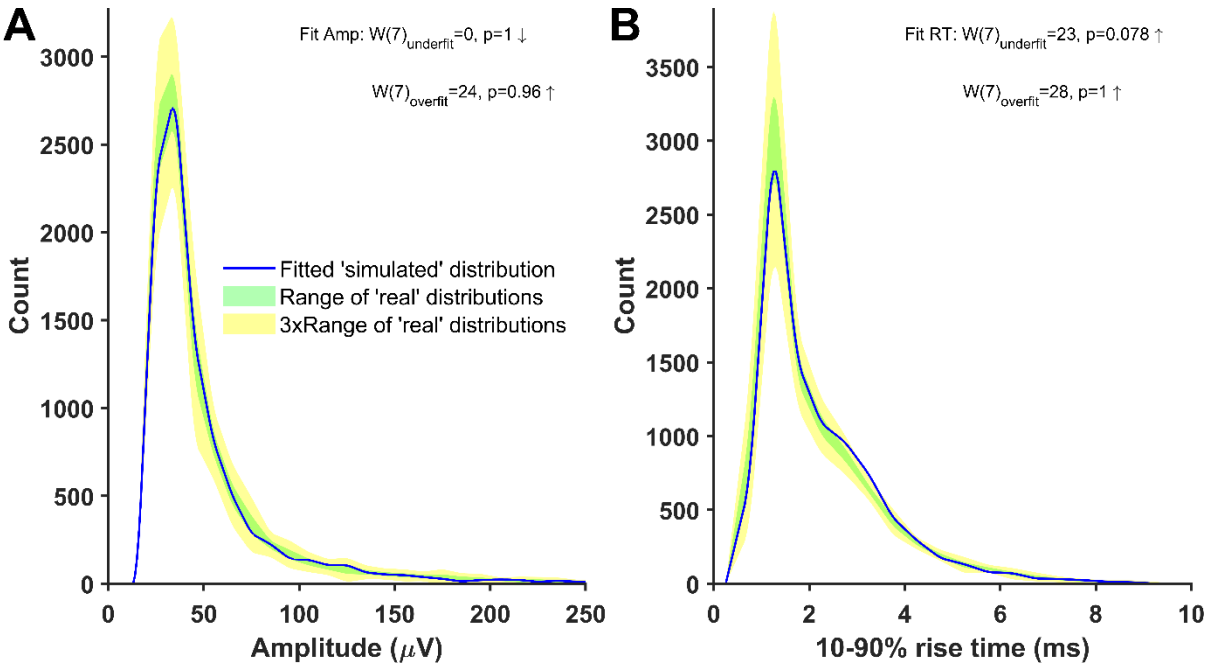

Supplementary Figure 27: Cell p131c (layer 2/3), distributions of mini-like events detected in a 'noise with simulated minis' voltage trace that closely matched 'noise with real minis' recordings. Parameters of simulated minis controlled by GA. Down arrow: 'simulated' SAD < 'real' SAD (up: 'simulated' > 'real'; Suppl. Fig. 15).

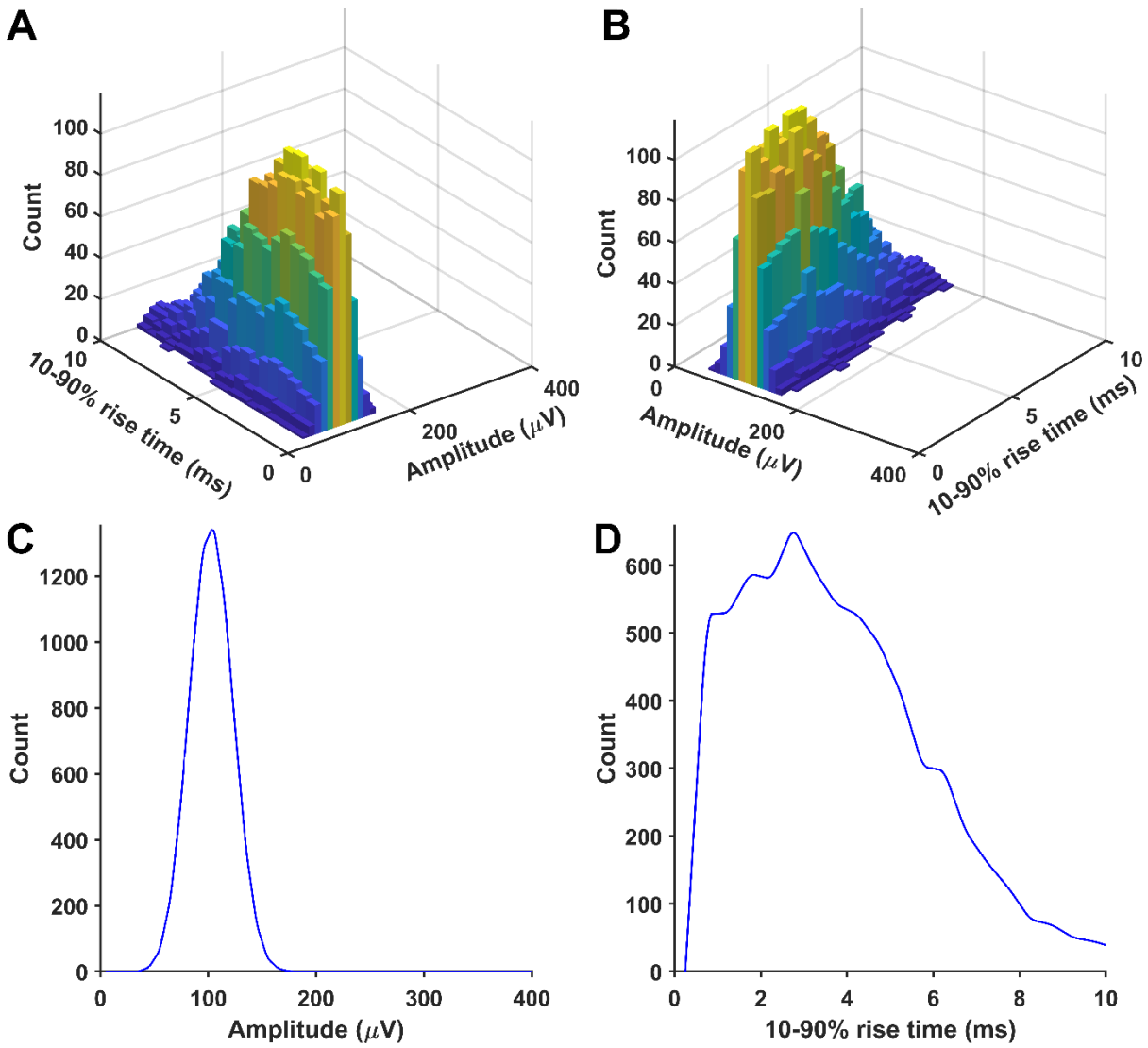

Supplementary Figure 28: An example of a distribution of randomly selected simulated minis that was used to produce a close match between distributions of mini-like events detected in a 'noise with simulated minis' voltage trace (40 µV lower limit on simulated amplitudes) and a 'noise with real minis' recording for cell p103a (layer 5).

(A) and (B) Joint amplitude and 10-90% rise time distribution of simulated minis (two views).

(C) 'Marginal' amplitude and (D) 10-90% rise time distributions (all 2-D bins projected onto that axis).

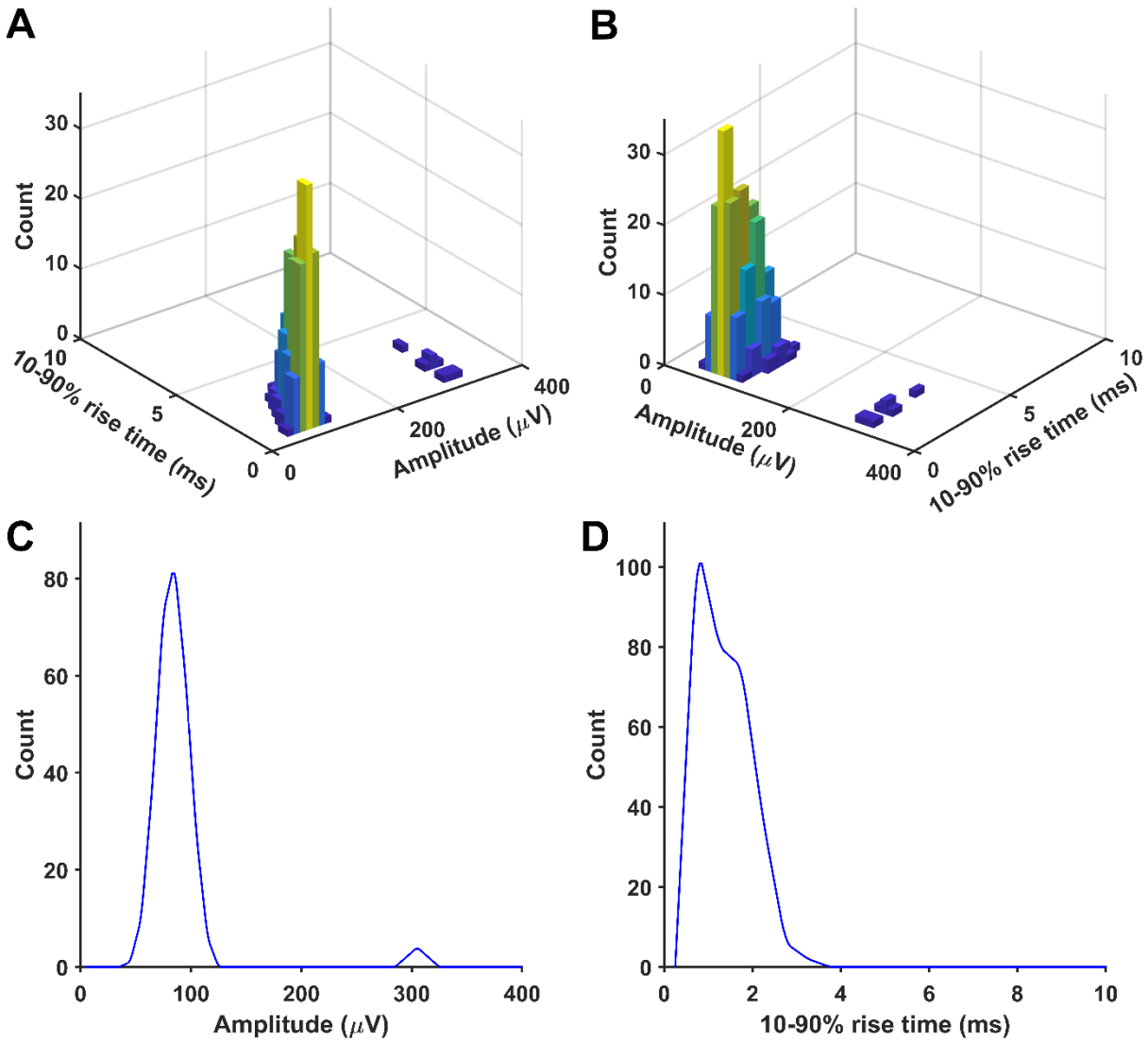

1273

1274 **Supplementary Figure 29:** An example of a distribution of randomly selected simulated minis that

1275 was used to produce a close match between distributions of mini-like events detected in a 'noise

1276 with simulated minis' voltage trace (40 µV lower limit on simulated amplitudes) and a 'noise with

1277 real minis' recording for cell p106b (layer 5).

1278 Panels as for Supplementary Figure 28.

1279

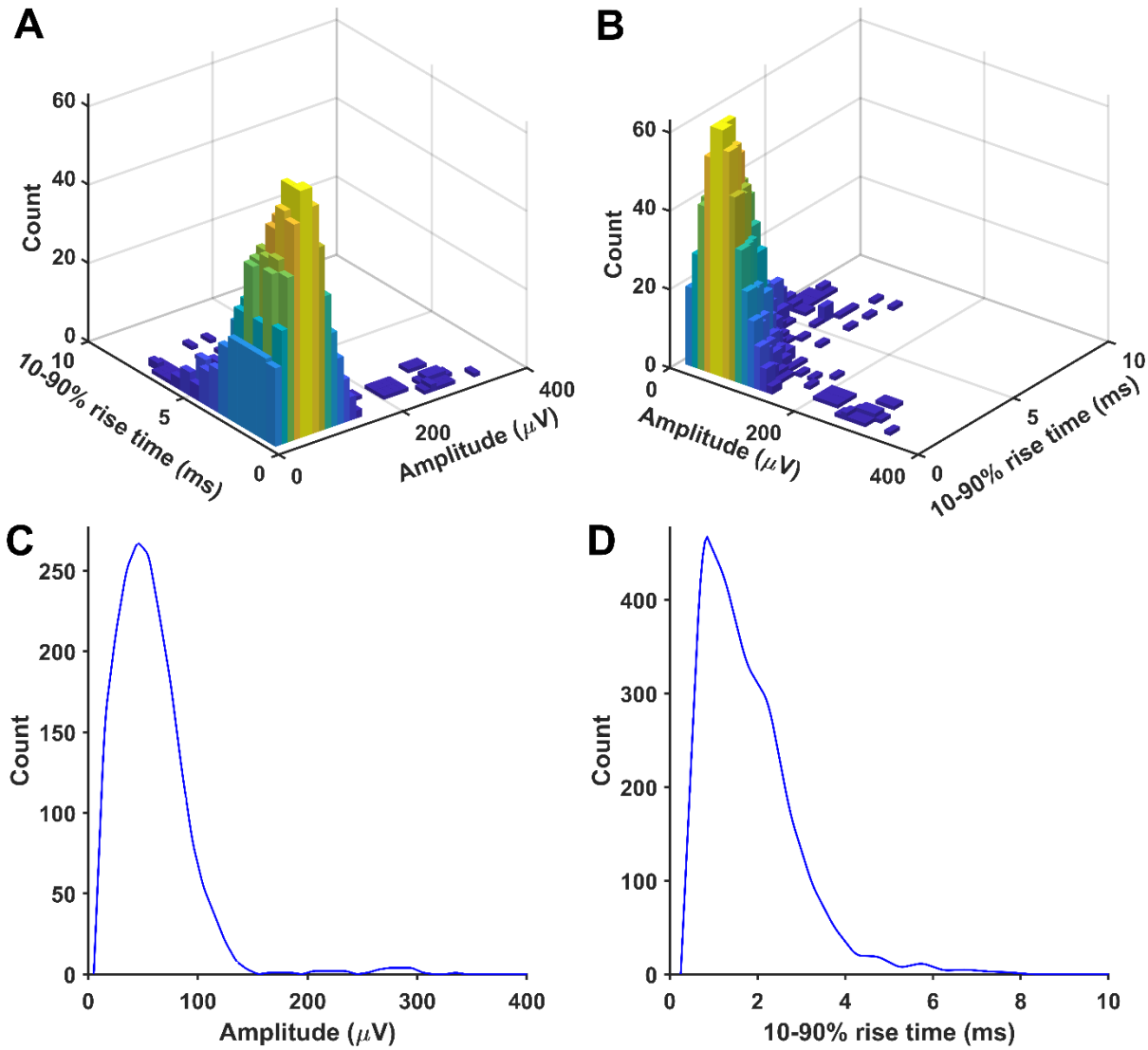

Supplementary Figure 30: An example of a distribution of randomly selected simulated minis that was used to produce a close match between distributions of mini-like events detected in a 'noise with simulated minis' voltage trace (10 µV lower limit on simulated amplitudes) and a 'noise with real minis' recording for cell p108a (layer 5).

Panels as for Supplementary Figure 28.

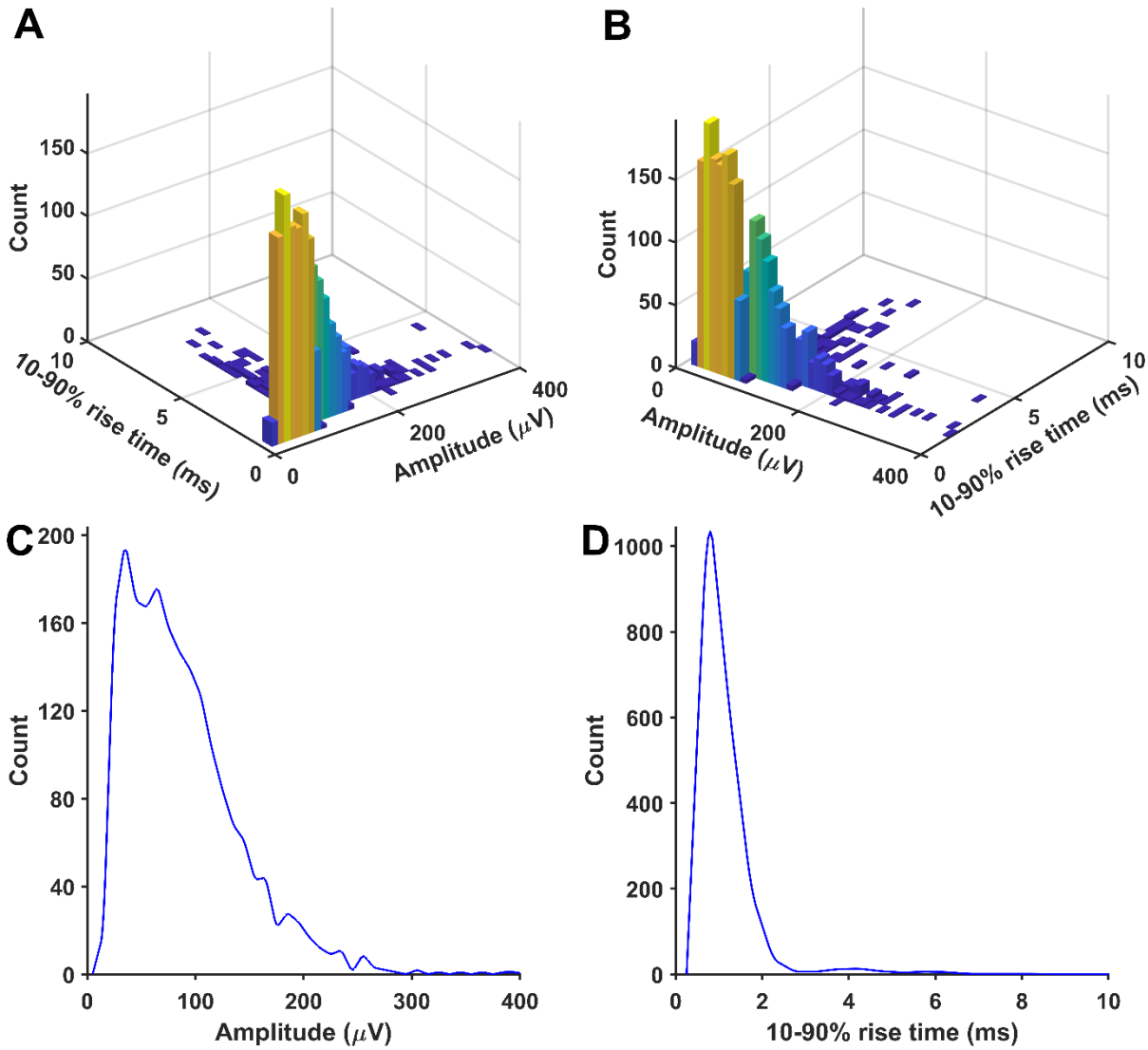

Supplementary Figure 31: An example of a distribution of randomly selected simulated minis that was used to produce a close match between distributions of mini-like events detected in a 'noise with simulated minis' voltage trace (10 µV lower limit on simulated amplitudes) and a 'noise with real minis' recording for cell p108b (layer 5).

Panels as for Supplementary Figure 28.

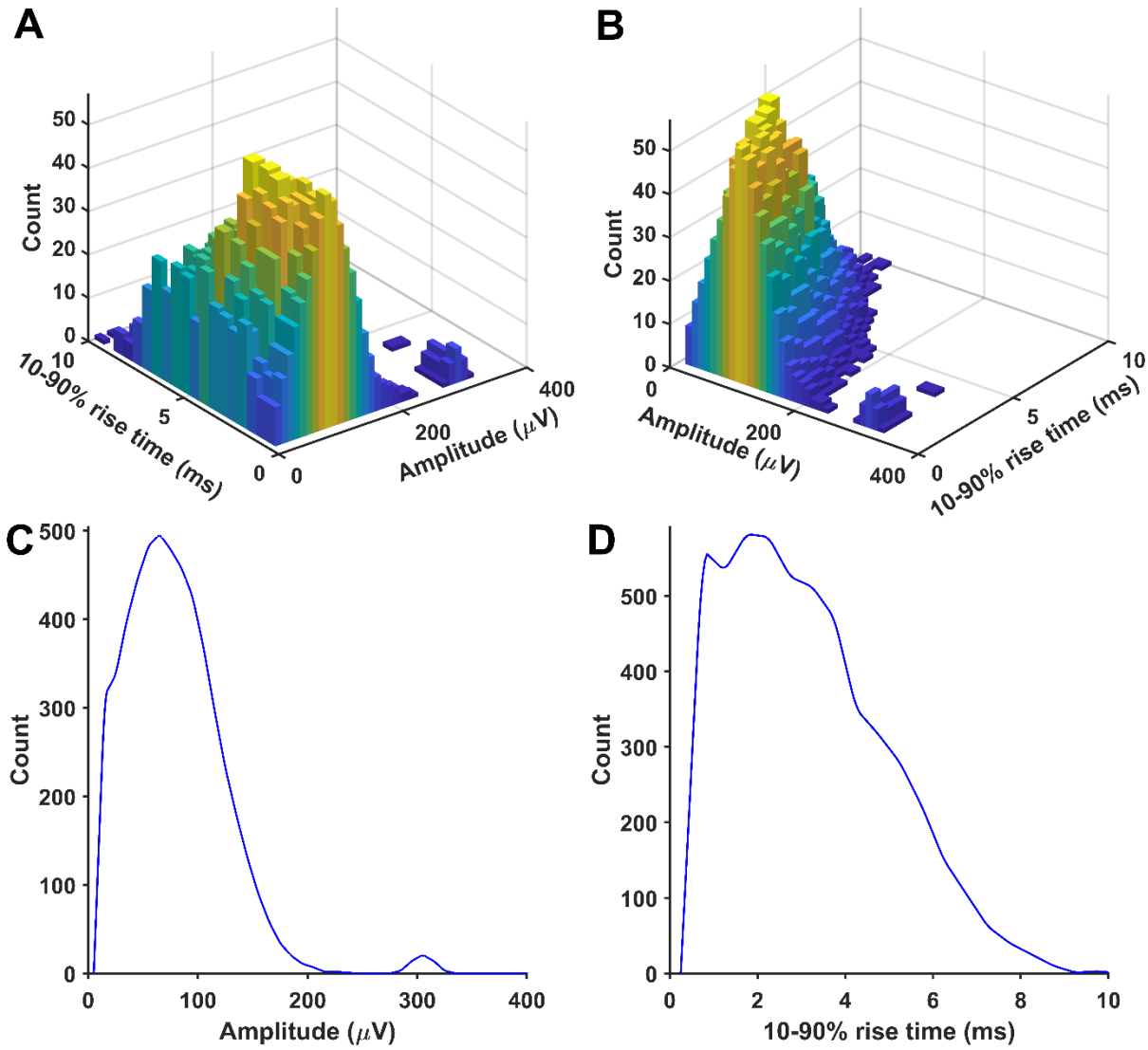

1294

1295 **Supplementary Figure 32:** An example of a distribution of randomly selected simulated minis that

1296 was used to produce a close match between distributions of mini-like events detected in a 'noise

1297 with simulated minis' voltage trace (10 µV lower limit on simulated amplitudes) and a 'noise with

1298 real minis' recording for cell p108c (layer 5).

1299 Panels as for Supplementary Figure 28.

1300

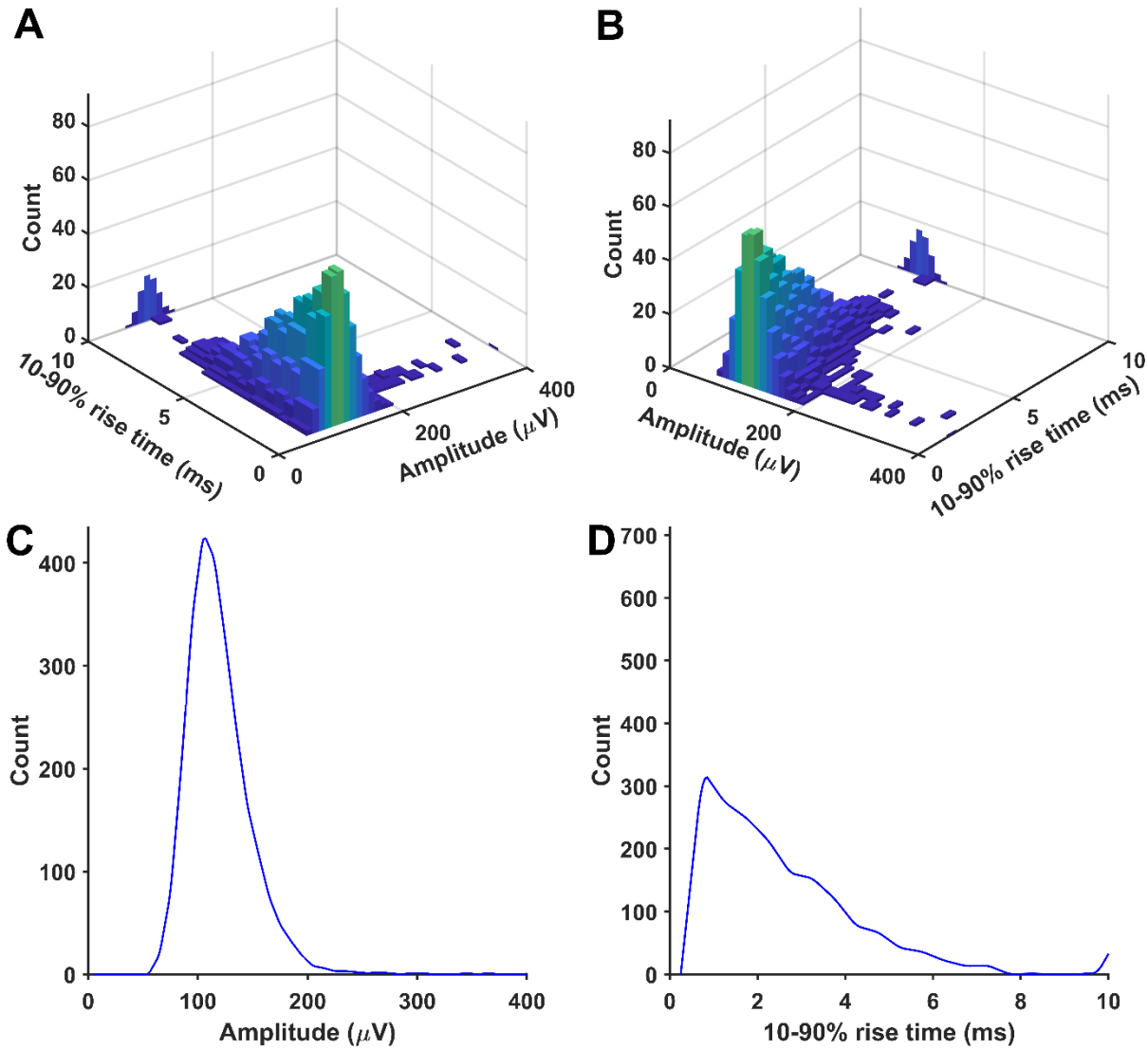

Supplementary Figure 33: An example of a distribution of randomly selected simulated minis that was used to produce a close match between distributions of mini-like events detected in a 'noise with simulated minis' voltage trace (60 µV lower limit on simulated amplitudes) and a 'noise with real minis' recording for cell p120b (layer 2/3).

Panels as for Supplementary Figure 28.

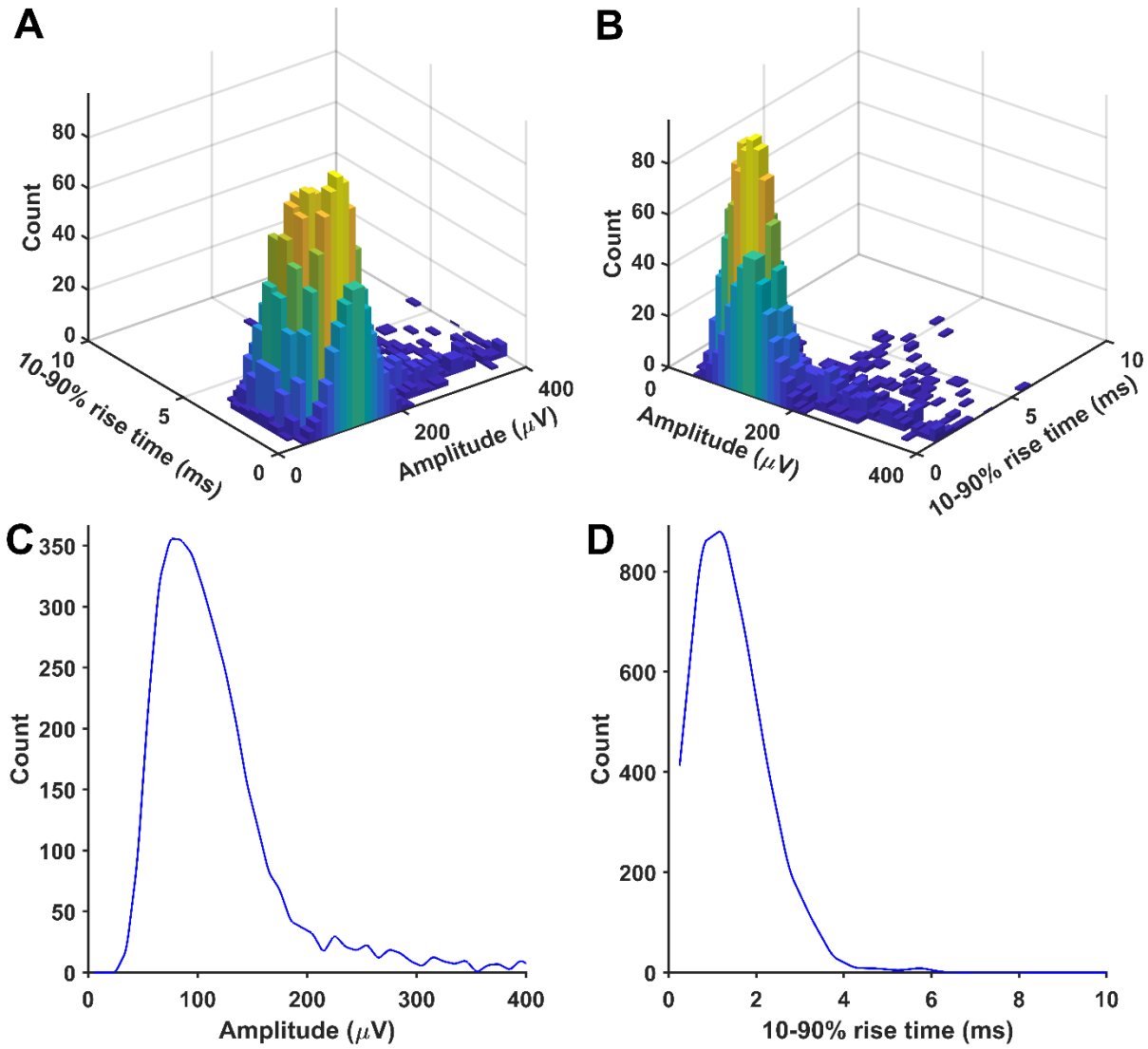

1308

1309 **Supplementary Figure 34:** An example of a distribution of randomly selected simulated minis that

1310 was used to produce a close match between distributions of mini-like events detected in a 'noise

1311 with simulated minis' voltage trace (30 µV lower limit on simulated amplitudes) and a 'noise with

1312 real minis' recording for cell p122a (layer 2/3).

1313 Panels as for Supplementary Figure 28.

1314

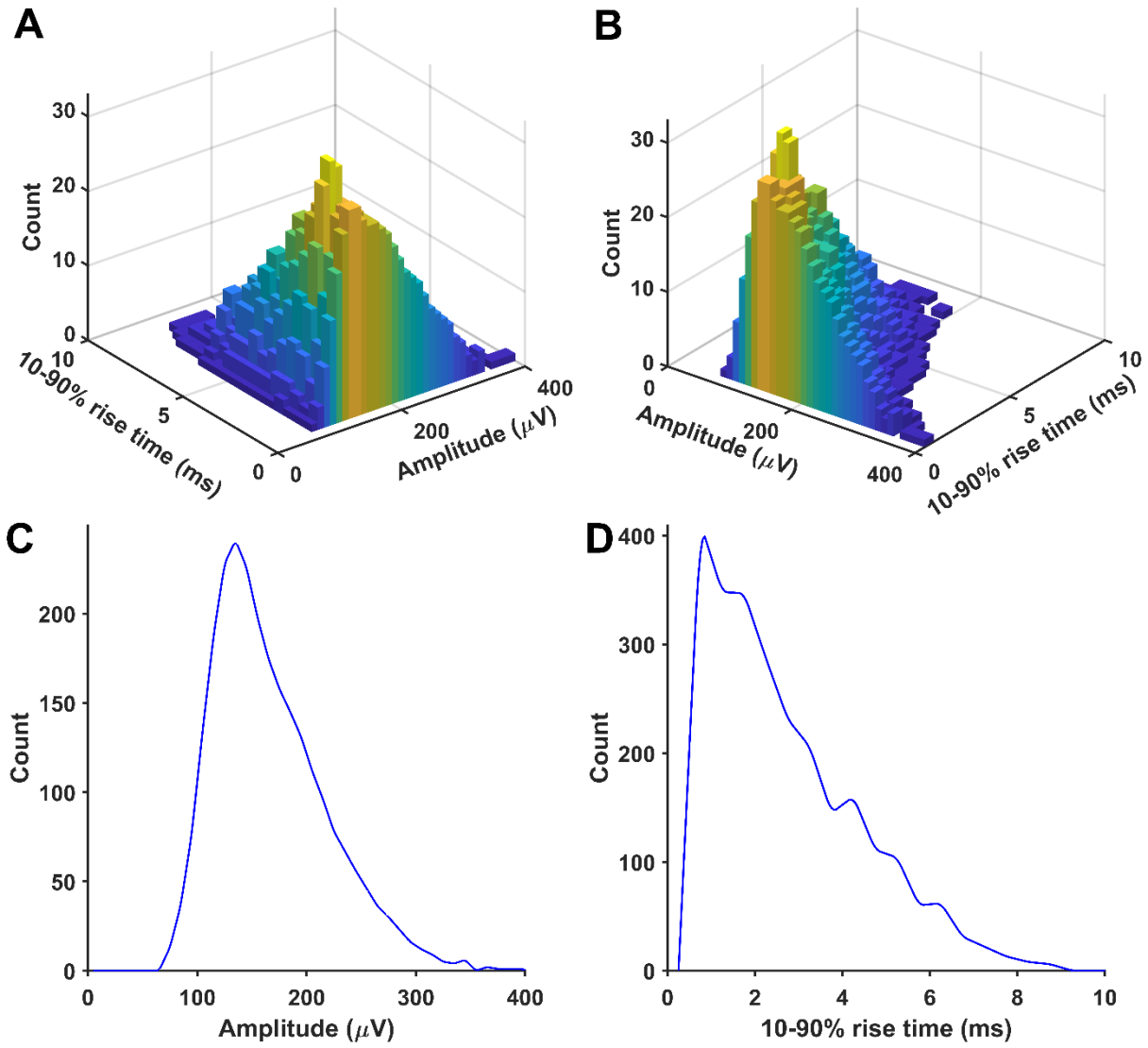

Supplementary Figure 35: An example of a distribution of randomly selected simulated minis that was used to produce a close match between distributions of mini-like events detected in a 'noise with simulated minis' voltage trace (40 µV lower limit on simulated amplitudes) and a 'noise with real minis' recording for cell p124b (layer 5).

Panels as for Supplementary Figure 28.

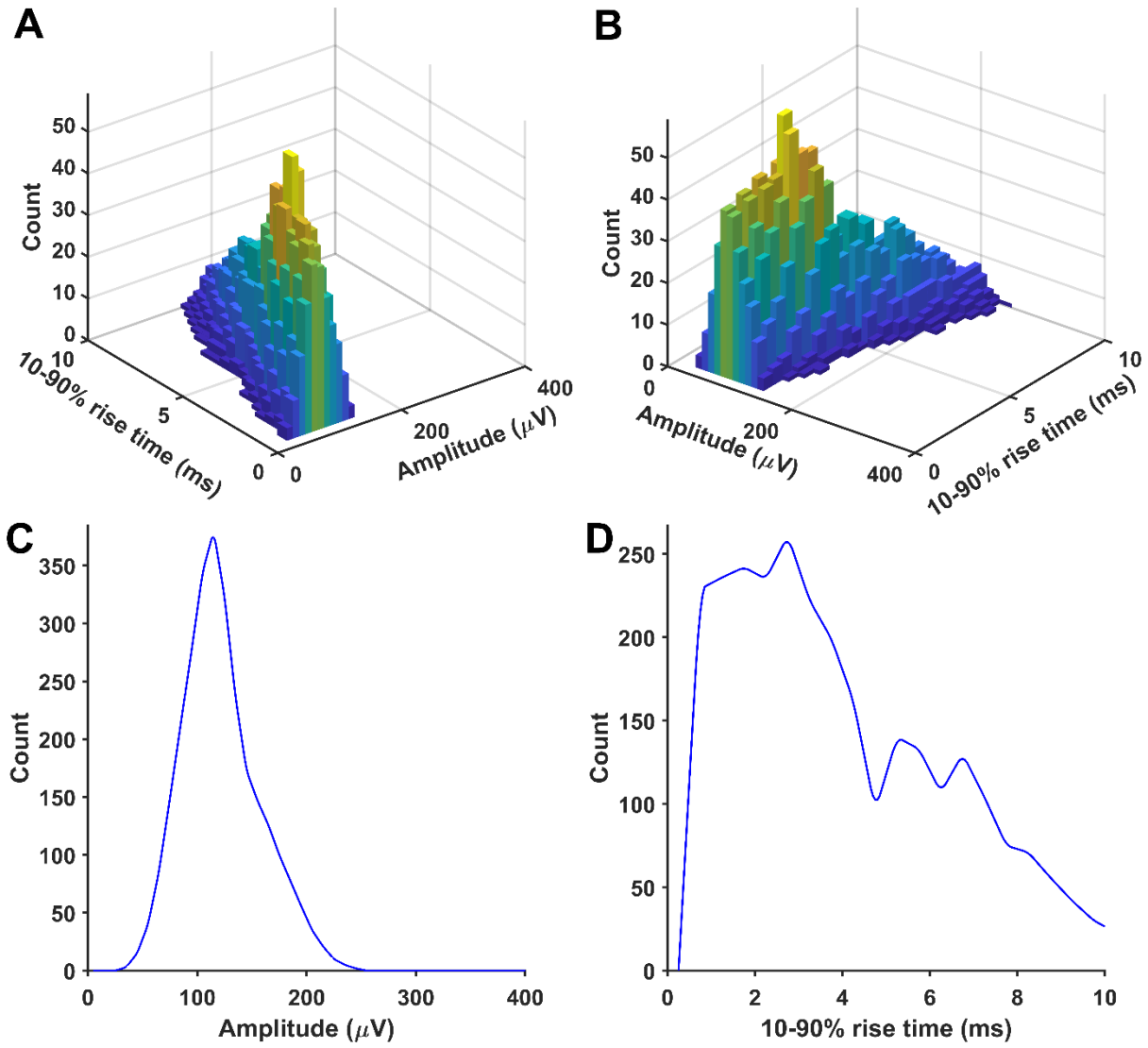

Supplementary Figure 36: An example of a distribution of randomly selected simulated minis that was used to produce a close match between distributions of mini-like events detected in a 'noise with simulated minis' voltage trace (30 µV lower limit on simulated amplitudes) and a 'noise with real minis' recording for cell p125a (layer 2/3).

Panels as for Supplementary Figure 28.

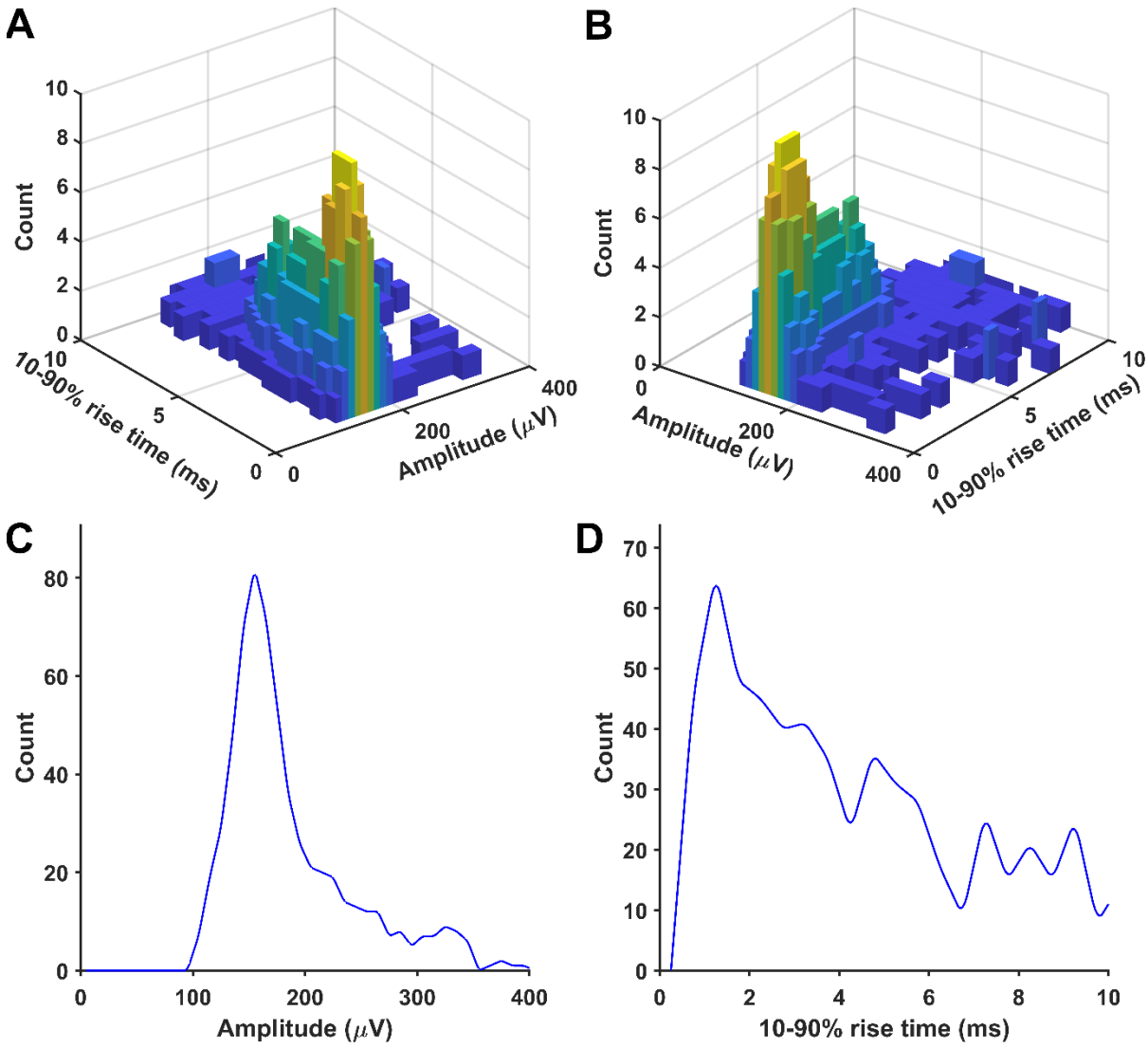

Supplementary Figure 37: An example of a distribution of randomly selected simulated minis that was used to produce a close match between distributions of mini-like events detected in a 'noise with simulated minis' voltage trace (100 µV lower limit on simulated amplitudes) and a 'noise with real minis' recording for cell p127c (layer 2/3).

Panels as for Supplementary Figure 28.

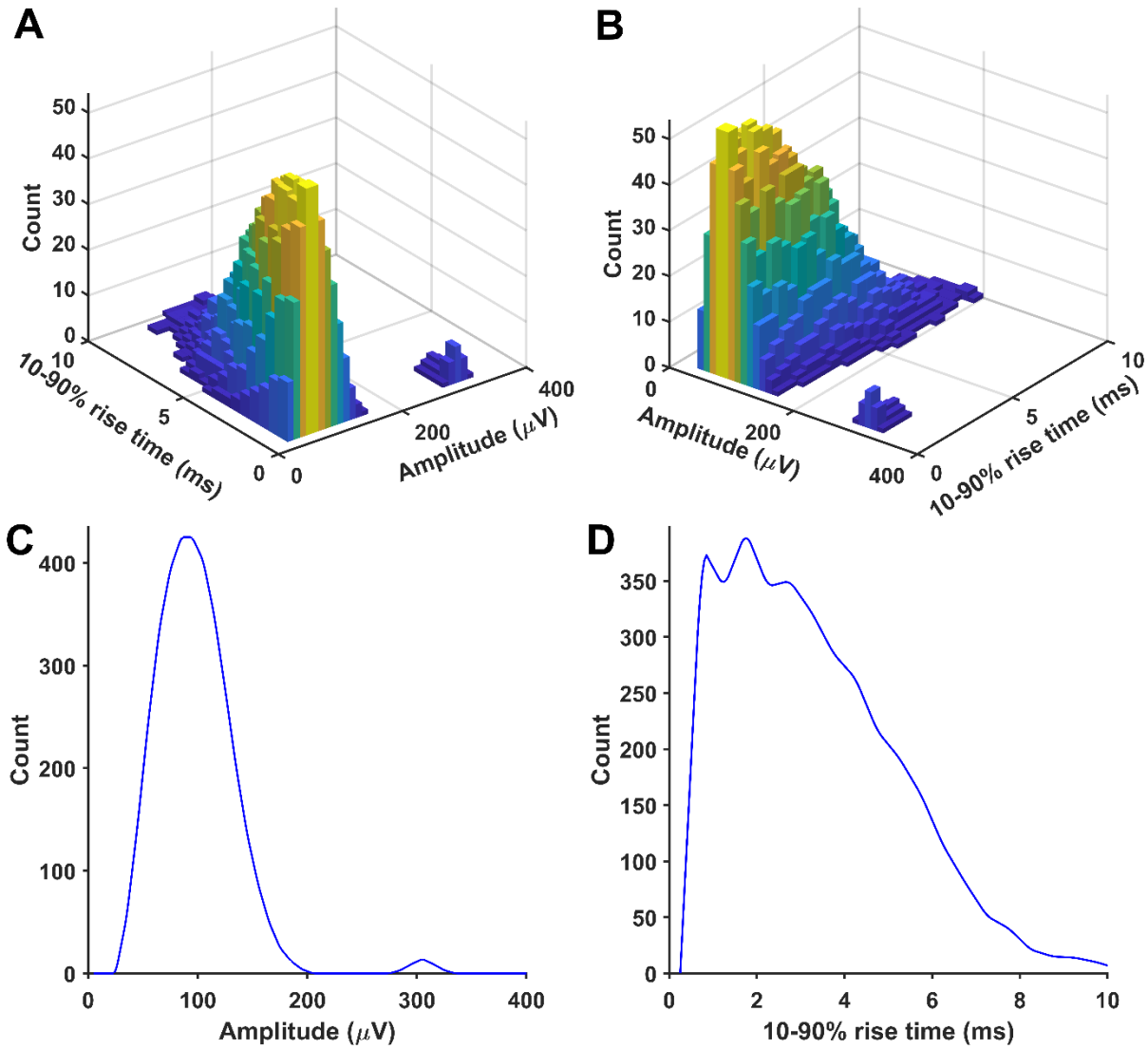

Supplementary Figure 38: An example of a distribution of randomly selected simulated minis that was used to produce a close match between distributions of mini-like events detected in a 'noise with simulated minis' voltage trace (30 µV lower limit on simulated amplitudes) and a 'noise with real minis' recording for cell p128c (layer 2/3).

Panels as for Supplementary Figure 28.

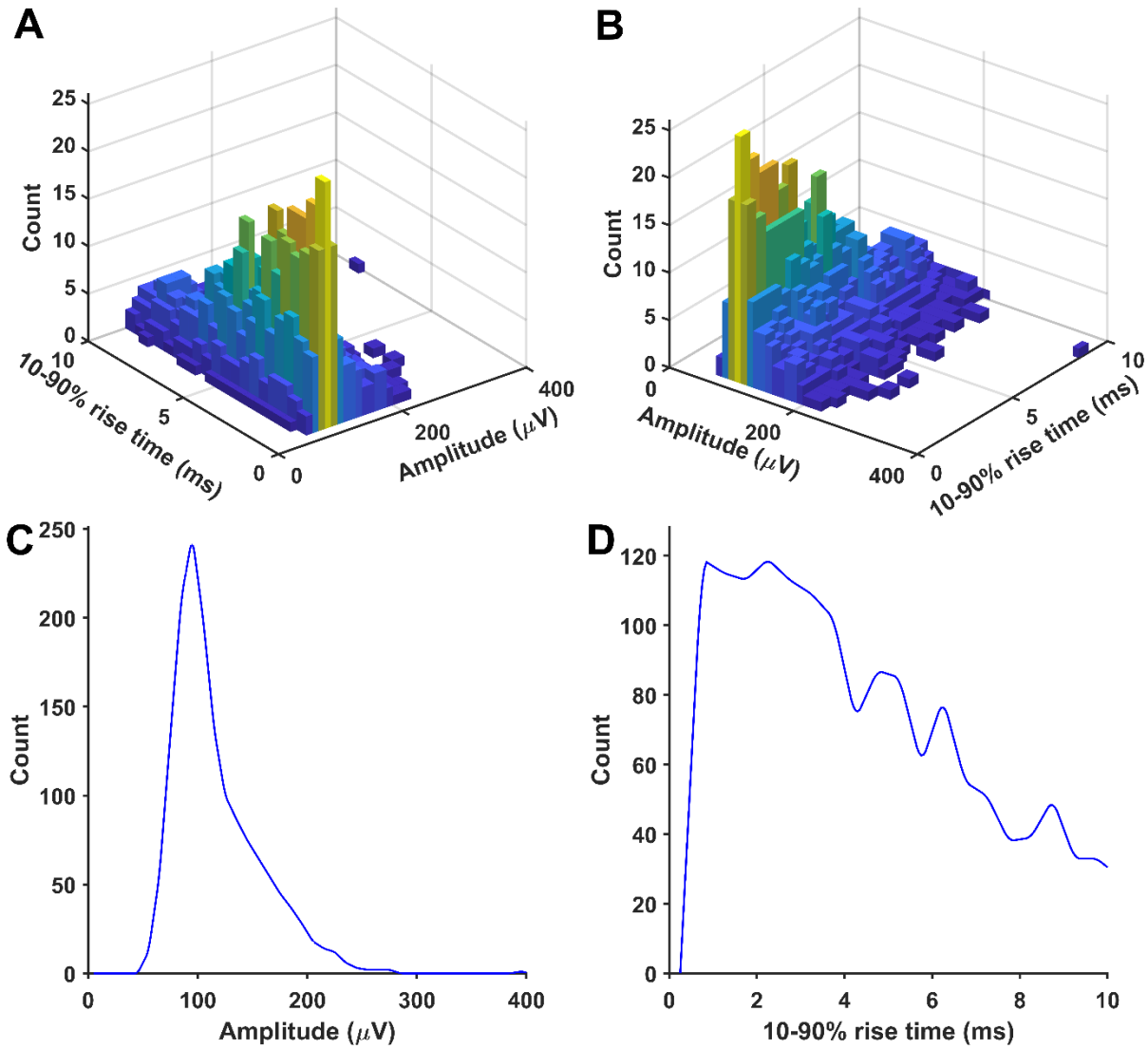

Supplementary Figure 39: An example of a distribution of randomly selected simulated minis that was used to produce a close match between distributions of mini-like events detected in a 'noise with simulated minis' voltage trace (50 µV lower limit on simulated amplitudes) and a 'noise with real minis' recording for cell p129a (layer 5).

Panels as for Supplementary Figure 28.

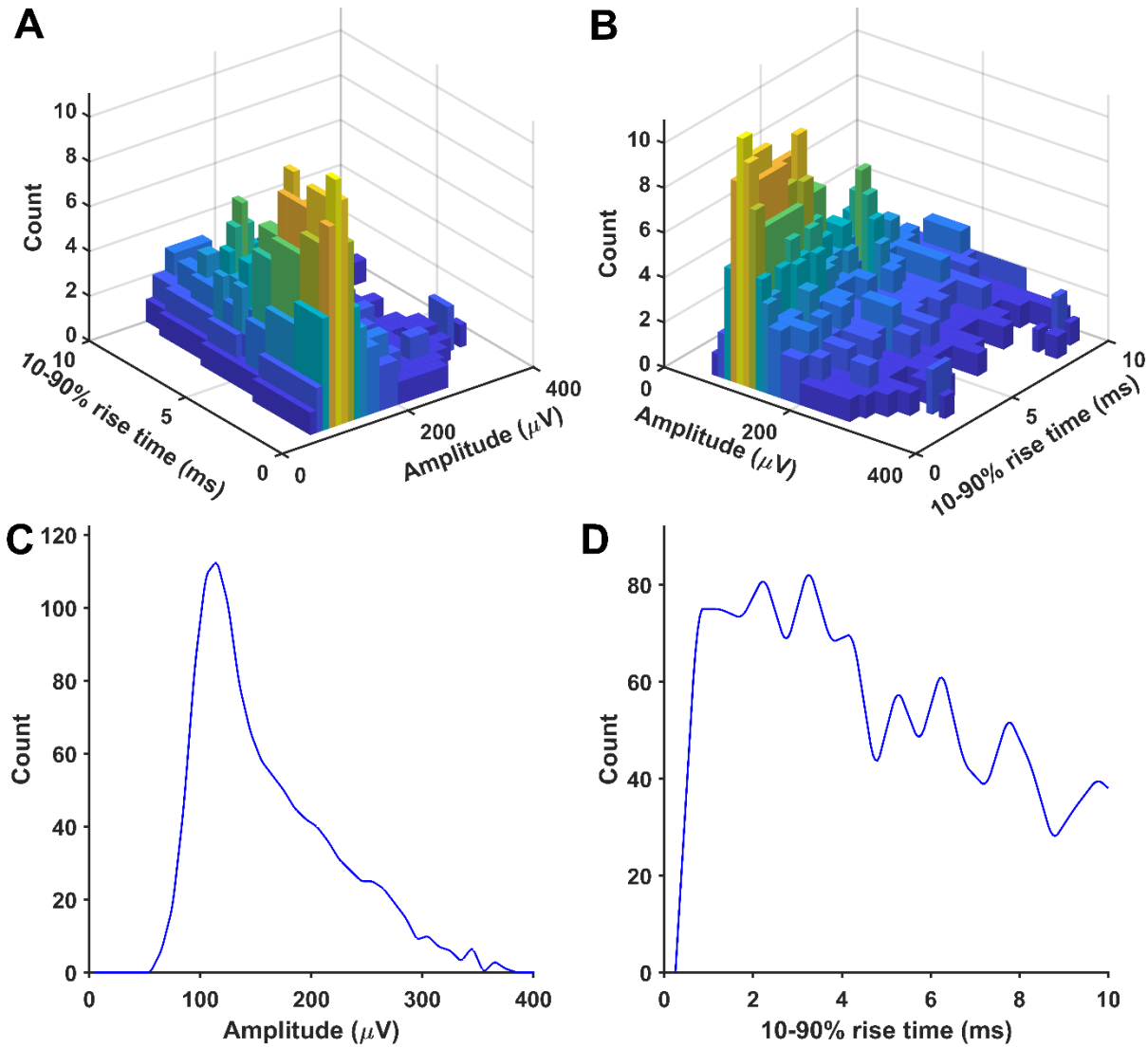

Supplementary Figure 40: An example of a distribution of randomly selected simulated minis that was used to produce a close match between distributions of mini-like events detected in a 'noise with simulated minis' voltage trace (60 µV lower limit on simulated amplitudes) and a 'noise with real minis' recording for cell p131a (layer 2/3).

Panels as for Supplementary Figure 28.